The Influence of Metabolic State on Targeted Drug Delivery, Biodistribution and Efficacy of Nanoparticles

A Dissertation Presented for the
Doctor of Philosophy
Degree
The University of Tennessee, Knoxville

Uchechukwu Chamberlin Anozie
May 2019

Copyright © 2019 by Uchechukwu Chamberlin Anozie.
All rights reserved.

ACKNOWLEDGEMENTS

I would like to thank my advisor Dr. Paul Dalhaimer for his support and guidance throughout the course of my dissertation. He has been very kind and gracious to me. I would also like to express my appreciation to all of my committee members. To Dr. Paul Frymier for his motivation and counsel. To Dr. Eric Boder for helping me have a better understanding of ligand-binding kinetics and also for lending me his Receptors book, which was very influential in the writing of this dissertation. I would like to thank Dr. Mike Fry for his willingness to serve on my committee, for helping with hematology and also for introducing me to Dr. Kim Newkirk who was also instrumental in the obesity and B-cell lymphoma project.

I extend my gratitude to Dr. Steve Abel for helping me think through some of the potential models that could be encountered for nanoparticle-protein binding. I would also like to thank his past student, Dr. Aaron Prescott for his help in working through some nanoparticle-protein models. I thank past students, Dr. Kevin Quigley, Dr. Alex Meyers and Katherine Krouse for their support during the initial phase of my graduate school project. I like to thank current students Molly Landon, Sid Mahajan, Jennifer Buczek, Monireh Asoudeh and Mitch Raith for their support. I particularly like to thank Jennifer for her help with RT-PCR, and Sid for this help with in-vitro cell-nanoparticle experiments.

I am grateful to Sarah Kauffman for her help in administering injections, working with me in running PCR reactions and also in handling all of our mice. I appreciate the help from Dr. Edward Wright with using the isothermal titration calorimetry and circular dichroism equipment, the help of Haden Scott for using the dynamic light scattering equipment, Eric Tague for identifying ApoA-I via mass spec., and the help of Liang Fang from Dr.

Boder's lab in using the gel filtration column. I would like to say a big thank you to all of our financial supporters because we would not be able to do this without them.

I would like to thank my parents Chief A. E. Anozie and Barrister Mrs. Anozie. They have been such a blessing to me; and sorry dad I cannot do two PhDs. I would like to thank my siblings for their support and most of all, for their friendship. I love all seven of you! Last but not least, I would like to thank my Lord and Savior, Jesus Christ, who has been with me through it all!

ABSTRACT

Plasma proteins have been shown to bind intravenously injected nanoparticles with high affinity and this could have potential consequences for drug delivery applications. A subset of plasma proteins, high density lipoproteins (HDLs), has been found to form a major component of the biomolecular corona of injected nanoparticles and this could possibly lead to nanoparticle therapies being diverted to HDL receptors (SCARBI).

I use polystyrene nanoparticles of different surface chemistries (PS, PS-COOH and PS-NH_2) and determine the affinity of lipoproteins for these nanoparticles. My findings indicate that the strength of binding of lipoproteins to nanoparticles *in vitro* is high enough to effect nanoparticle biodistribution *in vivo*. My *in vitro* binding studies also reveal that even with competition from other plasma proteins, lipoproteins still bind nanoparticles with moderate strength.

The ability of lipoproteins to redirect nanoparticles to their receptors upon binding was investigated by using mice models lacking SCARBI. Clodronate liposomes are utilized to eliminate the effects of macrophages so that I could eliminate background biodistribution. My study demonstrates that HDLs significantly affect nanoparticle biodistribution by comparing nanoparticle uptake and plasma lipoprotein cholesterol content in both wild-type and SCARBI-/-. Interestingly, nanoparticle uptake is increased in male SCARBI-/- mice following macrophage depletion, but the opposite is observed for females. Examination of plasma lipoprotein cholesterol content suggests that differences in lipoprotein and lipid metabolism between the genders could account for such dissimilarities.

To further elucidate the effects of metabolic state on nanoparticle uptake, I intravenously injected C57BL/6, KK-A^y and ob/ob mice with nanoparticles called, filomicelles. These mice are given two types of diets: a low-fat diet

(4 grams/day) and a high-fat diet *ad libitum*. KK-A^y and ob/ob are known to become obese upon consuming diets high in fat. Following obesity status, I observed that localization of filomicelles was reduced in the liver and spleen. In another study combining obesity and B-cell lymphoma in a mouse model, I address the potential for obese individuals to have a higher risk for advancing B-cell lymphoma. My results from hematology, and histopathological examinations of spleen and lymph node tissues indicates that obesity may have the potential to advance the disease.

TABLE OF CONTENTS

CHAPTER I Introduction 1
1.1 Background and Significance 2
1.2 Factors Impacting Nanoparticle Drug Delivery Efficacy 3
1.2.1 Biomolecular Corona 4
1.2.2 Nanoparticle Properties: Effect of Size and Shape 8
1.2.2.1 Effect of Particle Size and Shape on Margination 8
1.2.2.2 Effect of Particle Size and Shape on Cellular Uptake 13
1.2.2.3 Effect of Particle Size and Shape on Biodistribution 18
1.3 Conclusions 22
References 24
CHAPTER II The Impact of Lipoprotein Receptors and Lipid Metabolism on Nanomedicine 30
2.1 Abstract 31
2.2 Introduction 32
2.3 Materials and Methods 33
2.3.1 Materials 33
2.3.2 In Vitro Binding of Plasma Proteins to Polystyrene Nanoparticles 34
2.3.3 HDL Isolation by Anion Exchange Chromatography 35
2.3.4 Protein Identification by Mass Spectrometry 36
2.3.5 Gel Filtration Chromatography 37
2.3.6 Isothermal Titration Calorimetry (ITC) 38
2.3.7 Preparation of DiR-loaded PS-COOH Nanoparticles 38
2.3.8 In Vivo Studies 39
2.3.9 PCR Screening for Mice Genotype 39
2.3.10 HDL and LDL/VLDL Cholesterol Quantification 40
2.4 Results and Discussion 40
2.4.1 Measurement of Binding Parameters by Gel Electrophoresis 40
2.4.2 mHDL Purification by Anion Exchange Chromatography 46
2.4.3 Measurement of HDL Binding Parameters by ITC 49

2.4.4 Effect of Lipoprotein Binding and SCARBI Receptors on Nanoparticle Biodistribution 52
2.5 Conclusion 60
References 62
Appendix A 66
A.1 Isothermal Titration Calorimetry: Single Set of Independent Sites Binding Model 67
A.2 Protein Gel Calibration 69
A.3 Representative Protein Gels for the Binding of Nanoparticles to Plasma Proteins 70
A.4 Size Distribution of PSCOOH Nanoparticles 72
A.5 CD Profile of the Structural Changes of mHDL in $PSNH_2$ Nanoparticles 73
A.6 UV-VIS Absorbance Profile Showing Protein Depletion and Protein Gel Displaying the Plateau of ApoA-I 74
A.7 Protein Gels from mHDL Isolation by Anion Exchange Chromatography 75
A.8 Gel Filtration Chromatography Calibration Curve 75
A.9 PCR Genotyping with Genomic DNA from Mice Tails 76
A.10 Body Weight and Organ Weight of Mice 76
CHAPTER III The Localization of Soft Nanoparticles to the Liver and Spleen is Significantly Reduced in Obese Mice 78
3.1 Abstract 79
3.2 Introduction 79
3.3 Materials and Methods 80
3.3.1 Synthesis of Diblock Copolymers for Filomicelles 80
3.3.2 Nanoparticle Preparation 82
3.3.3 Mice 82
3.3.4 Imaging 83
3.4 Results and Discussion 83
3.5 Conclusion 85
References 89
CHAPTER IV Incorporation of Obesity and B-cell Lymphoma in a Mouse Model 91
4.1 Abstract 92
4.2 Introduction 92

4.3 Materials and Methods 95
4.3.1 Breeding and Injections 95
4.3.2 PCR Screening for Mice Genotype – Lep^{Ob} 95
4.3.3 PCR Screening for Mice Genotype – Eμ-*myc* 96
4.3.4 Blood Collection 97
4.3.5 Hematology 97
4.3.6 Tissue Fixation and Evaluation 97
4.4 Results and Discussion 97
4.5 Conclusion 100
References 111
Appendix C 114
C.1 PCR Genotyping for Lep^{ob} Status and Eμ-*myc* 115
CHAPTER V Conclusion and Recommendations 116
5.1 Conclusion 117
5.2 Recommendations for Future Studies 117
VITA 119

LIST OF TABLES

Table 1.1 High absorbance proteins (>10% in biomolecular corona) associated with HDLs and LDLs[34-36] 7
Table 1.2 Summary of size-dependent cellular uptake 15
Table 2.1 Adsorption Parameters Obtained from ITC and Protein Gel Electrophoresis 51
Table 4.1 Experimental Outline of Injection Schedule, Blood Collection and Diet Placement 101
Table 4.2 Weight of Mice During Experiments* 103
Table 4.3 White Blood Cell Count from Blood of Eμ-*myc* Transgenic and Normal Mice 104
Table 4.4 Histological Classification for Spleen and Lymph Node Tissues of Normal and Eμ-*myc* Mice 106
Table 4.5 Weights of Spleen and Lymph Node in C35-C38 110

LIST OF FIGURES

Figure 1.1 Venn diagram showing the distribution of biomolecular corona as related to the lipoproteome[34-36] 7

Figure 1.2 Nanoparticle margination to red blood cell-free layer 9

Figure 1.3 Time to margination as a function of particle radius for $\Delta\rho = 10^3$ and 10^4 relative density values. Adapted from ref.[49] 11

Figure 1.4 (A) The relationship between internalization velocity and Ω for different nanoparticle shapes. (B) Phagocytosis phase diagram for the different nanoparticle shapes. Adapted from ref.[70] 17

Figure 2.1 Saturation Binding Curve of ApoA-I to PS Nanoparticles 43

Figure 2.2 Saturation Binding Curve of ApoA-I to PS-COOH Nanoparticles 44

Figure 2.3 Saturation Binding Curve of ApoA-I to PS-NH_2 Nanoparticles 44

Figure 2.4 Fraction Bound of ApoAI from (A) Mouse Plasma and (B) hHDL on Polystyrene Nanoparticles 45

Figure 2.5 Elution of mHDLs and other Plasma Proteins at the Initial Salt Gradient Scheme. Left Panel: a-n, fraction 75 – 88; Right Panel: a-f, fraction 96 – 101; g-l, fraction 89-95. 47

Figure 2.6 Chromatograms of the Purification of Lipoproteins from Mouse Plasma. Left Panel: Initial Salt Gradient Scheme. Right Panel: Final Salt Gradient Scheme. Linear gradient additions of elution buffer initiates after initial unbound plasma proteins are released from the column 47

Figure 2.7 Elution of mHDLs and other Plasma Proteins from the Final Salt Gradient Scheme. Left Panel: a-n, fraction 76 – 89. Right Panel: a-n, 90 – 103 48

Figure 2.8 Peaked Pooled Fraction of mHDLs from Anion Exchange Chromatography. Left Panel: mHDL Profiles in a 10-well Gel from Using the Initial Salt Gradient Scheme; a- fraction 87 - 88 and 91 – 94; b- 87 - 90. Right Panel: mHDL Profiles in a 15-well Gel from Using the Final Salt Gradient Scheme; a, 88 – 89; b, 90 – 93; c, 94 – 103; d, 90 – 103. 48

Figure 2.9 ITC Data from Titrating hHDL into Polystyrene Nanoparticles. (A) hHDL + PS. (B) hHDL + PS-COOH. (C) hHDL + PS-NH_2. The top panels represent the raw data from titrations after referenced baseline correction. The bottom panel are the integrated heats from each peak fitted to an independent binding model (solid lines). 50

Figure 2.10 ITC Data from Titrating mHDL into Polystyrene Nanoparticles. (A) mHDL + PS. (B) mHDL + PS-COOH. (C) mHDL + PS-NH_2. The top panels represent the raw data from titrations after referenced baseline correction. The bottom panel are the integrated heats from each peak fitted to an independent binding model (solid lines). 50

Figure 2.11 Fluorescence Intensity of Organs of Male SCARBI Ex Vivo After Macrophage Depletion with Clodronate Liposomes. PSCOOH+dye values are means ± SD (n = 5) except SCARB -/- (n = 3), dye (n = 1), pbs (n = 1). + $p < 0.05$, ++ $p < 0.01$ as determined by t-test (an F-test for equal and unequal variances was done and the corresponding t-test was applied). 54

Figure 2.12 Fluorescence Intensity of Organs of Male SCARBI Ex Vivo After Injections with Control Liposomes. PSCOOH+dye values are means ± SD (n = 5), dye (n = 1), pbs (n = 1) except SCARB -/- (n =2). ++ p < 0.01 as determined by t-test (an F-test for equal and unequal variances was done and the corresponding t-test was applied). 54

Figure 2.13 Fluorescence Intensity of Organs of Female SCARBI Ex Vivo After Macrophage Depletion with Clodronate Liposomes. PSCOOH+dye values are means ± SD (n = 5), dye (n = 1), pbs (n = 1). ++ p < 0.01, +++ p < 0.001 as determined by t-test (an F-test for equal and unequal variances was done and the corresponding t-test was applied) 55

Figure 2.14 Fluorescence Intensity of Organs of Female SCARBI Ex Vivo After Injections with Control Liposomes. PSCOOH+dye values are means ± SD (n = 5), dye (n = 1), pbs (n = 1). + p < 0.05 as determined by t-test (an F-test for equal and unequal variances was done and the corresponding t-test was applied). 55

Figure 2.15 SCARBI Female Organ Weights. n = 5. + p < 0.05 as determined by t-test (an F-test for equal and unequal variances was done and the corresponding t-test was applied) 56

Figure 2.16 SCARBI Male Organ Weights. n = 5, but wclod SCARBI-/- n = 3. + p < 0.05, +++ p < 0.001 as determined by t-test (F-test for equal and unequal variances was done and the corresponding t-test was applied). 56

Figure 2.17 Plasma HDL and LDL/VLDL Concentration in Male and Female Mice Treated With Clodronate and Control Liposomes. For SCARBI+/+, n = 3 for all except females treated with clodronate liposomes n = 4. For SCARBI-/-, n = 3, 4, 4 and 5 for males treated with clodronate liposomes, control liposomes; and females with clodronate liposomes, control liposomes respectively. + p < 0.05 and ++ p < 0.01 as determined by t-test (an F-test for equal and unequal variances was done and the corresponding t-test was applied). 59

Figure A.2-1 Protein Gel Calibration of 1/20X Plasma with BSA in 10-well Gels. (A) Lane 2- 1/20X plasma, lane 3- 0.175 µg, lane 4- 0.25 µg, lane 5- 0.5 µg, lane 6- 1 µg, lane 7- 2 µg, lane 8- 4 µg, lane 9- 8 µg. (B) Lane 2- 1/20X plasma, lane 4- 0.15 µg, lane 6- 0.125 µg, lane 7- 0.1 µg, lane 8- 0.05 µg, lane 9- 0.075 µg 69

Figure A.2-2 Protein Gel Calibration of 1/20X Plasma with BSA in 15-well Gels. (A) and (B) Lane 1- 0.05 µg, lane 2- 1/20X plasma, lane 3- 0.125 µg, lane 4- 0.15 µg, lane 5- 0.175 µg, lane 6- 0.25 µg, lane 7- 0.5 µg, lane 9- 1 µg, lane 10- 0.1 µg, lane 11- 2 µg, lane 12- 0.075 µg, lane 13- 8 µg, lane 15- 4 µg. 70

Figure A.3-1 Protein Gels of PSCOOH Binding to 1/5X – 1/2X plasma. (A) 2- 1/20X standard, 4- 1/3X plasma, 6- 1/3X plasma + PSCOOH, 8- 1/2X plasma, 10- 1/2X + PSCOOH, 12- 1/5X plasma, 14- 1/5X plasma + PSCOOH. Lane 4 – 14, supernatant. (B) Same as (A) except lane 4 – 14 is pellet. 70

Figure A.3-2 Protein Gels of PSCOOH Binding to 100X – 1/20X plasma. (A) 2- 1/20X standard, 3- 1/50X, 4- 1/50X + PSCOOH, 6- 1/20X + PSCOOH, 7- 1/20X, 8- 1/100X, 9- 1/100X + PSCOOH. Lane 3 – 9, supernatant. (B) Same as (A) except lane 3 – 9 is pellet 71

Figure A.3-3 Protein Gels of PSCOOH Binding to 100X – 1/60X plasma. (A) 2- 1/20X standard, 3- 1/100X + PSCOOH, 4- 1/100X, 5- 1/70X, 6- 1/70X + PSCOOH, 8- 1/60X, 9- 1/60X + PSCOOH. Lane 3 – 9, supernatant. (B) 2- 1/20X standard, 3- 1/100X, 4- 1/100X + PSCOOH, 6- 1/70X + PSCOOH, 7- 1/70X, 8- 1/60X, 9- 1/60X + PSCOOH. Lane 3 – 9, pellet. 71

Figure A.4-1 Top Panel: PSCOOH. Bottom Panel: PSCOOH-DiR....72

Figure A.5-1 Secondary Structural Changes Of mHDL Incubated With $PSNH_2$ Nanoparticles....73

Figure A.6-1 Absorbance Spectra Showing Complete Nanoparticle Pelletization After Ultracentrifugation. Left Panel: Depicting absorbance spectra without ultracentrifugation. Right Panel: Depicting the supernatant absorbance spectra after ultracentrifugation of the $PSNH_2$ and 1/20X plasma suspensions....74

Figure A.6-2 Protein Gel Showing the ApoA-I Bands from the Supernatant After Ultracentrifugation....74

Figure A.7-1 Protein Gels Depicting the Elution of One or More Distinct Plasma Proteins Prior to Changing the Salt Gradient Scheme. Left Panel: a-b, fraction 44 – 46; d – m, fraction 51-60. Right Panel: a-m, fraction 61-74..75

Figure A.8-1 Calibration Curve for Estimating the Molecular Weights of mHDL and hHDL....75

Figure A.9-1 SCARBltm1kri Genotyping with PCR. Wild-type represent one 262 bp band, mutant represents one 140 bp band, while heterozygous represents both 140 bp and 262 bp bands....76

Figure A.10-1 Body weight of male and female SCARBI+/+ and SCARB-/- mice....76

Figure A.10-2 Organ weight differences between male and female mice injected with either clodronate liposomes or control liposomes. + $p < 0.05$, ++ $p < 0.01$ as determined by the t-test (an F-test for equal and unequal variances was done and the corresponding t-test was applied). n.s. p. denotes no significant difference between all the male-female pairs within a clodronate liposome or control liposome group....77

Figure 3.1. Biodistribution of filomicelles in mice as a function of diet, weight, and genetics. (A) Plot of the weights of mouse livers as a function of mouse weight at the time of injection of filomicelles carrying NIR dye (filomicelles-NIR). Open symbols represent mice that were fed a low fat diet (LFD). Closed symbols represent mice that were fed a high fat diet (HFD). Mice that are represented by the open symbols in the box were restricted to 4 g/d of LFD. (B) Fluorescent images of livers from the mice that were injected with filomicelles-NIR. (C) Fluorescent intensity of the livers shown in (B). Each data point represents three livers. (D) Plot of the weights of mouse spleens as a function of mouse weight at the time of injection of filomicelles-NIR. Scale bars are 10 mm....87

Figure 3.2 (A) Fluorescent images of spleens from the mice that were injected with filomicelles-NIR. (B) Fluorescent intensity of the spleens shown in (A). Each data point represents three spleens. (C) Plot of the weights of mouse WAT as a function of mouse weight at the time of injection of filomicelles-NIR. (D) Fluorescent images of the WAT from the mice that were injected with filomicelles-NIR. (E) Fluorescent intensity of the WAT shown in (D). Each data point represents the WAT from three separate mice. Scale bars are 10 mm. 88

Figure 4.1 White Blood Count Frequency Distribution....103

Figure 4.2 Blood smear showing morphology of granulocytes and lymphoblasts (60x)....105

Figure 4.3 Spleen Histology of ob/ob Female (C28) Mice on a High Fat Diet for 8 weeks and following 3 Consecutive Week Injections of 5mg/kg PTX. (A) and (B) show the expansion of periarteriolar lymphoid sheaths, 100x and 200x respectively. (C) Extramedullary hematopoiesis in the red pulp (400x). (D) Enlarged view of the periarteriolar lymphoid sheath (400x). Left of the star in (D) is the arteriole....107

Figure 4.4 Histology of Lymph Node of ob/ob Female Mice (C28) on a High Fat Diet for 8 weeks and following 3 Consecutive Week Injections of 5mg/kg PTX. (A), (B) and (C) show the central germinal centers with larger cells

surrounded by small lymphocytes. (D) Enlarged imaged from image [E] showing the cholesterol cleft and the formation of a multinucleated giant cell (400x). (E) Lymph node expanded by cholesterol granuloma (100x). (F) Displaying foamy macrophages (200x). Square box is for the enlarged image in [D].....108

Figure 4.5 Histology of Lymph Nodes of Male (C35) ob/OB x Eμ-*myc* Mouse on a High Fat Diet for 2 weeks. (A) Showing no lymph node architecture and cells extending beyond the capsule (200x). (B) Enlarged image showing lymph node capsule (400x). (C) Monomorphic populations of large round cells with frequent mitoses (orange circle), and apoptotic cells often in clusters (green circle) (400x).....109

Figure C.1 Representative PCR results from the tail biopsies displaying the Lepob and Eμ-*myc* status of bred mice. 324 bp, internal positive control. 210 bp, B-cell lymphoma status. 155 bp; 155 bp, 100 bp and 55 bp; and 55 bp correspond to wild-type, heterozygous, and mutant for obesity status.....115

CHAPTER I

Introduction

1.1 Background and Significance

The leading causes of death in the world are due to noncommunicable diseases such as metabolic diseases, cardiovascular diseases and cancer. Recent statistical estimates by the World Health Organization show that half of the deaths that occurred worldwide in 2016 were attributable to these mentioned noncommunicable diseases (NCD) with more than 60% of NCD being related to cardiovascular diseases.[1] In the United States, in particular, NCD accounted for more than 88% of the 2.8 million deaths that occurred in 2016 with cardiovascular diseases (34% of NCD) and cancer (25% of NCD) being the top-killers.[1-2]

The rapid rise in these diseases has been linked to the global obesity epidemic.[3-4] Current data suggests that more than one-third of the world's population in 2016 was either overweight (Body Mass Index $\geq$ 25 kg/m^2 to < 30 kg/m^2) or obese (Body Mass Index $\geq$ 30 kg/m^2);[5] and if secular trends are to continue, epidemiologist and researchers alike have projected that half of the world's adult population will be overweight or obese by 2030.[6-7] In the United States, these 2030 projections are pretty steep with over 86% of the adult population being either overweight or obese and 51% obese.[3, 8]

Given these dire statistics, there is an overwhelming likelihood that patients that would potentially be administered drugs in the clinic will either be overweight or obese. However, the vast majority of studies that are carried out to develop and test the effectiveness of these drugs or drug delivery vehicles (e.g. nanoparticles) use lean animal models. Therefore, the need for models that explore non-ideal metabolic states is of utmost importance. Several elements need to be examined when addressing the effects of non-ideal metabolic states like obesity on nanoparticle drug delivery. These may include varying circulating lipoprotein levels, enlarged/fatty livers, and associated conditions like, type 2 diabetes or atherosclerosis.

Circulating lipoproteins could limit nanoparticle effectiveness in reaching their desired targets. It has been shown in numerous studies that when nanoparticles are exposed to biological fluids (e.g. blood or plasma), proteins and other biomolecules bind to their surfaces and form a coating known as the protein or biomolecular corona.[9-12] A protein or biomolecular corona defines the biological identity of a nanoparticle; therefore, it can exert an influence over its clearance kinetics. Lipoproteins have been shown to be components of the biomolecular corona in many different nanoparticles with various surface modifications.[9-12] Of particular interest are high-density lipoproteins (HDLs) that have been found to bind strongly to nanoparticles.[10-11]

HDLs could conceivably redirect nanoparticles to HDL receptors (e.g. scavenger receptor class B type I) on liver sinusoidal endothelial cells (LSEC) or hepatocytes of the liver,[13] endothelial cells of the lung, heart etc.,[14] and thereby diminish the delivery of the therapeutic payload to targets other than tissues or cells that express scavenger or lipoprotein receptors. Therefore, pertinent mouse models that test the ability of HDLs to retain their functionality after binding nanoparticles would prove useful and insightful given the interaction and function of HDLs and its receptors in the body.

Ultimately, mouse models that combine the effects of metabolic imbalances and cancer would also be of great significance since the overall goal is to ultimately evaluate the effects of a patient's metabolic condition on targeted nanoparticle efficacy.

1.2 Factors Impacting Nanoparticle Drug Delivery Efficacy

Several factors impact the delivery of nanoparticle therapeutics and these may include physicochemical properties such as size, shape, surface chemistry, site-specific targeting ligands, etc.[15-16] Other factors like the aforementioned biomolecular corona and patient metabolic state are also crucial components to nanomedicine and

drug delivery efficacy. Due to the intricate nature of biological systems and their effect on drug delivery, it is worthwhile to address these factors as they would provide for a more streamlined approach in the application of targeted drug delivery systems.

1.2.1 Biomolecular Corona

Nanoparticles injected into the bloodstream are exposed to thousands of blood proteins and other biomolecules (e.g. nucleic acids, sugars) which compete for the nanoparticle surface.[12, 17-18] The process of biomolecular corona formation occurs whereby the kinetics of binding initial favor the most abundant proteins in the bloodstream but over a relatively short period of time (seconds to minutes) these are replaced by proteins of higher affinity.[18-19] As the nanoparticle travels from one biological environment to another, it embodies this biomolecular corona "fingerprint" which can determine further associations and interchanges in its new environment.[18, 20] Clearly, this biomolecular "fingerprint" is important in drug delivery efficacy because it can dictate the recognition of nanoparticle-biomolecular corona complexes by the immune system or cell-surface receptors. Recognition of these nanoparticles is facilitated by proteins that may or may not undergo conformational changes and have exposed epitopes in the biomolecular corona.[21]

It is important to note, however, that proteins in the biomolecular corona can function as opsonins and dysopsonins.[22] Dysopsonin adsorption reduces the recognition of nanoparticles by the immune system, thus, extending its circulation time in the body.[22] As an example, apolipoproteins and albumin have been shown to bind nanoparticles and decrease the adsorption of opsonins such as immunoglobulin G and complement factors, hence inhibiting complement activation.[23-24] Although complement activation can lead to the rapid clearance of nanoparticles in the body, it is not the only mechanism by which to predict nanoparticle clearance. A recent study

reported by Bertrand and coworkers[25] have showed that poly(ethylene glycol)-*b*-poly(lactic co glycolic acid) (PEG-PLGA) nanoparticles with low steric hindrance and absorbed apolipoprotein E (ApoE) protect the nanoparticles against rapid opsonization and increases blood circulation time in experiments that implemented C57BL/6 and ApoE-/- mice models. More importantly, they observed similar levels of complement protein C3 and other complement components on PEG-PLGA nanoparticles that displayed rapid and slow clearances in experiments that implemented C57BL/6 and complement protein C3-/- mice models. Ultimately, they demonstrated that low-density lipoprotein receptors could also be essential to the rapid clearance of nanoparticles because of the presence of ApoE in the biomolecular corona.

Evidently, the composition of the biomolecular corona is important to nanoparticle drug delivery but the question that requires more probing is which proteins or biomolecules in the biomolecular corona are "most relevant" to evaluating therapeutic effectiveness. The simple answer is, it depends. There are several complex elements that need to be taken into consideration. For example, the fact that every human has a unique blood profile that also changes with disease type coupled with different routes for nanoparticle drug administration can affect which proteins or biomolecules are considered "most relevant".[21, 26-27] In addition, the composition of the biomolecular corona is unique to each nanomaterial type, and dissimilar physicochemical properties also influence the biomolecular corona composition thus adding another facet of complexity to finding a one-size-fits-all solution to nanoparticle drug delivery.[15] Therefore, one possible approach would be to have a repository where you can resolve the biomolecular corona of each nanoparticle type tailored to specific disease conditions. Various models could also be built to predict nanoparticle biological outcome after identities of potential candidates from the biomolecular corona are established. This proposal is plausible because we can model binding affinity constants for nanoparticle-protein interactions and there have already been quantitative and computational efforts to advance

our understanding of the biomolecular corona as it relates to predicting nanoparticle-cell association,[28-31] biodistribution,[32-33] and toxicity[28-29, 32].

Although computational developments are far from being fully realized, we can nonetheless peruse research studies in literature to look at major proteins of the biomolecular corona that form on different nanomaterials. Walkey and Chan did an extensive review on plasma proteins that bound to 63 nanomaterials by compiling data from 26 independent research studies.[34] In their review, they discovered a subset of 125 unique plasma proteins that bound to at least one of the 63 nanomaterials. Of these 125 plasma proteins, 21 were found to constitute greater than 10% of the total absorbed biomolecular corona mass and were termed "high abundance" proteins. 15 of the 21 high abundance proteins were found to be associated with lipoproteins, particularly HDLs (Table 1.1). These associations were made by cross-matching to a compendium of HDL associated proteins by Davidson and coworkers (Figure 1.1).[35-36] It should also be noted that approximately two-thirds of the 125 plasma proteins were listed in the compendium of either the HDL or LDL proteome watch list. In general, the 125 plasma proteins discovered on the 63 nanomaterials are involved in physiological roles related to lipid metabolism and transport, complement activation, immune response, inflammation, hemostasis, and metal binding or ion transport.[35, 37]

With knowledge of plasma proteins or biomolecules that form the core of the biomolecular corona, scientists can then exploit such information to predict physiological responses and enhance therapeutic potential. Obviously, care should be taken as with any model to determine its scope and applicability since not all systems are translatable. A simple example is that not all *in vitro* systems translate *in vivo*; but studies that combine *in vitro*, *in situ*, and *in vivo* models would be essential in optimizing translatability.

Table 1.1 High absorbance proteins (>10% in biomolecular corona) associated with HDLs and LDLs[34-36]

Protein	HDL*	LDL*
Apolipoprotein A-I	1	1
Apolipoprotein A-IV	1	1
Apolipoprotein B-100	0	1
Apolipoprotein C-II	1	1
Apolipoprotein C-III	1	1
Apolipoprotein E	1	1
Clusterin	1	1
Complement C3	1	0
Fibrinogen	1	1
Haptoglobin	1	0
Hemoglobin	1	0
Histidine-rich glycoprotein	1	0
Ig gamma chain	1	0
Inter alpha trypsin inhibitor H1	1	0
Paraoxonase-1	1	0
Serum albumin	1	1

* 1 – Protein is present, 0 – Protein is absent.

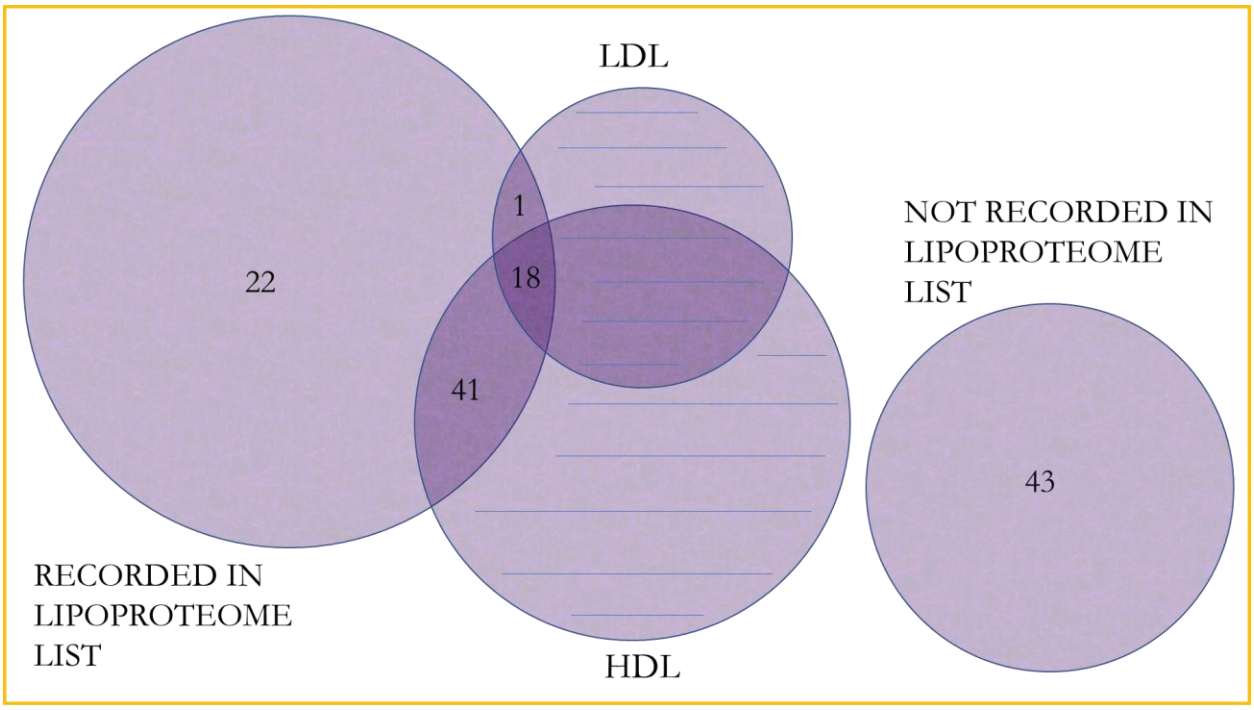


Figure 1.1 Venn diagram showing the distribution of biomolecular corona as related to the lipoproteome[34-36]

1.2.2 Nanoparticle Properties: Effect of Size and Shape

The size and shape of nanoparticles play important roles in margination dynamics, opsonization, cellular uptake and biodistribution. Overcoming barriers to nanoparticle drug delivery can be made possible by designing nanoparticles of different sizes and shapes to accumulate in desired tissues or cells of interest. Recognizing the roles and limitations of these factors (size and shape) in assessing nanoparticle design parameters is important to the field of drug delivery.

1.2.2.1 Effect of Particle Size and Shape on Margination

The tendency for nanoparticles to laterally drift towards endothelial walls is beneficial for nanoparticle-cell associations and in theory could improve the likelihood of site-specific active targeting (e.g. cancerous tumors). Conventionally speaking, this phenomenon is usually assigned to free-flowing leukocytes and platelets that exit the central blood flow and localize to a region near vessel walls known as the red blood cell-free layer; therefore, it is only befitting that nanoparticles be fine-tuned with similar geometries of these blood components to achieve the intended benefits of marginating to this red blood cell-free layer (Figure 1.2). Researchers have studied this margination propensity by implementing mathematical models, and their findings demonstrated that particles possessing a typical spherical geometry are less likely to marginate to vessel walls than nonspherical particles.[38-41] In addition to mathematical models, studies that assessed margination dynamics in more physiological conditions have also shown that particle size and shape are important to marginating to vessel walls.[42-46]

Lee and coworkers investigated the importance of particle size on margination dynamics by employing intravital microscopy to monitor the flow of 200 nm and 1000 nm PEGylated fluorescent polystyrene spheres in the microcirculation of Balb/c mice ear.[42] Results of the study revealed that the 1000 nm particles were more

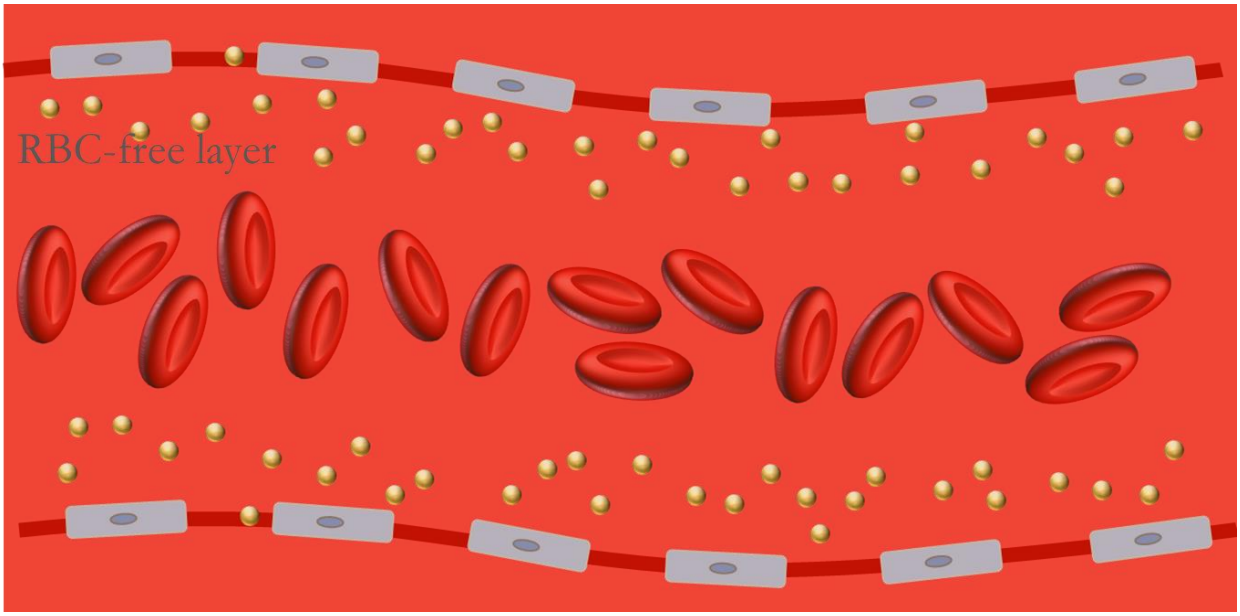


Figure 1.2 Nanoparticle margination to red blood cell-free layer

effectively pushed laterally to the vessel walls by red blood cells. Simulations of transport within whole blood were run by the group and also showed this size-dependent behavior with larger particles (500 nm and 1000 nm) having better margination dynamics than smaller ones (10 nm, 50 nm and 100 nm). These results would imply that sub-micron to micron-sized spherical particles are more effectively pushed laterally to vessel walls and may be favored for vascular targeting than traditional nanospheres with sizes ranging from 10 nm to 100 nm. Charoenphol and coworkers also examined the effect of particle size on margination dynamics and their results provide support to the fact that larger-sized spherical particles marginate to vessels walls more effectively than their smaller-sized counterparts.[43] In their *in vivo* study, they used ApoE-/- mice aortas to investigate the adhesion of 0.5 μm and 2 μm vascular-targeted (sialyl lewis A and anti-VCAM-1) fluorescent polystyrene spheres. Results from the study indicated that 2 μm particle adhesion densities were 2.5 – 3.5-fold higher in all major segments of mice aorta than the 0.5 μm spheres, pointing to better margination efficiency for the 2 μm spheres.

It should be noted that theoretical models have predicted that within a capillary flow, adhesion strength reduces as spherical particle diameter increases (d > ~560 nm) because of higher dislodging forces experienced by larger spherical particles,[47] so it may be unlikely that adhesion strength would be particularly relevant in the Charoenphol study. Also, the surface density of ligand/antibody was the same for both spherical particles. In any case, regardless of the site-specific targeting moiety used on a nanoparticle, if it does not have substantial margination efficiency it would not be able to reach the vicinity of vessel walls to make contact with potential receptors. In the Charoenphol study, gravity would more than likely play a role in the margination of the larger spherical particles to the vessel walls since gravitational forces become more significant as particle size increases (d > 500 nm).[40, 48] Another point worth mentioning is that a mere increase in size does not always necessitate better margination efficiency because other factors like the relative particle density, Brownian diffusion or van der Waals interaction forces can affect margination to vessel walls.[40, 44, 49]

For instance, an increase in size of the neutrally-buoyant nanoparticles (10 nm, 50 nm and 100 nm) from the above-discussed simulation work of Lee and coworkers did not show any significant improvement in margination efficiency and all nanoparticles ultimately resided in the vessel core. In a study by Toy and coworkers,[44] increasing the size of neutrally-buoyant liposomes (65 nm, 100 nm and 130 nm) caused a decrease in margination to vessel walls in experiments that utilized a fibronectin-coated polydimethylsiloxane microchannel for monitoring margination dynamics. Given that the contribution of gravity was neglected for these liposomes, the decrease in margination was reasoned to be attributed to larger momentum values exceeding the diffusion component of the liposomes towards the channel walls. Decuzzi and coworkers[49] used theoretical models to study the margination of particles to blood vessel walls and they demonstrated that a critical radius value exist by which time to margination would increase up to this value before decreasing past this critical point (Figure 1.3). The

model showed that the critical radius was dependent on the relative density of the particle to blood to the effect that when relative density decreased the critical radius increased. Furthermore, as the relative density decreased van der Waals forces became more dominant for nanoscale particles. In other words, the critical radius would be higher for particles with densities closer to that of blood with buoyancy being less of an influence as particle size decreased to the nanoscale. Therefore, it could be possible that the sizes of the liposomes studied in Toy and coworkers' study was well away from its critical radius for the experimental setup. It should be pointed out, however, that both the Toy and Decuzzi study were undertaken with the exclusion of blood components which are crucial to margination dynamics since particle collisions with red blood cells could also affect lateral displacement to the red blood cell-free layer.[41]

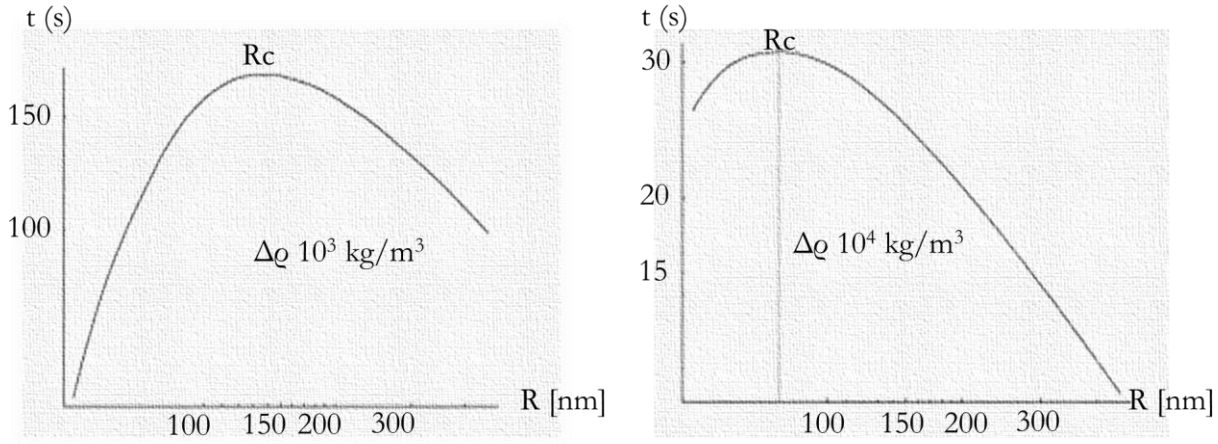


Figure 1.3 Time to margination as a function of particle radius for $\Delta\rho = 10^3$ and 10^4 relative density values. Adapted from ref.[49]

An *in vivo* study by D'Apolitio and coworkers[45] was conducted to determine the effect of particle shape on the margination of fluorescently labeled poly(lactic-co-glycolic acid) (PLGA) microparticles in skin vessels of

transgenic Tie2-green fluorescent protein (GFP expressed on vascular endothelium) mice. They employed intravital confocal microscopy to visualize the flow dynamics of PLGA spheres (1 μm), discs (d: 1 μm x h: 400 nm) and rods (d: 400 nm x h: 1.8 μm) of equal volume. Their findings indicated that the rods had the lowest margination propensity while discoidal and spherical microparticles had similar margination propensity. In another work by Thompson and coworkers,[46] the margination propensity of spherical and rod-shaped particles of different equivalent spherical diameters (ESDs) and aspect ratios (ARs) was studied under blood flow in a parallel plate flow chamber lined with human umbilical vein endothelial cells. Results from the experiments showed that rod-shaped particles with high ARs ≥ 9 (and ESDs ≥ 1 μm) had better margination propensity – as measured by particle wall binding – than equivalent spheres particularly at high shear rates and disturbed flow profiles. Nanorods (500 nm ESD), however, did not show any improvement in particle wall binding when compared with equivalent spheres, even at high ARs.

It should be mentioned that confocal imaging from experiments run under laminar blood flow (30% hematocrit) and at the highest wall shear rate revealed that there was no difference in localization of rod-shaped particles (AR 4 and 9) or equivalent spheres to the red blood cell-free layer for particles with an ESD of 2 μm. However, there was decreased localization for rod-shaped particles for the highest AR studied (AR = 11) when compared with equivalent spheres at an ESD of 1 μm. These experiments suggest that particle adhesion improved the results observed for rod-shaped particles. This brings up an important point of separating particle margination from particle adhesion since the latter is influenced by other factors such as particle ligand/antibody distribution, receptor density, binding strength etc. To better understand relationships between specific nanoparticle properties and margination in blood flow, studies need to clearly distinguish between particle margination and particle adhesion to prevent confounding by the latter.

1.2.2.2 Effect of Particle Size and Shape on Cellular Uptake

Following nanoparticle margination and site-specific adhesion, nanoparticles have to interact with the extracellular matrix or external membranes of target cells and then traverse this plasma membrane to deliver their therapeutic payload through endocytosis. Endocytosis can be classified according to different mechanisms as determine by cell type, nanoparticle-biomolecular corona or other targeting moieties.[21,50] Broadly speaking, the process would involve the wrapping of nanoparticles by the cell membrane for membrane budding that is subsequently pinched off to form an endocytic vesicle, followed by sorting and trafficking of the endosomal contents to other specialized intracellular compartments.[50] Since nanoparticle cellular internalization and compartmentalization are essential in governing the successful delivery of its cargo, it is important to understand how nanoparticle properties affect such processes.

Jiang and coworkers studied the cellular internalization of Herceptin-coated gold and silver nanospheres (2 – 100 nm) in human breast cancer SK-BR-3 cells overexpressing ErbB2 receptor.[51] Their study showed that size played an important role in cellular uptake with the 40 nm and 50 nm sized nanospheres having the most significant uptake. The increased internalization observed for these nanoparticle sizes was attributed to the greater affinity for the receptor binding sites. As size increased, so did the affinity of the nanoparticles for the receptor binding sites. However, the decrease in internalization observed for the larger-sized nanoparticles was ascribed to limited membrane wrapping. In another study, Lu and coworkers investigated the cellular internalization of mesoporous silica nanospheres (30 – 280 nm) in HeLa cells.[52] Results of the study indicated that 50 nm-sized particles were highly internalized by HeLa cells with cellular uptake in the following order 50 > 30 > 110 > 280 > 170 nm. Other researchers have also reported similar results with nanoparticle sizes around 50 nm being optimal

for cellular uptake;[53-59] however, this overall trend could possibly be a characteristic of non-phagocytic cells (Table 1.2). It is unclear if phagocytic cells display similar size-dependent uptake of nanospheres (Table 1.2).[55, 60-65]

Besides nanoparticle size, the nanoparticle shape can also have a significant impact on its cellular internalization. Barua and coworkers found that trastuzumab-coated polystyrene nanorods provided better cellular uptake than nanodiscs and nanospheres in BT-474 and SK-BR-3 breast cancer cell lines, with nanospheres exhibiting the lowest uptake.[66] The increased uptake of nanorods over nanodiscs and nanospheres was ascribed to higher multivalent binding of trastuzumab to cell receptors as a result of increased contact area with the cell surface. Uptake of uncoated polystyrene nanorods and nanodiscs were less than nanospheres in tests with BT-474 cells pointing perhaps to enhanced coating and presentation of trastuzumab-coated nonspherical particles. Xinglu and coworkers probed the cellular uptake of mesoporous silica nanoparticles (MSNPs) of different ARs (AR = 1, AR = 2 and AR = 4) in A375 human melanoma cells and found that nanoparticles with larger ARs experienced higher and rapid internalization than nanoparticles with smaller ARs.[67] In contrast to these studies, Chithrani and coworkers have showed that rod-shaped gold nanoparticles exhibited lower cellular uptake in HeLa cells when compared with spherical gold nanoparticles (AR = 1 > AR = 3 > AR = 5).[68] They reasoned that the lower uptake of nanorods was possibly due to the presence of residual surfactant because the nanorods were fabricated with cetyl trimethylammonium bromide that may have not been completely removed from the surface of the gold nanorods. Another reason posited was that membrane wrapping could have taken longer for nanorods since in addition to the AR, the absolute size and/or volume of the particle could have affected cellular internalization kinetics.[69]

In terms of shape-dependent cellular uptake by phagocytic cells, Champion and Mitragotri have suggested that macrophages are able to use the local curvature of a particle at the point of initial contact to determine whether or not to initiate phagocytosis, or merely spread on the particle which they called “frustrated”

Table 1.2 Summary of size-dependent cellular uptake

Nanoparticle[a]	Size range (nm)	Optimal size (nm)	Cell line	Reference
Gold	2 – 90	40, 50	SK-BR-3	[51]
Silver	5 – 90	40, 50	SK-BR-3	[51]
MSN	30 – 280	50	HeLa	[52]
PS	20 – 100	40	1321N1, A549	[53]
Gold	45 – 110	45	HeLa, CL1-0	[54]
Gold	16 – 58	40[b]	Raw 264.7, HepG2	[55]
Gold	10 – 50	50	NRK	[56]
Gold	25 – 50	50	PANC1, Jurkat	[57]
LDH	50 – 350	50	MNNG/HOS	[58]
Silica	20 – 200	60	A549, HepG2, NIH/3T3	[59]
PSCOOH	20 – 200	20	J774.A1	[60]
PVP-IO	8 – 65	37	Raw 264.7	[61]
PSCOOH	40 – 2000	40	Raw 264.7, HeLa A549, 1321N1, hCMEC/D3	[62]
Dextran-coated SPIO	62 – 394	394	HMDM	[63]
Silica-coated IO	30 – 120	None	HMDM, MDDC	[64]
Dextran-coated SPIO	20, 50	None	HMDM	[64]
Silver[c]	20 – 75	20	THP-1	[65]
Silver[d]	20 – 75	50, 75	THP-1	[65]

(a) All spherical particles. (b) Positively charged gold nanoparticles displayed no size-dependent uptake. (c) Without fetal calf serum treatment. (d) With fetal calf serum treatment. MSN – mesoporous silica nanoparticles; PS – polystyrene; LDH – layered double hydroxide; PSCOOH – carboxylate-functionalized polystyrene; PVP-IO – Polyvinylpyrrolidone-coated iron oxide; SPIO – superparamagnetic iron oxide.

phagocytosis.[70] They studied the phagocytosis of six different shapes (prolate ellipsoid, oblate ellipsoid, elliptical disc, rectangular disc, UFO and spheres) in NR8383 alveolar rat macrophages and determined the success of phagocytosis by two dimensionless parameters, Ω and V^*, where Ω was related to the shape of the particle and the point of attachment on the macrophage while V^* was defined as the ratio of the particle volume to macrophage volume. The authors used a phase diagram (Figure 1.4) to illustrate the regions of successful internalization ($\Omega \leq 45°$, $V^* \leq 1$), unsuccessful internalization ($\Omega \leq 45°$, $V^* \geq 1$) and spreading ($\Omega > 45°$). Their results suggested that shape played a major role in the induction of the phagocytosis process and size mainly affected total particle engulfment when the volume of the particle was greater than that of the macrophages.

Padmore and coworkers reported frustrated phagocytosis after the exposure of short and long glass fibers to murine alveolar macrophages.[71] They identified critical lengths (12 μm and 27 μm, d ~0.8 μm) by which frustrated phagocytosis occurred by fitting dose-response curves of stimulated cytokines (IL-1α and TNF-α) to short and long glass fiber populations. Differences in critical lengths stemmed from the potency and weighting of short and long glass fibers towards cytokine response. Concerning the overall uptake, their investigations showed that macrophage internalization events were less for longer fibers when compared with shorter fibers.

Analyses by other researchers also indicated that using higher AR or elongated particles increased the possibility of frustrated phagocytosis and/or immune evasion.[72-75] However, for successfully phagocytosed nonspherical particles, high AR has also been associated with increased uptake, but this alone does not determine the total amount of particles internalized as discussed earlier for non-phagocytic cells. For example, Arnida and coworkers[76] found that PEGylated gold nanorods were less readily internalized than PEGylated nanospheres in RAW 264.7 macrophages, but in another work by Bartneck and coworkers[77] they obtained contrasting results for the uptake of neutral gold nanorods and nanospheres by human blood macrophages. Also, cellular uptake in

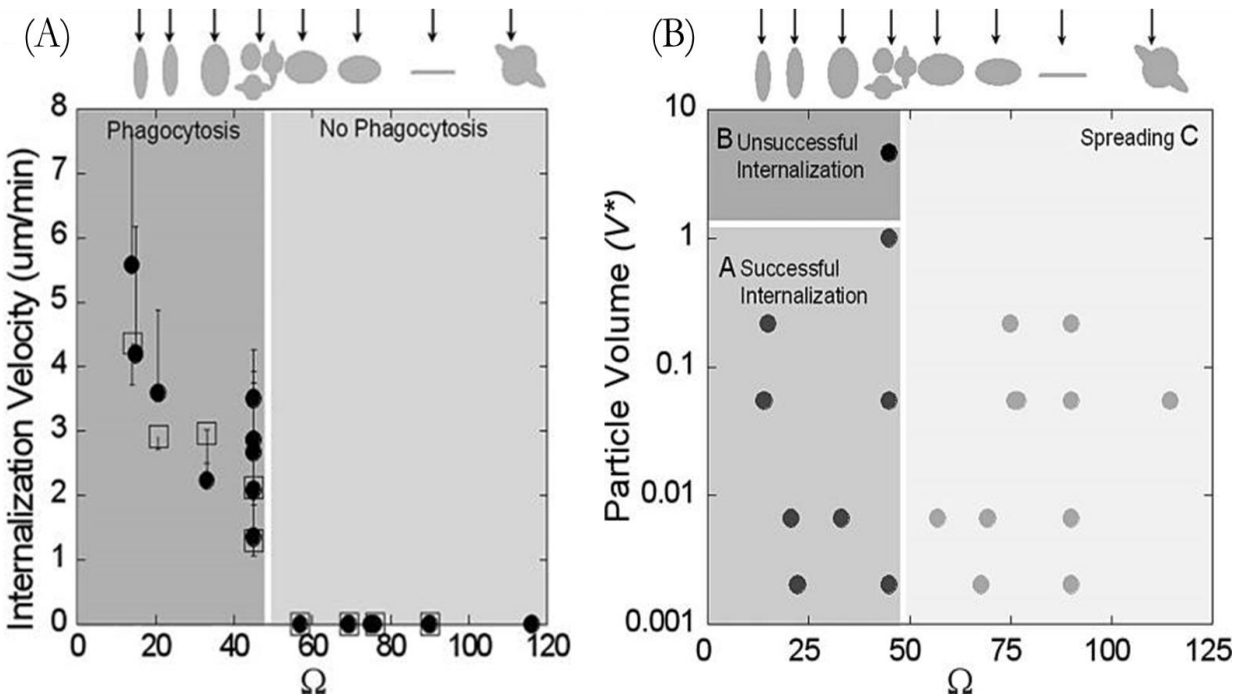


Figure 1.4 (A) The relationship between internalization velocity and Ω for different nanoparticle shapes. (B) Phagocytosis phase diagram for the different nanoparticle shapes. Adapted from ref.[70]

human blood macrophages was comparable for amine- and carboxyl-terminated PEGylated gold nanorods and nanospheres, thus particle shape did not influence the uptake of these nanoparticles.

In summary, literature suggests that nanoparticle shape and size can be exploited to increase or decrease the cellular uptake of nanoparticles. Although general conclusions can be made regarding the size and shape of nanoparticles, a better understanding of the interplay of nanoparticle characteristics, cell type and mechanism of internalization is needed for the rational design of drug delivery vehicles. In addition, *in vitro* research that closely resembles physiological conditions should be considered in future developments.

1.2.2.3 Effect of Particle Size and Shape on Biodistribution

Nanoparticles injected intravenously have to pass through the hurdles of the body's immune system, that includes the mononuclear phagocyte system, to eventually reach their intended destination. Major organs of the body that are associated with the mononuclear phagocyte system, such as the liver and spleen, have filters that could preclude nanoparticle delivery to desired regions. The liver embodies discontinuous endothelia with vascular fenestrations that have sizes that range from 50 – 180 nm,[78] while the spleen has interendothelial cell slits that range in size from 200 – 500 nm.[79] Kidneys have a glomerular filtration system that utilize fenestrated blood capillaries and podocyte slit diaphragms to filter particles that are < 5 nm,[80] and the lungs are known to have micrometer-sized particles readily accumulate within its capillaries.[81] Nanoparticles generally experience rapid clearance from the aforementioned organs based on the cut-off pore size of the organ's filtration system, unless the particles' material structure and fluid dynamics are such that they allow extension and alignment with the flow of blood or streamlines around macrophages, as is the case with flexible filamentous polymer micelle assemblies (also known as filomicelles).[72]

Discher and coworkers showed that longer filomicelles composed of a hydrophilic poly-ethylene glycol (PEG) corona and either a hydrophobic core of biodegradable polycaprolactone (PCL) or inert poly-ethyl-ethylene were able to persist in circulation for longer periods of time when compared with shorter filomicelles (L_0, 18 μm ≥ 8 μm > 4 μm > 2 μm; d_0, 22 nm to 60 nm) and spherical vesicles.[72] Filomicelles of greater contour lengths were able to stay in circulation for up to a week while their spherical counterparts were cleared within 2 days, and this difference could have been due to the breakdown of the longer filomicelles into smaller fragments coupled with inefficient uptake of the particles by phagocytic cells. Biodistribution of the particles in Sprague-Dawley rats following 4 days after intravenous injection displayed the highest distribution of the PCL filomicelles (L_0 = 4 μm or 8 μm) in the liver and spleen, with distributions to the lungs and kidneys to a lesser extent.

In another study by Discher and coworkers,[82] they compared the ability of paclitaxel loaded filomicelles and spherical micelles to shrink xenografted tumors (human lung carcinoma cell line, A549) in Ncr nude mice. Their study demonstrated that filomicelles were able to increase the maximum tolerated dose of paclitaxel relative to spherical micelles, and the paclitaxel loaded filomicelles had the most inhibitory effect on tumor growth possibly due to the higher dose and the ability of filomicelles to reptate into the leaky tumor vasculature. Besides, following 24 hours of injection with filomicelles and spherical micelles of the same paclitaxel dose (8 mg/kg), the filomicelles exhibited greater tumor/organ selectivity when compared with spherical micelles. The effect of this selectivity could be observed in the percent change of tumor/organ apoptosis from utilizing spherical micelles and filomicelles following 22 days of multiple 8 mg/kg injections: tumor/liver, +29%; tumor/kidney, +31%; tumor/spleen, +38%; tumor/heart, +60% and tumor/lung, +61%.

A recent study reported by Kaga and coworkers[83] to investigate the influence of size and shape on the biodistribution of poly(glycidyl methacrylate)-*b*-poly(oligo- (ethylene glycol) methyl ether methacrylate)-*b*-

polystyrene (PGMA-*b*-POEGMA-*b*-PS) block copolymer nanoparticles demonstrated higher degrees of accumulation in the liver and spleen as the overall nanoparticle size increased. The nanoparticle form and dimensions are as follows: spherical micelles, d: 21 nm and 33 nm; rodlike micelles, d: 37 nm, contour length: 350 nm – 450 nm; wormlike micelles, d: 45 nm, contour length: 1 – 2 μm. Biodistribution of nanoparticles in the HT1080 tumor-bearing athymic nude mice also showed that most of the nanoparticles were cleared from the blood within 2 days, and nanoparticle tumor accumulation decreased as overall nanoparticle size increased. Additionally, wormlike micelles had the most accumulation in the lungs while the distribution of other nanoparticles decreased as overall size increased. The smaller spherical micelles (21 nm) also had the highest biodistribution in the kidneys, pancreas and heart.

Müllner and coworkers[84] found that increasing the rigidity and aspect ratio of cylindrical polymer brushes (PEGMA-*co*-GMA, PCL-*b*-(PEGMA-*co*-GMA)) produced greater plasma clearance following intravenous injection in rats. This greater plasma clearance for higher AR cylindrical polymer brushes is in contrast to the works by Discher and coworkers where higher ARs for filomicelles resulted in greater circulation times. Such disparity could stem from the stability of the backbone of the cylindrical polymer brushes employed by Müllner and coworkers as opposed to the self-assembled filomicelles from the works of the Discher and coworkers that experienced fragmentation following intravenous injection, thus supporting their prolonged residence in circulation. Apart from an increase in clearance, the higher AR cylindrical polymer brushes also brought about greater deposition in mononuclear phagocyte system (MPS) organs with the most notable uptake occurring in the liver and spleen.

Decuzzi and coworkers examined the influence of size (700 nm – 3 μm) and shape (discoidal, spherical, hemispherical and cylindrical; $v \approx 0.6\ \mu m^3$) on the biodistribution of silica or silicon nanoparticles in xenografted MDA-MB-231 tumor-bearing nu/nu nude mice.[81] Their investigations showed that majority of the spherical

particles accumulated in the liver, lung and spleen. At a higher dose, the smallest spherical particle, 700 nm, had the most accumulation in the liver and the larger spherical particles, 2.5 μm and 3.0 μm, had significant accumulation in the lungs as expected. Tumor accumulation decreased as spherical particle size increased. Discoidal particles were shown to accumulate significantly more in the lungs and heart when compared with hemispherical, cylindrical and spherical particles. On the other hand, cylindrical particles accumulated significantly more in the liver when compared with other non-spherical and spherical particles. There was higher accumulation of discoidal and hemispherical particles in the spleen when compared with cylindrical and spherical particles. No significant differences in shape effects were found for particle accumulation in the brain, kidneys and tumor. It is possible that the higher accumulations observed for discoidal particles in most organs were as a result of better margination propensity; however, lower accumulations for the liver was attributed to the inability of liver macrophages to engulf the particles because of their elongated shapes.

Black and coworkers studied the biodistribution of 50 nm PEGylated radioactive gold particles of different shapes (nanodiscs, nanospheres, nanorods and nanocages) in EMT6 tumor-bearing Balb/c mice.[85] Twenty-four hours post intravenous injection, the nanostructures were mainly distributed to the liver and spleen. Nanodiscs and nanocages displayed greater accumulation in the lungs and spleen when compared with other nanoparticle shapes, while nanospheres and nanocages had higher accumulations in the heart than the other nanostructures. Tumor deposition was highest for the nanospheres and this may have been due to increased retention of nanospheres in blood circulation and a lower clearance by the liver and spleen. Nanorods exhibited the lowest tumor deposition (nanospheres > nanocages > nanodiscs > nanorods) and this was attributed to the low coverage density of PEG on the particle surface.

Overall, these studies indicate that PEGylation increases the circulation time of nanoparticles in the body and that size and shape play important roles in biodistribution. In order to effectively target specific organs, particle size and shape need to be tailored to maximize delivery. In the case of tumors, smaller nanoparticles would be ideal for enhanced permeability but changes to the tumor microenvironment may also change the effective size for tumor uptake. Therefore, in order to exploit the nanomaterial's properties, careful consideration of the nature of the disease and desired target should help guide nanoparticle design.

1.3 Conclusions

With the ultimate goal of designing drug delivery systems to deliver their cargos to specific targets, the efforts that have been made to accomplish this prove that recognition by the immune system or opsonization are still major obstacles to successful developments. Changes in the metabolic state of an individual have therefore become an essential component to consider when evaluating therapeutic options to be administered because this could affect drug delivery.

Nanoparticle technologies for drug delivery are growing and the rational design of these technologies to overcome the above barriers to effective treatment require that we understand the relationship between nanoparticle properties, biomolecules in different biological environments, the biomolecular corona, and the complexities surrounding the disease. The use of particle fabrication methods to form and modify nanoparticle shapes are becoming increasingly relevant to achieve this particular aim. Not only are particle sizes and shapes important parameters that determine margination efficiency to vessel walls, they are also crucial properties that can be exploited to evade recognition by the immune system. The AR of nanoparticles can be adjusted to "frustrate" phagocytosis and decrease cellular internalization. Generally, nanoparticles of higher AR can be used to this effect

and PEGylation of nanoparticles also offer steric hindrance against opsonization and tend to promote increased blood residence time. Sequestration of nanoparticles by MPS organs can thus be limited for prolonged periods, sometimes up to days, thereby increasing the probability of nanoparticles arriving at their destination.

Although nanoparticle fabrication techniques exist that are geared to evade the immune system, there is still more work to be done to deepen our understanding of how the biomolecular corona formed on nanoparticle surfaces affects such opsonization and subsequent biodistribution. Numerous nanomaterials are available, and the biomolecular corona composition varies based on the properties of these nanomaterials. However, lipoproteins and the like are major constituents of many nanoparticle biomolecular coronas and should be investigated in further detail. This would be particularly important since lipid metabolism and lipoprotein receptors may be major aspects affecting nanoparticle drug delivery efficacy. Consequently, it is of paramount importance that we establish key elements governing the interconnectedness between metabolic conditions, nanoparticle corona formation and biodistribution that will allow for a rational design strategy and the potential for personalized medicine.

References

1. *Global Health Estimates 2016: Deaths by Cause, Age, Sex, by Country and by Region, 2000-2016*; World Health Organization: Geneva, 2018.
2. *World health statistics 2018: monitoring health for the SDGs, sustainable development goals*; World Health Organization: Geneva, 2018. Licence: CC BY-NC-SA 3.0 IGO.
3. Hruby, A.; Hu, F. B., The Epidemiology of Obesity: A Big Picture. *Pharmacoeconomics* **2015,** *33* (7), 673-689.
4. Romieu, I.; Dossus, L.; Barquera, S.; Blottière, H. M.; Franks, P. W.; Gunter, M.; Hwalla, N.; Hursting, S. D.; Leitzmann, M.; Margetts, B.; Nishida, C.; Potischman, N.; Seidell, J.; Stepien, M.; Wang, Y.; Westerterp, K.; Winichagoon, P.; Wiseman, M.; Willett, W. C., Energy balance and obesity: what are the main drivers? *Cancer Causes & Control* **2017,** *28* (3), 247-258.
5. *Global Health Observatory: Overweight and Obesity, 1975-2016*; World Health Organization: Geneva, 2018.
6. Kelly, T.; Yang, W.; Chen, C.-S.; Reynolds, K.; He, J., Global burden of obesity in 2005 and projections to 2030. *International Journal of Obesity* **2008,** *32*, 1431-1437.
7. Finkelstein, E. A.; Khavjou, O. A.; Thompson, H.; Trogdon, J. G.; Pan, L.; Sherry, B.; Dietz, W., Obesity and severe obesity forecasts through 2030. *American Journal of Preventive Medicine* **2012,** *42* (6), 563-570.
8. Wang, Y.; Beydoun, M. A.; Liang, L.; Caballero, B.; Kumanyika, S. K., Will all Americans become overweight or obese? estimating the progression and cost of the US obesity epidemic. *Obesity* **2008,** *16* (10), 2323-2330.
9. Yan, X.; Kuipers, F.; Havekes, L. M.; Havinga, R.; Dontje, B.; Poelstra, K.; Scherphof, G. L.; Kamps, J. A., The role of apolipoprotein E in the elimination of liposomes from blood by hepatocytes in the mouse. *Biochemical and Biophysical Research Communications* **2005,** *328* (1), 57-62.
10. Cukalevski, R.; Lundqvist, M.; Oslakovic, C.; Dahlbäck, B.; Linse, S.; Cedervall, T., Structural Changes in Apolipoproteins Bound to Nanoparticles. *Langmuir* **2011,** *27* (23), 14360-14369.
11. Dell'Orco, D.; Lundqvist, M.; Oslakovic, C.; Cedervall, T.; Linse, S., Modeling the Time Evolution of the Nanoparticle-Protein Corona in a Body Fluid. *PLoS One* **2010,** *5* (6), e10949.
12. Hellstrand, E.; Lynch, I.; Andersson, A.; Drakenberg, T.; Dahlbäck, B.; Dawson, K. A.; Linse, S.; Cedervall, T., Complete high-density lipoproteins in nanoparticle corona. *Federation of European Biochemical Societies* **2009,** *276*, 3372-3381.
13. Ganesan, L. P.; Mates, J. M.; Cheplowitz, A. M.; Avila, C. L.; Zimmerer, J. M.; Yao, Z.; Maiseyeu, A.; Rajaram, M. V. S.; Robinson, J. M.; Anderson, C. L., Scavenger receptor B1, the HDL receptor, is expressed abundantly in liver sinusoidal endothelial cells. *Scientific Reports* **2016,** *6*, 20646.
14. Vaisman, B. L.; Demosky, S. J.; Stonik, J. A.; Ghias, M.; Knapper, C. L.; Sampson, M. L.; Dai, C.; Levine, S. J.; Remaley, A. T., Endothelial expression of human ABCA1 in mice increases plasma HDL cholesterol and reduces diet-induced atherosclerosis. *Journal of Lipid Research* **2012,** *53* (1), 158-167.
15. Nel, A. E.; Mädler, L.; Velegol, D.; Xia, T.; Hoek, E. M. V.; Somasundaran, P.; Klaessig, F.; Castranova, V.; Thompson, M., Understanding biophysicochemical interactions at the nano–bio interface. *Nature Materials* **2009,** *8*, 543-557.

16. Alexis, F.; Pridgen, E.; Molnar, L. K.; Farokhzad, O. C., Factors Affecting the Clearance and Biodistribution of Polymeric Nanoparticles. *Molecular Pharmaceutics* **2008,** *5* (4), 505-515.
17. Nanjappa, V.; Thomas, J. K.; Marimuthu, A.; Muthusamy, B.; Radhakrishnan, A.; Sharma, R.; Khan, A. A.; Balakrishnan, L.; Sahasrabuddhe, N. A.; Kumar, S.; Jhaveri, B. N.; Sheth, K. V.; Khatana, R. K.; Shaw, P. G.; Srikanth, S. M.; Mathur, P. P.; Shankar, S.; Nagaraja, D.; Christopher, R.; Mathivanan, S.; Raju, R.; Sirdeshmukh, R.; Chatterjee, A.; Simpson, R. J.; Harsha H. C.; Pandey, A.; Keshava Prasad T. S., Plasma Proteome Database as a resource for proteomics research: 2014 update. *Nucleic Acids Research* **2014,** *42* (Database issue), D959-D965.
18. Ke, P. C.; Lin, S.; Parak, W. J.; Davis, T. P.; Caruso, F., A Decade of the Protein Corona. *ACS Nano* **2017,** *11*, 11773-11776.
19. Tenzer, S.; Docter, D.; Kuharev, J.; Musyanovych, A.; Fetz, V.; Hecht, R.; Schlenk, F.; Fischer, D.; Kiouptsi, K.; Reinhardt, C.; Landfester, K.; Schild, H.; Maskos, M.; Knauer, S. K.; Stauber, R. H., Rapid formation of plasma protein corona critically affects nanoparticle pathophysiology. *Nature Nanotechnology* **2013,** *8*, 772-781.
20. Lundqvist, M.; Stigler, J.; Cedervall, T.; Berggård, T.; Flanagan, M. B.; Lynch, I.; Elia, G.; Dawson, K., The Evolution of the Protein Corona around Nanoparticles: A Test Study. *ACS Nano* **2011,** *5* (9), 7503-7509.
21. Monopoli, M. P.; Åberg, C.; Salvati, A.; Dawson, K. A., Biomolecular coronas provide the biological identity of nanosized materials. *Nature Nanotechnology* **2012,** *7*, 779-786.
22. Nguyen, V. H.; Lee, B.-J., Protein corona: a new approach for nanomedicine design. *International Journal of Nanomedicine* **2017,** *12*, 3137-3151.
23. Peng, Q.; Zhang, S.; Yang, Q.; Zhang, T.; Wei, X. Q.; Jiang, L.; Zhang, C. L.; Chen, Q. M.; Zhang, Z. R.; Lin, Y. F., Preformed albumin corona, a protective coating for nanoparticles based drug delivery system. *Biomaterials* **2013,** *34* (33), 8521-8530.
24. Amici, A.; Caracciolo, G.; Digiacomo, L.; Gambini, V.; Marchini, C.; Tilio, M.; Capriotti, A. L.; Colapicchioni, V.; Matassa, R.; Familiari, G.; Palchetti, S.; Pozzi, D.; Mahmoudi, M.; Laganà, A., *In vivo* protein corona patterns of lipid nanoparticles. *Royal Society of Chemistry Advances* **2017,** *7*, 1137-1145.
25. Bertrand, N.; Grenier, P.; Mahmoudi, M.; Lima, E. M.; Appel, E. A.; Dormont, F.; Lim, J.-M.; Karnik, R.; Langer, R.; Farokhzad, O. C., Mechanistic understanding of in vivo protein corona formation on polymeric nanoparticles and impact on pharmacokinetics. *Nature Communications* **2017,** *8*, 1-8.
26. Hajipour, M. J.; Laurent, S.; Aghaie, A.; Rezaee, F.; Mahmoudi, M., Personalized protein coronas: a "key" factor at the nanobiointerface. *Biomaterials Science* **2014,** *2* (9), 1210-1221.
27. Anderson, N. L.; Anderson, N. G., The Human Plasma Proteome History, Character, and Diagnostic Prospects. *Molecular & Cellular Proteomics* **2002,** *1* (11), 845-867.
28. Liu, R.; Jiang, W.; Walkey, C. D.; Chan, W. C. W.; Cohen, Y., Prediction of nanoparticles-cell association based on corona proteins and physicochemical properties. *Nanoscale* **2015,** *7*, 9664-9675.
29. Palchetti, S.; Digiacomo, L.; Pozzi, D.; Peruzzi, G.; Micarelli, E.; Mahmoudi, M.; Caracciolo, G., Nanoparticles-cell association predicted by protein corona fingerprints. *Nanoscale* **2016,** *8*, 12755-12763.
30. Walkey, C. D.; Olsen, J. B.; Song, F.; Liu, R.; Guo, H.; Olsen, D. W. H.; Cohen, Y.; Emili, A.; Chan, W. C. W., Protein Corona Fingerprinting Predicts the Cellular Interaction of Gold and Silver Nanoparticles. *ACS Nano* **2014,** *8* (3), 2439-2455.
31. Kamath, P.; Fernandez, A.; Giralt, F.; Rallo, R., Predicting Cell Association of Surface-Modified Nanoparticles Using Protein Corona Structure - Activity Relationships (PCSAR). *Current Topics in Medicinal Chemistry* **2015,** *15* (18), 1930-1937.

32. Lin, Z.; Monteiro-Riviere, N. A.; Kannan, R.; Riviere, J. E., A computational framework for interspecies pharmacokinetics, exposure and toxicity assessment of gold nanoparticles. *Nanomedicine (Lond.)* **2016,** *11* (2), 107-119.
33. Sahneh, F. D.; Scoglio, C. M.; Monteiro-Riviere, N. A.; Riviere, J. E., Predicting the impact of biocorona formation kinetics on interspecies extrapolations of nanoparticle biodistribution modeling. *Nanomedicine (Lond.)* **2015,** *10* (1), 25-33.
34. Walkey, C. D.; Chan, W. C. W., Understanding and controlling the interaction of nanomaterials with proteins in a physiological environment. *Chemical Society Reviews* **2012,** *41*, 2780-2799.
35. Shah, A. S.; Tan, L.; Long, J. L.; Davidson, W. S., Proteomic diversity of high density lipoproteins: our emerging understanding of its importance in lipid transport and beyond. *Journal of Lipid Research* **2013,** *54* (10), 2575-2585.
36. Davidson, W. S. Davidson Lab Webpage: Lipoprotein Proteome Watch. www.DavidsonLab.com (accessed July 17, 2018).
37. Lundqvist, M.; Stigler, J.; Elia, G.; Lynch, I.; Cedervall, T.; Dawson, K. A., Nanoparticle size and surface properties determine the protein corona with possible implications for biological impacts. *Proceedings of the National Academy of Sciences* **2008,** *105* (38), 14265-14270.
38. Tan, J.; Shah, S.; Thomas, A.; Ou-Yang, H. D.; Liu, Y., The influence of size, shape and vessel geometry on nanoparticle distribution. *Microfluid Nanofluidics* **2013,** *14* (1-2), 77-87.
39. Shah, S.; Liu, Y.; Hu, W.; Gao, J., Modeling Particle Shape-Dependent Dynamics in Nanomedicine. *Journal of Nanoscience and Nanotechnology* **2011,** *11* (2), 919-928.
40. Lee, S.-Y.; Ferrari, M.; Decuzzi, P., Shaping nano-/micro-particles for enhanced vascular interaction in laminar flows. *Nanotechnology* **2009,** *20* (49), 1-11.
41. Vahidkhaha, K.; Bagchi, P., Microparticle shape effects on margination, near-wall dynamics and adhesion in a three-dimensional simulation of red blood cell suspension. *Soft Matter* **2015,** *11* (11), 2097-2109.
42. Lee, T.-R.; Choi, M.; Kopacz, A. M.; Yun, S.-H.; Liu, W. K.; Decuzzi, P., On the near-wall accumulation of injectable particles in the microcirculation: smaller is not better. *Scientific Reports* **2013,** *3*, 1-8.
43. Charoenphol, P.; Mocherla, S.; Bouis, D.; Namdee, K.; Pinsky, D. J.; Eniola-Adefeso, O., Targeting therapeutics to the vascular wall in atherosclerosis–Carrier size matters. *Atherosclerosis* **2011,** *217* (2), 364-370.
44. Toy, R.; Hayden, E.; Shoup, C.; Baskaran, H.; Karathanasis, E., Effect of Particle Size, Density and Shape on Margination of Nanoparticles in Microcirculation. *Nanotechnology* **2011,** *22* (11), 1-18.
45. D'Apolito, R.; Tomaiuolo, G.; Taraballi, F.; Minardi, S.; Kirui, D.; Liu, X.; Cevenini, A.; Palomba, R.; Ferrari, M.; Salvatore, F.; Tasciotti, E.; Guido, S., Red blood cells affect the margination of microparticles in synthetic microcapillaries and intravital microcirculation as a function of their size and shape. *Journal of Controlled Release* **2015,** *217*, 263-272.
46. Thompson, A. J.; Mastria, E. M.; Eniola-Adefeso, O., The margination propensity of ellipsoidal micro/nanoparticles to the endothelium in human blood flow. *Biomaterials* **2013,** *34* (23), 5863-5871.
47. Decuzzi, P.; Ferrari, M., The adhesive strength of non-spherical particles mediated by specific interactions. *Biomaterials* **2006,** *27*, 5307-5314.
48. Gentile, F.; Curcio, A.; Indolfi, C.; Ferrari, M.; Decuzzi, P., The margination propensity of spherical particles for vascular targeting in the microcirculation. *Journal of Nanobiotechnology* **2008,** *6* (9), 1-9.

49. Decuzzi, P.; Lee, S.; Bhushan, B.; Ferrari, M., A Theoretical Model for the Margination of Particles within Blood Vessels. *Annals of Biomedical Engineering* **2005,** *33* (2), 179-190.
50. Kumari, S.; Swetha, M. G.; Mayor, S., Endocytosis unplugged: multiple ways to enter the cell. *Cell Research* **2010,** *20*, 256-275.
51. Jiang, W.; Kim, B. Y. S.; Rutka, J. T.; Chan, W. C. W., Nanoparticle-mediated cellular response is size-dependent. *Nature Nanotechnology* **2008,** *3*, 145-150.
52. Lu, F.; Wu, S.-H.; Hung, Y.; Mou, C.-Y., Size Effect on Cell Uptake in Well-Suspended, Uniform Mesoporous Silica Nanoparticles. *Small* **2009,** *5* (12), 1408-1413.
53. Varela, J. A.; Bexiga, M. G.; Åberg, C.; Simpson, J. C.; Dawson, K. A., Quantifying size-dependent interactions between fluorescently labeled polystyrene nanoparticles and mammalian cells. *Journal of Nanobiotechnology* **2012,** *10* (39), 1-6.
54. Wang, S.-H.; Lee, C.-W.; Chiou, A.; Wei, P.-K., Size-dependent endocytosis of gold nanoparticles studied by three-dimensional mapping of plasmonic scattering images. *Journal of Nanobiotechnology* **2010,** *8* (33), 1-13.
55. Liu, X.; Huang, N.; Li, H.; Jin, Q.; Ji, J., Surface and Size Effects on Cell Interaction of Gold Nanoparticles with Both Phagocytic and Nonphagocytic Cells. *Langmuir* **2013,** *29*, 9138-9148.
56. Ma, X.; Wu, Y.; Jin, S.; Tian, Y.; Zhang, X.; Zhao, Y.; Yu, L.; Liang, X.-J., Gold Nanoparticles Induce Autophagosome Accumulation through Size-Dependent Nanoparticle Uptake and Lysosome Impairment. *ACS Nano* **2011,** *5* (11), 8629-8639.
57. Sabuncu, A. C.; Grubbs, J.; Qian, S.; Abdel-Fattah, T. M.; Stacey, M. W.; Beskok, A., Probing nanoparticle interactions in cell culture media. *Colloids and Surfaces B: Biointerfaces* **2012,** *95*, 96-102.
58. Oh, J.-M.; Choi, S.-J.; Lee, G.-E.; Kim, J.-E.; Choy, J.-H., Inorganic Metal Hydroxide Nanoparticles for Targeted Cellular Uptake Through Clathrin-Mediated Endocytosis. *Chemistry - An Asian Journal* **2009,** *4*, 67-73.
59. Kim, I.-Y.; Joachim, E.; Choi, H.; Kim, K. K., Toxicity of silica nanoparticles depends on size, dose, and cell type. *Nanomedicine: Nanotechnology, Biology and Medicine* **2015,** *11* (6), 1407-1416.
60. Clift, M. J. D.; Rothen-Rutishauser, B.; Brown, D. M.; Duffin, R.; Donaldson, K.; Proudfoot, L.; Guy, K.; Stone, V., The impact of different nanoparticle surface chemistry and size on uptake and toxicity in a murine macrophage cell line. *Toxicology and Applied Pharmacology* **2008,** *232* (3), 418-427.
61. Huang, J.; Bu, L.; Xie, J.; Chen, K.; Cheng, Z.; Li, X.; Chen, X., Effects of Nanoparticle Size on Cellular Uptake and Liver MRI with Polyvinylpyrrolidone-Coated Iron Oxide Nanoparticles. *ACS Nano* **2010,** *4* (12), 7151-7160.
62. dos-Santos, T.; Varela, J.; Lynch, I.; Salvati, A.; Dawson, K. A., Quantitative Assessment of the Comparative Nanoparticle-Uptake Efficiency of a Range of Cell Lines. *Small* **2011,** *7* (23), 3341-3349.
63. Beduneau, A.; Ma, Z.; Grotepas, C. B.; Kabanov, A.; Rabinow, B. E.; Gong, N.; Mosley, R. L.; Dou, H.; Boska, M. D.; Gendelman, H. E., Facilitated Monocyte-Macrophage Uptake and Tissue Distribution of Superparmagnetic Iron-Oxide Nanoparticles. *PLoS One* **2009,** *4* (2), e4343.
64. Kunzmann, A.; Andersson, B.; Vogt, C.; Feliu, N.; Ye, F.; Gabrielsson, S.; Toprak, M. S.; Buerki-Thurnherr, T.; Laurent, S.; Vahter, M.; Krug, H.; Muhammed, M.; Scheynius, A.; Fadeel, B., Efficient internalization of silica-coated iron oxide nanoparticles of different sizes by primary human macrophages and dendritic cells. *Toxicology and Applied Pharmacology* **2011,** *253* (2), 81-93.

65. Kettler, K.; Giannakou, C.; Jong, W. H. d.; Hendriks, A. J.; Krystek, P., Uptake of silver nanoparticles by monocytic THP-1 cells depends on particle size and presence of serum proteins. *Journal of Nanoparticle Research* **2016,** *18* (9), 286.
66. Barua, S.; Yoo, J.-W.; Kolhar, P.; Wakankar, A.; Gokarn, Y. R.; Mitragotri, S., Particle shape enhances specificity of antibody-displaying nanoparticles. *Proceedings of the National Academy of Sciences* **2013,** *110* (9), 3270-3275.
67. Huang, X.; Teng, X.; Chen, D.; Tang, F.; He, J., The effect of the shape of mesoporous silica nanoparticles on cellular uptake and cell function. *Biomaterials* **2010,** *31* (3), 438-448.
68. Chithrani, B. D.; Ghazani, A. A.; Chan, W. C. W., Determining the Size and Shape Dependence of Gold Nanoparticle Uptake into Mammalian Cells. *Nano Letters* **2006,** *6* (4), 662-668.
69. Chithrani, B. D.; Chan, W. C. W., Elucidating the Mechanism of Cellular Uptake and Removal of Protein-Coated Gold Nanoparticles of Different Sizes and Shapes. *Nano Letters* **2007,** *7* (6), 1542-1550.
70. Champion, J. A.; Mitragotri, S., Role of target geometry in phagocytosis. *Proceedings of the National Academy of Sciences* **2006,** *103* (13), 4930-4934.
71. Padmore, T.; Stark, C.; Turkevich, L. A.; Champion, J. A., Quantitative analysis of the role of fiber length on phagocytosis and inflammatory response by alveolar macrophages. *Biochimica et Biophysica Acta* **2017,** *1861* (2), 58-67.
72. Geng, Y.; Dalhaimer, P.; Cai, S.; Tsai, R.; Tewari, M.; Minko, T.; Discher, D. E., Shape effects of filaments versus spherical particles in flow and drug delivery. *Nature Nanotechnology* **2007,** *2*, 249-255.
73. Schinwald, A.; Murphy, F. A.; Prina-Mello, A.; Poland, C. A.; Byrne, F.; Movia, D.; Glass, J. R.; Dickerson, J. C.; Schultz, D. A.; Jeffree, C. E.; MacNee, W.; Donaldson, K., The Threshold Length for Fiber-Induced Acute Pleural Inflammation: Shedding Light on the Early Events in Asbestos-Induced Mesothelioma. *Toxicological Sciences* **2012,** *128* (2), 461-470.
74. Murphy, F. A.; Schinwald, A.; Poland, C. A.; Donaldson, K., The mechanism of pleural inflammation by long carbon nanotubes: interaction of long fibres with macrophages stimulates them to amplify pro-inflammatory responses in mesothelial cells. *Particle and Fibre Toxicology* **2012,** *9* (8), 1-15.
75. Huang, X.; Li, L.; Liu, T.; Hao, N.; Liu, H.; Chen, D.; Tang, F., The Shape Effect of Mesoporous Silica Nanoparticles on Biodistribution, Clearance, and Biocompatibility in Vivo. *ACS Nano* **2011,** *5* (7), 5390-5399.
76. Arnida; Janát-Amsbury, M. M.; Ray, A.; Peterson, C. M.; Ghandehari, H., Geometry and surface characteristics of gold nanoparticles influence their biodistribution and uptake by macrophages. *European Journal of Pharmaceutics and Biopharmaceutics* **2011,** *77* (3), 417-423.
77. Bartneck, M.; Keul, H. A.; Singh, S.; Czaja, K.; Bornemann, J.; Bockstaller, M.; Moeller, M.; Zwadlo-Klarwasser, G.; Groll, J., Rapid uptake of gold nanorods by primary human blood phagocytes and immunomodulatory effects of surface chemistry. *ACS Nano* **2010,** *4* (6), 3073-3086.
78. Wisse, E.; Jacobs, F.; Topal, B.; Frederik, P.; Geest, B. D., The size of endothelial fenestrae in human liver sinusoids: implications for hepatocyte-directed gene transfer. *Gene Therapy* **2008,** *15*, 1193-1199.
79. Chen, L.-T.; Weiss, L., The Role of the Sinus Wall in the Passage of Erythrocytes Through the Spleen. *Blood* **1973,** *41* (4), 529-537.
80. Ohlson, M.; Sörensson, J.; Haraldsson, B., A gel-membrane model of glomerular charge and size selectivity in series. *American Journal of Physiology - Renal Physiology* **2001,** *280* (3), F396-F405.

81. Decuzzi, P.; Godin, B.; Tanaka, T.; Lee, S.-Y.; Chiappini, C.; Liu, X.; Ferrari, M., Size and shape effects in the biodistribution of intravascularly injected particles. *Journal of Controlled Release* 2010, *141* (3), 320-327.
82. Christian, D. A.; Cai, S.; Garbuzenko, O. B.; Harada, T.; Zajac, A. L.; Minko, T.; Discher, D. E., Flexible Filaments for in vivo Imaging and Delivery: Persistent Circulation of Filomicelles Opens the Dosage Window for Sustained Tumor Shrinkage. *Molecular Pharmaceutics* 2009, *6* (5), 1343-1352.
83. Kaga, S.; Truong, N. P.; Esser, L.; Senyschyn, D.; Sanyal, A.; Sanyal, R.; Quinn, J. F.; Davis, T. P.; Kaminskas, L. M.; Whittaker, M. R., Influence of Size and Shape on the Biodistribution of Nanoparticles Prepared by Polymerization-Induced Self-Assembly. *Biomacromolecules* 2017, *18* (12), 3963-3970.
84. Müllner, M.; Dodds, S. J.; Nguyen, T.-H.; Senyschyn, D.; Porter, C. J. H.; Boyd, B. J.; Caruso, F., Size and Rigidity of Cylindrical Polymer Brushes Dictate Long Circulating Properties *In Vivo*. *ACS Nano* 2015, *9* (2), 1294-1304.
85. Black, K. C. L.; Wang, Y.; Luehmann, H. P.; Cai, X.; Xing, W.; Pang, B.; Zhao, Y.; Cutler, C. S.; Wang, L. V.; Liu, Y.; Xia, Y., Radioactive ^{198}Au-Doped Nanostructures with Different Shapes for *In Vivo* Analyses of Their Biodistribution, Tumor Uptake, and Intratumoral Distribution. *ACS Nano* 2014, *8* (5), 4385-4394.

CHAPTER II

The Impact of Lipoprotein Receptors and Lipid Metabolism on Nanomedicine

2.1 Abstract

Nanoparticles introduced into the bloodstream are exposed to thousands of proteins that are competing for their surfaces. During transport, this competition changes the amount and class of proteins that are bound to the nanoparticle surface. High density lipoproteins (HDLs) have been shown to bind nanoparticle surfaces of different sizes and chemistries, but quantitative values are lacking. Bound HDLs could change the biodistribution of nanoparticles if the interaction is stable and HDLs retain their functionality.

We determined equilibrium binding parameters for HDLs and nanoparticles using isothermal titration calorimetry, gel electrophoresis and a quantitative model of protein-sphere interactions. We used polystyrene spheres – PS, PS-COOH, and PS-NH_2 – as model nanoparticles. Apolipoprotein A-I – the main structural protein of HDLs – was shown to bind nanoparticles with moderate binding affinities in spite of competition from other plasma proteins. Isothermal titration calorimetry and exploration of the secondary structure of lipoproteins indicated that conformational states of lipoproteins could play a role in determining their strength of binding.

Our *in vivo* investigations with SCARBI-/- mice demonstrated the involvement of lipoprotein bound nanoparticles and lipoprotein receptors in nanoparticle biodistribution. We also determined from measurements of plasma HDL and LDL/VLDL cholesterol content that cholesterol metabolism was important to the uptake and biodistribution of injected polystyrene nanoparticles. In addition, we found that female and male mice have differences in relation to lipid metabolism which translated into different biodistribution profiles. Overall, this shows that lipid and lipoprotein metabolism are indeed important in nanoparticle drug delivery and this would have significant impact on the application of nanotherapies for various diseases.

2.2 Introduction

Over the last decades, nanotechnology-based therapeutics have been used for the treatment of various diseases, however, biological barriers have precluded the effectiveness of such drug delivery systems with poor drug biodistribution or accumulation at diseased sites being one of the major challenges.[1-4] Nanoparticle-based drug delivery systems that are administered intravenously to a patient enter the bloodstream and encounter blood proteins and biomolecules that vie for a position on the surface of the nanoparticles. Surface coverage and the composition of the adsorbed entities is determined by their respective affinities for the nanoparticle.[5-6]

Many research studies have revealed that lipoproteins constitute a major component of the biomolecular corona mass surrounding different nanoparticles exposed to blood or plasma proteins.[7-13] In particular, high-density lipoproteins (HDLs) or its major associated apolipoproteins have been demonstrated to bind nanoparticles *in vitro* with high affinity. For instance, apolipoproteinA-I (ApoA-I) – the main structural protein of HDLs – has been shown to bind polystyrene nanoparticles, PS (24 nm) and PS-COOH (28 nm), with affinity (K_d) values of 360 nM and 60 nM respectively.[14] Hydroxyethyl starch (HES) nanocapsules possessing different functionalities were shown to bind ApoA-I with K_d values of ~3 nM, ~5.3 nM, and ~185 nM for HES (275 ± 28 nm), HES-COOH (200 ± 20 nm), and HES-NH_2 (256 ± 26 nm) respectively.[15] Reconstituted HDL particles have also displayed high binding affinities to 70 nm N-iso-propylacrylamide/N-tert-butylacrylamide copolymer nanoparticles with a K_d value of 1 nM.[16] Notwithstanding, quantitative values are still lacking for studies that measure the binding affinity of HDLs, or its main structural proteins, for nanoparticles that are exposed to whole plasma. In order to achieve this aim, we investigated the binding of lipoproteins in mouse plasma to polystyrene nanoparticles of different surface

chemistries. We show that binding of lipoproteins to these nanoparticles was still fairly strong (K_d in micromolar range) despite competition from numerous proteins or biomolecules usually present in plasma.

Taking into consideration the binding of lipoproteins to nanoparticles, it is conceivable that lipoproteins could potentially change the course of injected nanoparticles to lipoprotein receptors (e.g. scavenger receptor class B I) in the body. Because lipoprotein receptors can be found widely distributed throughout tissues or major organs of the body (liver, lung, spleen, heart and kidney),[17] this could have significant consequences for nanoparticle drug delivery applications since delivery to potential targets would dwindle. Toxicity also becomes a major concern. Relevant *in vivo* models are thus needed to examine the distribution of nanoparticles in the body following binding to plasma lipoproteins in circulation. We address this issue by employing scavenger receptor class B I (SCARBI) mouse models that alter lipoprotein uptake, and clodronate liposomal formulations for macrophage depletion. Our findings demonstrate that nanoparticle distribution is indeed affected by lipoprotein receptor binding; and interestingly, there were differences in nanoparticle uptake and biodistribution between male and female genders of which lipid metabolism was implicated in the understanding of the overall observed differences.

2.3 Materials and Methods

2.3.1 Materials

50 nm PS (08691-10) and PS-COOH (15913-10) nanoparticles were purchased from Polysciences, Inc., United States and used as received. 50 nm PS-NH_2 were purchased from Bangs Laboratories, United States and used as received. 10X phosphate buffered saline powder concentrate (BP665-1), bovine serum albumin (BSA) fraction V (BP-1605-100), Coomassie brilliant blue R-250 (BP101-25), Tris-HCl (BP-153-300), glycerol (BP229-1), sodium chloride (BP358-1) and EDTA (S311) were all purchased from Fisher Scientific, United States. β-mercaptoethanol

(M3148) was purchased from Sigma-Aldrich, United States. Sodium dodecyl sulfate (SDS) sample buffer was formulated (250 mM Tris-HCl pH 6.8, 10% SDS, 30% Glycerol, 5% β-mercaptoethanol, 0.02% bromophenol blue). Precast protein gels (10-well NuPAGE 12% Bis-Tris and 15-well NuPAGE 4-12% Bis-Tris), 20X NuPAGE MOPS SDS running buffer and 1,1'-Dioctadecyl-3,3,3',3'-Tetramethylindotricarbocyanine Iodide (DiR) dye were purchased from Thermo Fisher Scientific, United States.

Mouse plasma (GTX73236) was purchased from Genetex, Inc., United States and human HDLs (361-10) were purchased from Lee Biosolutions, Inc., United States. Thyroglobulin, ovalbumin, carbonic anhydrase, ribonuclease, aprotinin, dextran 2000 were all purchased from GE Healthcare, United States. MP Biomedicals gamma globulin from bovine plasma and BD Vacutainer plasma separation tubes (PST) coated with lithium heparin were purchased from Fisher Scientific, United States. PageRuler Plus Prestained 10-250kDa Protein Ladder was purchased from Thermo Fisher Scientific, United States.

2.3.2 In Vitro Binding of Plasma Proteins to Polystyrene Nanoparticles

Mouse plasma was thawed in a water bath maintained at 37°C and centrifuged at 3,000 rpm for 5 min at 4°C (Sorvall Legend XTR Centrifuge, Thermo Fisher Scientific, Germany). The supernatant was collected, transferred to new tubes and re-spun at 13,300 rpm (17,000 xg) for 3 min at 4°C (accu Spin Micro 17, Fisher Scientific, Germany). Concentrations of polystyrene nanoparticles (5.85×10^{12} particles/ml, calculated based on manufacturer's specifications) were chosen such that there were no appreciable depletion effects from ApoA-I binding to the nanoparticles. Different mouse plasma dilutions were made and incubated with the polystyrene nanoparticles at 4°C for 2 hours on an orbital shaker (Orbitron Rotator II, Boekel Scientific, United States). Respective control samples were also incubated concurrently under the same conditions, and all dilutions for

mouse plasma were done with 1X PBS. After incubation, the samples were centrifuged (Beckman Optima LE-80K Ultracentrifuge, Beckman Coulter Inc., United States) at 4°C and at a speed of 40,000 rpm (Type 80 Ti rotor, 150,528 xg_{max}) for 20 min to separate unbound proteins from the nanoparticles. The solid nanoparticle-protein pellet was washed with 1X PBS and resuspended in SDS buffer. After addition of SDS sample buffer to the samples containing the nanoparticle-protein pellet and also the supernatant containing unbound proteins, they were incubated at 95°C for 10 mins. Following protein desorption and denaturation, the samples were then loaded onto a protein gel and run in 1X MOPS running buffer at 200 V for 50 min. For each gel, diluted mouse plasma at 1/20 X was used as an in-gel standard. The 1/20 X mouse plasma was calibrated for both 10-well and 15-well gels by using several known concentrations of BSA (Appendix A.2). Relative density values from the known albumin protein bands and all other protein bands were estimated using ImageJ software (http://rsbweb.nih.gov/ij) after staining with Coomassie blue. All of the gels were set up to include controls for both the supernatant and the nanoparticle-protein pellet samples, and dilutions from the sample buffer was accounted for when calculating the amount of proteins from needed sample bands. These *in vitro* experiments were carried out in triplicates.

The above procedure was applied to another experiment, but incubations were carried out with constant mouse plasma or human HDL (hHDL) concentrations and increasing nanoparticle concentrations. These experiments were carried out once.

2.3.3 HDL Isolation by Anion Exchange Chromatography

Two or three milliliters of mouse plasma was passed through a sterile polyethersulfone 0.22 µm filter (Millex-GP, Millipore) and introduced into a 50 ml Superloop (GE Healthcare, United States) column on an ÄKTApurifier 10 FPLC system maintained at 4°C. The mouse plasma was allowed to equilibrate in the starting buffer (1 mM EDTA,

20 mM Tris-HCl; pH 8.6) and then injected via the Superloop into an anion exchange column (Source 15Q, GE Healthcare, United States). The sample was processed at a flow rate of 1.2 ml/min and eluted (1 mM EDTA, 500 mM NaCl and 20 mM Tris-HCl; pH 8.4) as 1 ml fractions on a Frac-920 (GE Healthcare, United States) fraction collector modified to include 1.5 ml microcentrifuge tubes. Peaked fractions were run on a protein gel to determine purity and where to collect fractions containing HDLs. Subsequently, HDL peaked fractions were pooled and dialyzed against 1X PBS at 4°C.

2.3.4 Protein Identification by Mass Spectrometry

Bands of interest that were excised from SDS-PAGE gels and in-gel digestion was performed with trypsin according to a protocol by Shevchenko and coworkers.[18] The resulting peptide mixtures were separated with an UltiMate 3000 RSLCnano system (Thermo Fisher Scientific, United States) via precolumn concentration and an EASY-spray ionization source (Thermo Fisher Scientific, United States). 10 µl of the sample was loaded on the a PepMap C18 (Thermo Fisher Scientific, United States) precolumn using 98:2 (v/v) water: acetonitrile. This solvent was also used to desalt the sample for 10 min following the start of the run. After 10 min, the precolumn was back flushed with 100% water with 0.1% formic acid. The separation used an EASY-spray column (ES800, Thermo Fisher Scientific, United States) over the course of 60 min. Chromatography solutions (solvent A: 100% water with 0.1% formic acid; solvent B:100% acetonitrile with 0.1% formic acid) were used to deliver the 60 min gradient. The gradient is as follows: t = 0 min 100% A, 0% B; t = 10 min 100% A, 0% B; t = 35 min 5% A, 95% B; t = 45 min 5% A, 95% B; t = 45.1 min 100% A, 0% B; t = 60 min 100% A, 0% B. The column was kept at 40 °C.

A Thermo Scientific Q Exactive Orbitrap mass spectrometer was used to collect data. Data was collected in positive mode with the following ionization conditions: spray voltage 1.50 kV; capillary temperature 300°C. A full scan/data

dependent Top N analysis was performed to collected full scan data and fragmentation data of the most abundant *m/z* eluting the column. Mass spectrometer settings for the full scan were: resolution 70,000; automatic gain control $3x10^6$ ions; max IT time 100 ms; *m/z* range 200-2000. Mass spectrometer settings for the data dependent acquisition were: resolution 17,500; automatic gain control $1x10^5$ ions; max IT time 50 ms; loop count 12; isolation window 1 *m/z;* normalized collisional energy 30; dynamic exclusion 10.0 s.

Following data collection, the MaxQuant software was used to match detected parent masses and fragments to an in silico digested FASTA proteome with an error window of 5 ppm.

2.3.5 Gel Filtration Chromatography

hHDL and pooled fractions of mouse HDL (mHDL) from anion exchange chromatography were applied to a gel filtration column to estimate their molecular weights. A Superose 12 10/300 GL (GE Healthcare, United States) size exclusion column on an ÄKTA FPLC system was utilized. The column was equilibrated (50 mM phosphate, 0.15 M NaCl, pH 7.2) and then calibrated using the following molecular mass markers: thyroglobulin (670 kDa), gamma globulin (150 kDa), ovalbumin (44 kDa), ribonuclease (13.7 kDa), carbonic anhydrase (29 kDa) and aprotinin (6.5 kDa). Blue dextran 2000 was used to determine the column void volume. The gel phase distribution coefficient (K_{av}) value was calculated as: (elution volume – column void volume) / (geometric column volume – column void volume). A calibration curve of K_{av} versus logarithm of the molecular weight (log M_r) was plotted to calculate the molecular weights of hHDL and mHDL.

2.3.6 Isothermal Titration Calorimetry (ITC)

Experiments were carried out with a VP-ITC microcalorimeter (TA instruments, United States) at a temperature of 25°C and stirring rate of 300 rpm. Ultrapure Milli-Q water was used as a reference solution for the titrations. In order to minimize pH change during experiments, the studies were performed at neutral pH in aqueous solution. Lipoproteins (mHDL and hHDL) and polystyrene nanoparticles (PS, PS-COOH, PS-NH_2) were dialyzed against Milli-Q water, and experiments consisted of consecutive additions of lipoprotein solutions (1.92 mg/ml) from the syringe into nanoparticle solution (~1.2 x 10^{-5} mM) located in the cell of volume 1.451 ml. Lipoprotein solutions were added as 10 ul injections and the resulting data of heat against molar ratio were analyzed with an independent binding site model[19] using Microcal Origin 7.0 software. The first 2 µl injection was discarded because of diffusion of HDL before the initiation of the experiment. Appendix A.1 contains details of the model.

2.3.7 Preparation of DiR-loaded PS-COOH Nanoparticles

PS-COOH with DiR was prepared by a modified solvent-diffusion method.[20] Briefly, a solution containing the concentrated DiR (2.5 mg/ml in methanol) was added into 600 µl of PS-COOH (25 mg/ml) nanoparticle suspension. The solution was mixed and incubated for 15 min followed by dialysis (12 – 14 K MWCO) in 1X PBS. The same procedure was used for all preparations of PS-COOH-DiR labeled nanoparticles and the concentration of DiR was determined by UV-VIS from a DiR calibration curve. Particle size distribution of the PS-COOH-DiR nanoparticles was determined with DLS to ensure that the size distribution after labeling was relatively similar (Appendix A.4).

2.3.8 In Vivo Studies

Animal experiments were conducted using institutionally approved protocols by the Institutional Animal Care and Use Committee (IACUC) at the University of Tennessee, Knoxville.

Mice that are wild-type and homozygous null for SCARBI^{tm1Kri} were bred from six female and three male mice that are heterozygous for SCARBI^{tm1Kri} (stock# 003379, JAX Laboratory, United States). The breeding pair consisted of two female mice for one male mouse in a cage. All animals had free access to drinking water and a low-fat diet (D12450B, Research Diets, Inc., United States), and their housing facility was maintained at room temperature with regular day and night cycles. In a typical experiment, mice were injected intravenously via the tail vein with 200 µl of either clodronate liposomes or control liposomes (Liposoma B.V., Netherlands). Female mice had an average weight of 20.56 g (± 1.52) while male mice had an average weight of 22.66 g (± 2.06) (Appendix A.10). After 24 hours, mice were injected with either 100 µl of 1X PBS, DiR dye in 1X PBS or PS-COOH-DiR dyed nanoparticles. Twenty-four hours later, blood samples were collected via cardiac puncture with the mice under isoflurane anesthesia. Blood samples were collected into lithium heparin coated PST and centrifuged to obtain mouse plasma. Separated plasma samples were stored on ice for the duration of an experiment before freezing at -80°C for longer-term storage. At the end of blood collection and plasma separation, mice organs were harvested, and fluorescent images were obtained using a Vivo Vision IVIS Lumina (Caliper Co., United States) imaging system.

2.3.9 PCR Screening for Mice Genotype

Mouse tail snips were performed, and genomic DNA extractions were carried out according to manufacturer's protocol using DirectAmp tissue genomic DNA amplification kit (Denville Scientific, United States). The following stock primers were used as recommended by JAX Laboratory for SCARBI^{tm1kr1}: oIMR7768 wild-type forward, 5'-

ATC TCA GCC TTA GGC CCT GT-3'; oIMR7769 common, 5'-TCA AAC CCT GTG ACA ACA GC-3'; and oIMR7770 mutant forward, 5'-ATA GAT TCG CCC TTG TGT CC-3'. Stock primers were diluted to 100 pmoles/µl and then a fresh primer mix was made by diluting all primers to 10 pmoles/µl. The recipe for PCR amplification consisted of 4 µl of DNA extract, 1 µl of primer mix, 10 µl of Hot-Start Taq mastermix (Denville Scientific, United States) and 5 µl of water. PCR was carried out with an Eppendorf Mastercycler X50a (Eppendorf, Germany) under the following cycling conditions: 94°C for 4 min, (94°C for 20 s, 65°C for 20 s (lower by 0.5°C every cycle), 68°C for 20 s) 10 cycles, (94°C for 20 s, 60°C for 20 s, 72°C for 20 s) 28 cycles, 72°C for 2 min and hold at 4°C. Following the run, the PCR products were run on a 2% agarose gel at 100 V for 30 min. PCR products that were wild-type, heterozygous and mutant would have the following band sizes: 262 bp; 140 bp and 262 bp; and 140 bp respectively (Appendix A.9). exACTGene 50 bp mini DNA ladder (Fisher Scientific, United States) was used as the size marker.

2.3.10 HDL and LDL/VLDL Cholesterol Quantification

HDL and LDL/VLDL cholesterol quantification of mouse plasma was performed using an HDL and LDL/VLDL cholesterol assay kit (Abcam, United Kingdom). Optical density measurements were carried out at 570 nm.

2.4 Results and Discussion

2.4.1 Measurement of Binding Parameters by Gel Electrophoresis

The law of mass action was used to determine the binding of ApoA-I to the different polystyrene nanoparticles. We employed a simplified binding model where a nanoparticle was considered to have identical independent binding sites such that the binding of a protein to the nanoparticle does not influence subsequent binding steps. For the

sake of simplicity, the final derivations shown here are given in its reduced form; the more complicated and exact step-by-step binding approach can be found elsewhere.[21]

$$[N] + [P] \rightleftharpoons [NP] \tag{2.1}$$

$$[N_T] = [NP] + [N] \tag{2.2}$$

$$[P_T] = [NP] + [P] \tag{2.3}$$

where [N] and [P] are the concentrations of free nanoparticle and protein respectively. $[N_T]$ and $[P_T]$ are the total concentrations of nanoparticle and protein respectively while [NP] is the nanoparticle-protein complex concentration

$$Rate\ of\ forward\ reaction = K_f \cdot [N][P] \tag{2.4}$$

$$Rate\ of\ reverse\ reaction = K_r \cdot [NP] \tag{2.5}$$

Equating Eqn. (2.4) with Eqn. (2.5) and finding the ratio of the forward (K_f) and reverse (K_r) rate constants gives the expression for the association (K_a) binding constant while the inverse produces the dissociation (K_d) binding constant,

$$K_a = \frac{[NP]}{[N][P]} \tag{2.4}$$

$$K_d = \frac{[N][P]}{[NP]} \tag{2.5}$$

If we consider the nanoparticle surface as having only one binding site, then the simple 1:1 binding from the interaction of protein with the binding site in Eqn. (2.1) will yield the concentration of bound protein [NP]. Equating Eqn. (2.2) with Eqn. (2.5) and solving for fraction bound $[NP]/[N_T]$ yields,

$$\frac{[NP]}{[N_T]} = \frac{[P]}{K_d + [P]} \tag{2.6}$$

We however make the assumption that the polystyrene nanoparticle surface consists of multiple independent non-interacting binding sites. Therefore, if multiple independent and identical sites are on the polystyrene nanoparticle then the total amount of binding sites becomes,

$$n[N_T] = [NP] + [N] \tag{2.7}$$

where n sites are on a nanoparticle and Eqn. (2.6) is re-expressed as,

$$\frac{[NP]}{n[N_T]} = \frac{[P]}{K_d + [P]} \rightarrow \frac{[NP]}{[N_T]} = \frac{n[P]}{K_d + [P]} \tag{2.8}$$

but now bound protein [NP] incorporates all of the partially saturated forms of the nanoparticle-protein complex,

$$[NP] = [NP_1] + [NP_2] + \cdots [NP_n] = \frac{[N_T][P]}{K_{d1} + [P]} + \frac{[N_T][P]}{K_{d2} + [P]} + \ldots + \frac{[N_T][P]}{K_{dn} + [P]} \tag{2.9}$$

where n different sites can be occupied by the protein with the respective binding constant

A plot of ApoA-I that is bound to the nanoparticles versus free ApoA-I yields a hyperbolic curve where the binding affinity (K_d) can be obtained at half fractional saturation (n/2). This approach can be taken given that there are no considerable depletion effects from the protein binding to the nanoparticles, that is, [P] is approximately [P_T] at all concentrations used for the experiments.[22] In order to check for this, the unbound ApoA-I in the test supernatant and the ApoA-I in control supernatant were compared. Our results from measuring the density of the ApoA-I protein bands in the supernatant show that our assumptions are valid (Appendix A.3-1(A) – A.3-3(A)) and further calculations were not needed to account for depletion effects. K_d and n were calculated by comparing the resulting data of fraction bound – determined from the protein bands of the ApoA-I in the nanoparticle-protein pellet – with the fraction bound calculated from inserting the various ApoA-I concentrations from the plasma

dilutions into the model binding curve (Eqn. (2.8)) and minimizing the sum of squares error. Results of the binding model predicted values and the experimental data are shown in Figure 2.1 – 2.3.

Our results show that ApoA-I still has significant binding affinity for the polystyrene nanoparticles even in the presence of other competing plasma proteins; $K_{d\text{-}PSCOOH}$ 1.1 μM, $K_{d\text{-}PSNH2}$ 1.9 μM and $K_{d\text{-}PS}$ 3.1 μM. In addition, the number of ApoA-I particles on nanoparticle surfaces was higher for the PS (n = 92) and PS-NH_2 (n = 100) nanoparticles when compared with the PS-COOH (n = 58) nanoparticles pointing to potential surface chemistry effects on protein adsorption. To further elucidate the differences in binding, nanoparticle concentrations were increased while keeping plasma and hHDL concentrations constant. It is evident from Figure 2.4 that the depletion of ApoA-I in mouse plasma is hindered as $PSNH_2$ nanoparticle concentrations are increased, but this effect is not noticeable for nanoparticles incubated with hHDL. It is possible that structural changes of ApoA-I and/or surface displacements by other proteins may have played a role in inhibiting ApoAI binding to PS-NH_2 nanoparticles in whole plasma.

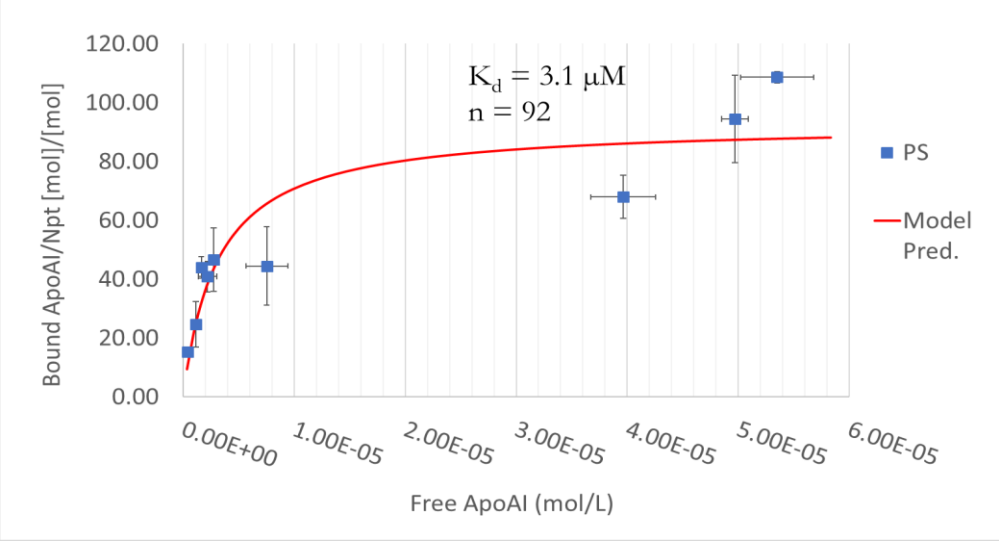


Figure 2.1 Saturation Binding Curve of ApoA-I to PS Nanoparticles

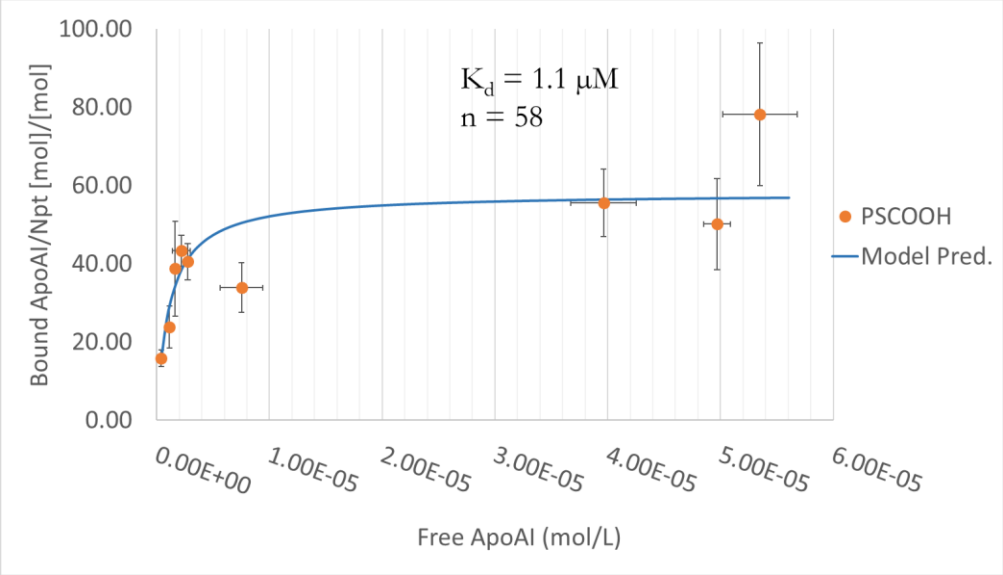


Figure 2.2 Saturation Binding Curve of ApoA-I to PS-COOH Nanoparticles

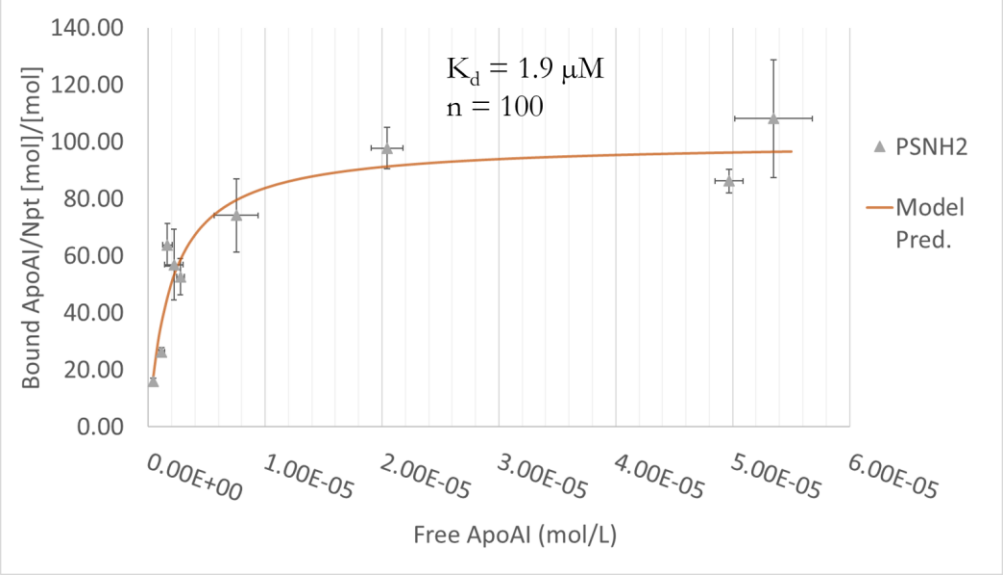


Figure 2.3 Saturation Binding Curve of ApoA-I to PS-NH_2 Nanoparticles

Researchers have demonstrated that PS-NH_2 nanoparticles disturb the secondary structure of ApoA-I upon binding and this becomes even more pronounced at higher nanoparticle concentrations.[14] Our investigations using circular dichroism (CD) confirmed their results after we incubated mHDL purified from whole plasma with PS-NH_2 nanoparticles (Appendix A.5). Another possibility for the observed differences in the depletion of ApoA-I in mouse plasma by PS-NH_2 nanoparticles could be because of the presence of nanoparticle-bound proteins in the supernatant. However, our studies using UV-VIS to examine the absorbance profile of both control and test samples after ultracentrifugation illustrate that this is clearly not the case (Appendix A.6) and that all particles are pelleted at the high g-forces. Restricted depletion of ApoA-I was therefore attributed to conformational changes of lipoproteins from binding to PS-NH_2 nanoparticles and the possible competition from other plasma proteins following the induced change.

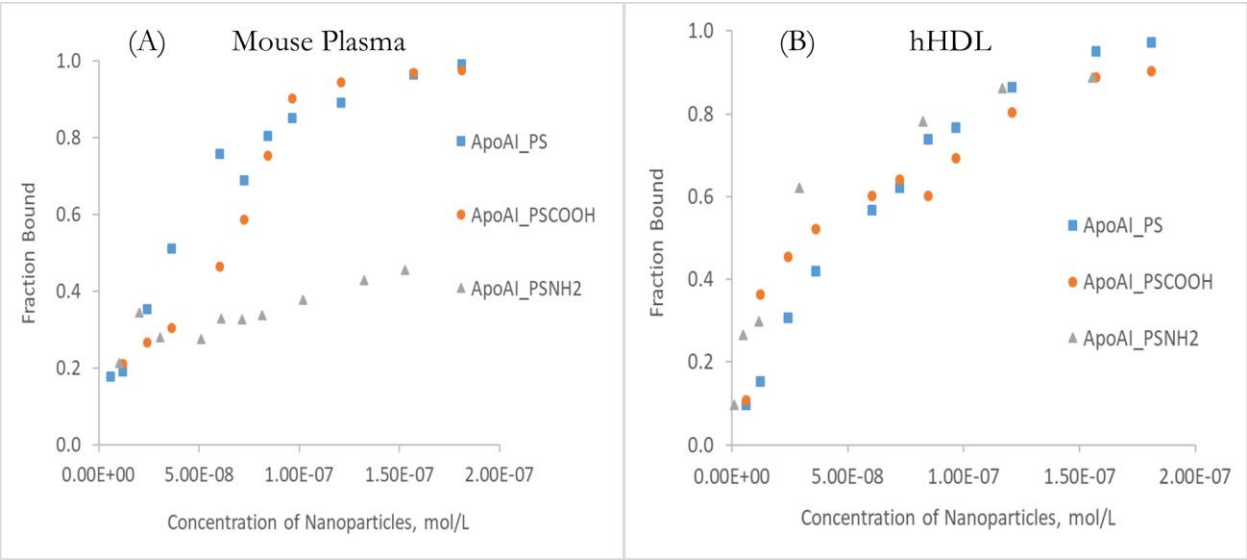


Figure 2.4 Fraction Bound of ApoAI from (A) Mouse Plasma and (B) hHDL on Polystyrene Nanoparticles

2.4.2 mHDL Purification by Anion Exchange Chromatography

In anion exchange chromatography, negatively charged molecules are attracted to the positively charged column (Source 15Q). This method utilized the characteristic that the relationship between the net surface charge experienced by a protein and the pH is unique to each individual protein. ApoA-I, the primary constituent of HDLs, should bind the positively charged column at the underlying pH of the buffer since it is greater than its isoelectric point (pI 5.3 – 5.8[23-24]). Bound proteins were eluted when salt ions of NaCl competed for a spot on the charged surface of the column. As we increased the salt concentration, it promoted the elution of one or more distinct proteins (Appendix A.7). Proteins having a lower net charge or weaker interaction were eluted first while those having a higher net charge or interaction with the column were eluted in later fractions. Albumin, a common contaminant found in the purification of HDLs from plasma was mainly eluted at earlier elution fraction (Appendix A.7) steps while HDL fractions were eluted at higher salt gradients since their ionic strength was greater at the prevailing pH. After the %elution buffer and fraction numbers were established, we considered reducing the %elution gradient at the fraction numbers coinciding with the elution of HDLs (Figure 2.5 – 2.6).

The initial salt gradient scheme employed 75% of elution buffer at the 85th fraction; this was changed to 70% but the gradient of %elution buffer remained the same, about 0.053% elution buffer for every 1 ml fraction. The change in the %elution buffer allowed us to obtain more fractions of HDLs (Figure 2.7); however, the salt gradient scheme could be optimized further for the acquisition of better resolved fractions. Figure 2.8 shows the HDL pooled fractions from the purification procedures. As a result of the attained protein gel profiles, we opted not to include fractions lower than 90 for future experiments with ITC.

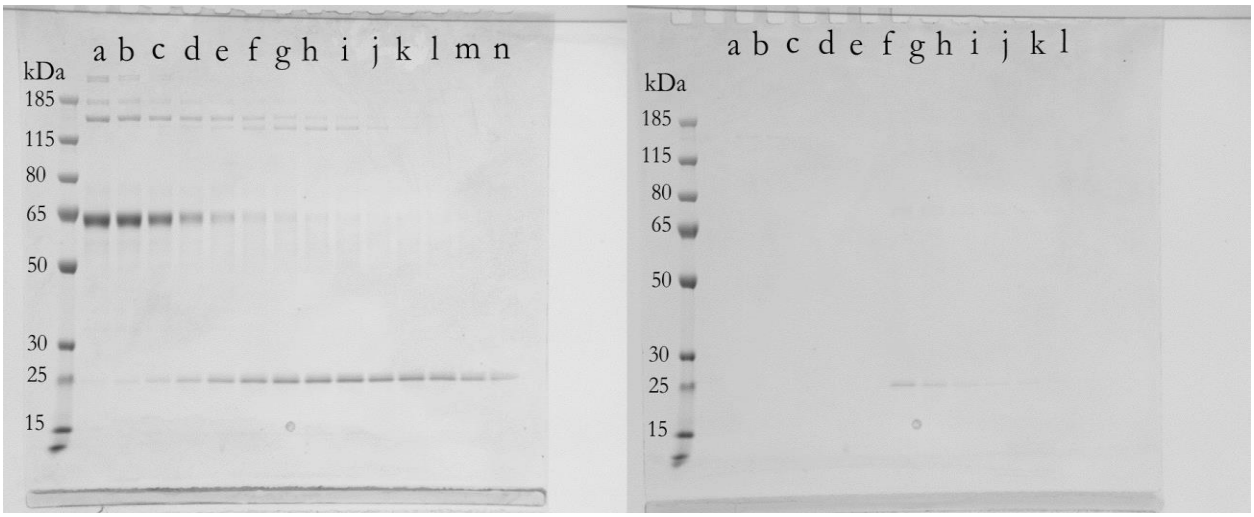


Figure 2.5 Elution of mHDLs and other Plasma Proteins at the Initial Salt Gradient Scheme. Left Panel: a-n, fraction 75 – 88; Right Panel: a-f, fraction 96 – 101; g-l, fraction 89-95.

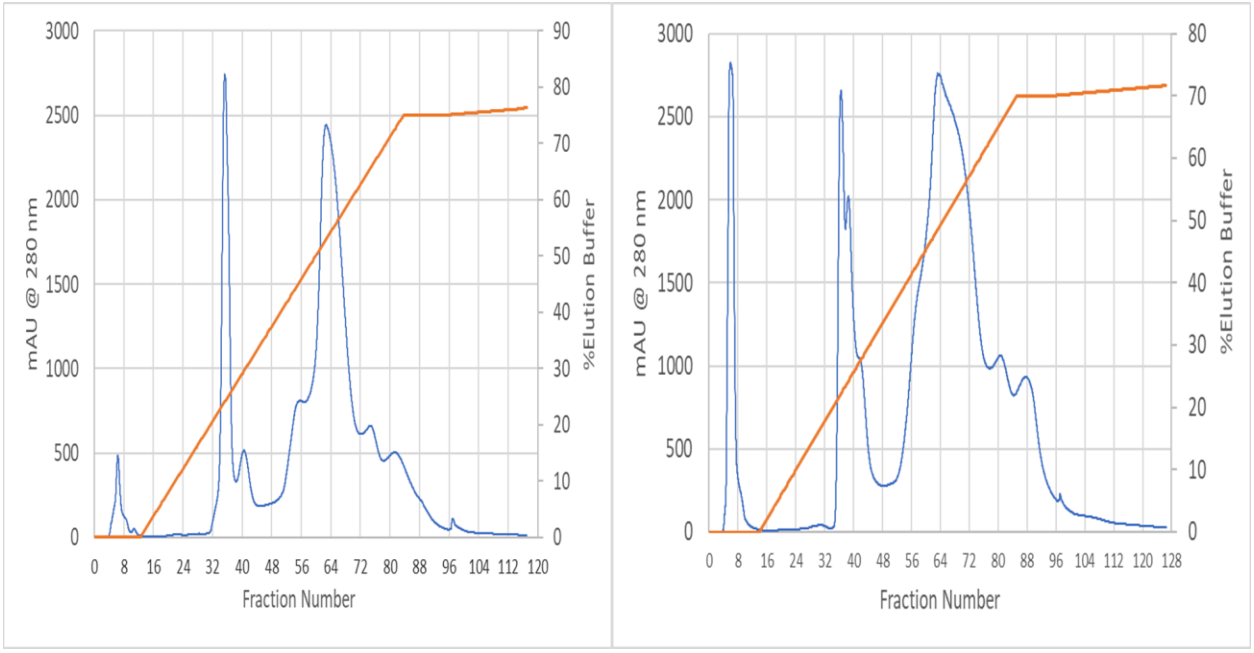


Figure 2.6 Chromatograms of the Purification of Lipoproteins from Mouse Plasma. Left Panel: Initial Salt Gradient Scheme. Right Panel: Final Salt Gradient Scheme. Linear gradient additions of elution buffer initiates after initial unbound plasma proteins are released from the column.

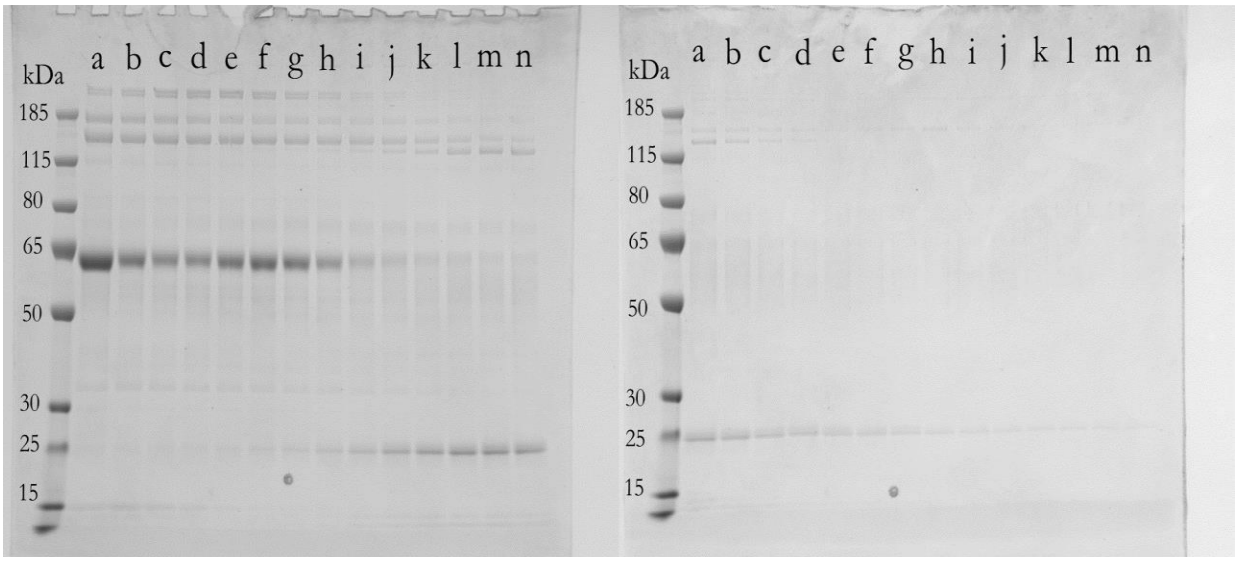


Figure 2.7 Elution of mHDLs and other Plasma Proteins from the Final Salt Gradient Scheme. Left Panel: a-n, fraction 76 – 89. Right Panel: a-n, 90 – 103

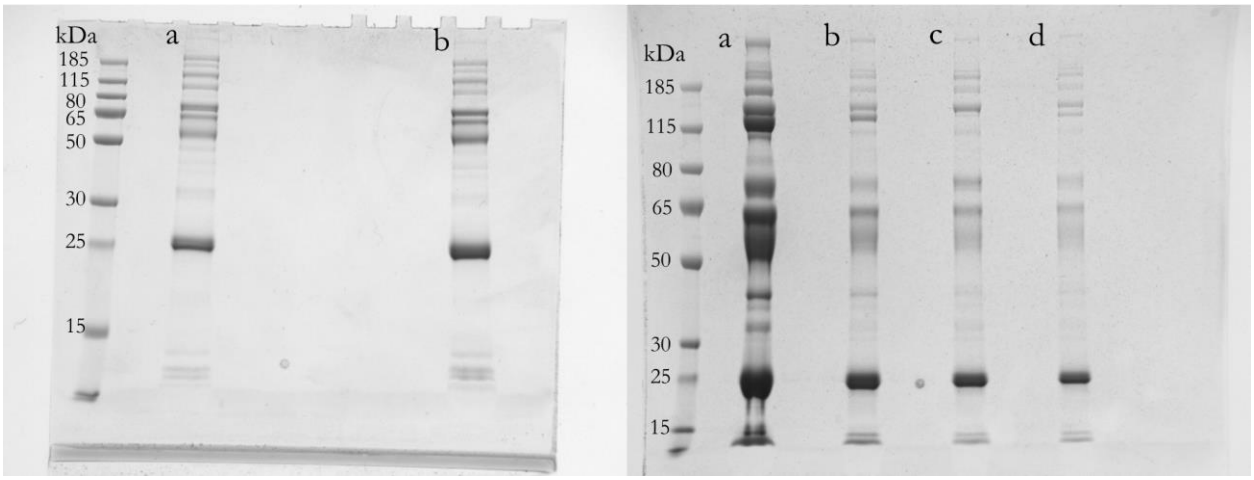


Figure 2.8 Peaked Pooled Fraction of mHDLs from Anion Exchange Chromatography. Left Panel: mHDL Profiles in a 10-well Gel from Using the Initial Salt Gradient Scheme; a- fraction 87 - 88 and 91 – 94; b- 87 - 90. Right Panel: mHDL Profiles in a 15-well Gel from Using the Final Salt Gradient Scheme; a, 88 – 89; b, 90 – 93; c, 94 – 103; d, 90 – 103.

2.4.3 Measurement of HDL Binding Parameters by ITC

ITC is a commonly used technique to study the adsorption and thermodynamic parameters from the binding of biomolecules and ligands in solution. Since the experiments are carried out *in situ*, it enables us to directly obtain binding parameters for nanoparticle-protein interactions in solution and also to determine associations that may be favorable. Titrations were analyzed for the twenty-seven 10 µl injections of HDLs into nanoparticle solution in the cell, and the generated adsorption isotherms and heat changes from titrations are shown in Figure 2.9 – 2.10. All binding isotherms were fitted according to an independent binding model (Appendix A.1).[19]

Examining the adsorption isotherms provides a quick way of gaining insight into the nature of binding between the HDLs and polystyrene nanoparticles. We can see from the steepness of the adsorption isotherms that the hHDLs have a higher binding affinity for PS and PS-COOH nanoparticles when compared with the mHDLs. However, it is difficult to make any inferences by visual inspection of the adsorption isotherms corresponding to PS-NH_2 and HDL titrations except that mHDLs have a higher affinity to PS-NH_2 than PS and PS-COOH. Table 2.1 provides a summary of the values obtained from fitting the data according to the independent site binding model. Stoichiometry and binding affinity values from protein gel electrophoresis measurements are also included for reference.

The results from the ITC experiment suggest that roughly 30 to 40 proteins constitute the corona proteins from the interaction of polystyrene nanoparticles with mHDLs. These values are in good agreement with the study performed with gel electrophoresis where the stoichiometry of binding of ApoA-I for PS, PS-COOH and PS-NH_2 nanoparticles are 92, 58 and 100 respectively. If HDLs are assumed to have around 3 – 4 ApoA-I molecules,[25] then this translates ideally to about less than equal to 31, 19 and 33 molecules of mHDLs on the PS, PS-COOH

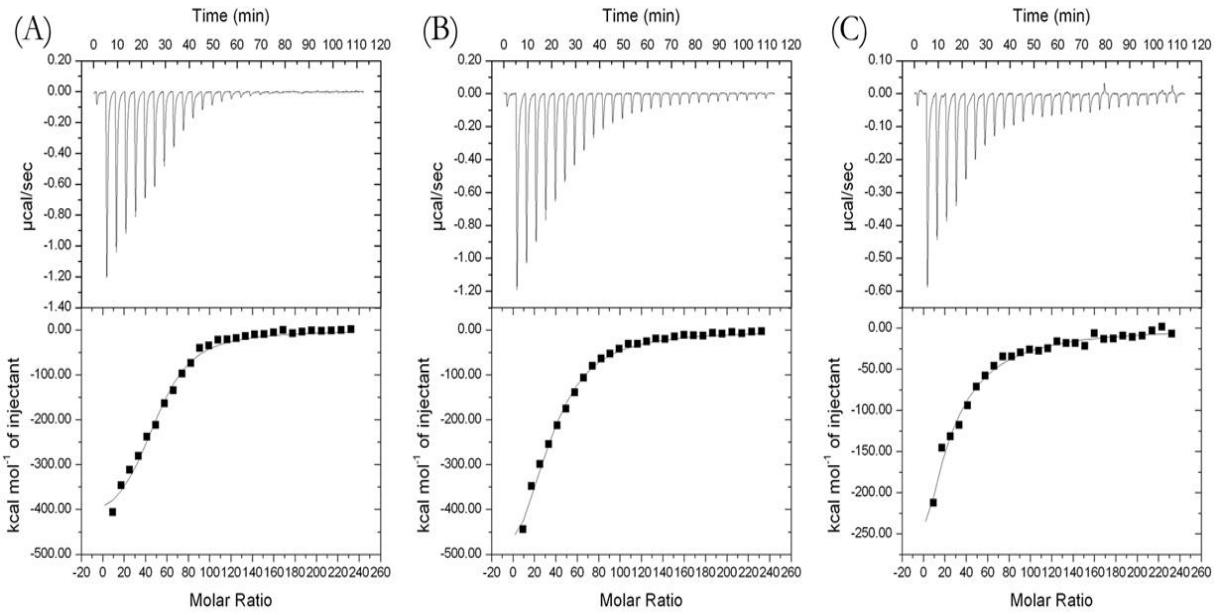


Figure 2.9 ITC Data from Titrating hHDL into Polystyrene Nanoparticles. (A) hHDL + PS. (B) hHDL + PS-COOH. (C) hHDL + PS-NH_2. The top panels represent the raw data from titrations after referenced baseline correction. The bottom panel are the integrated heats from each peak fitted to an independent binding model (solid lines).

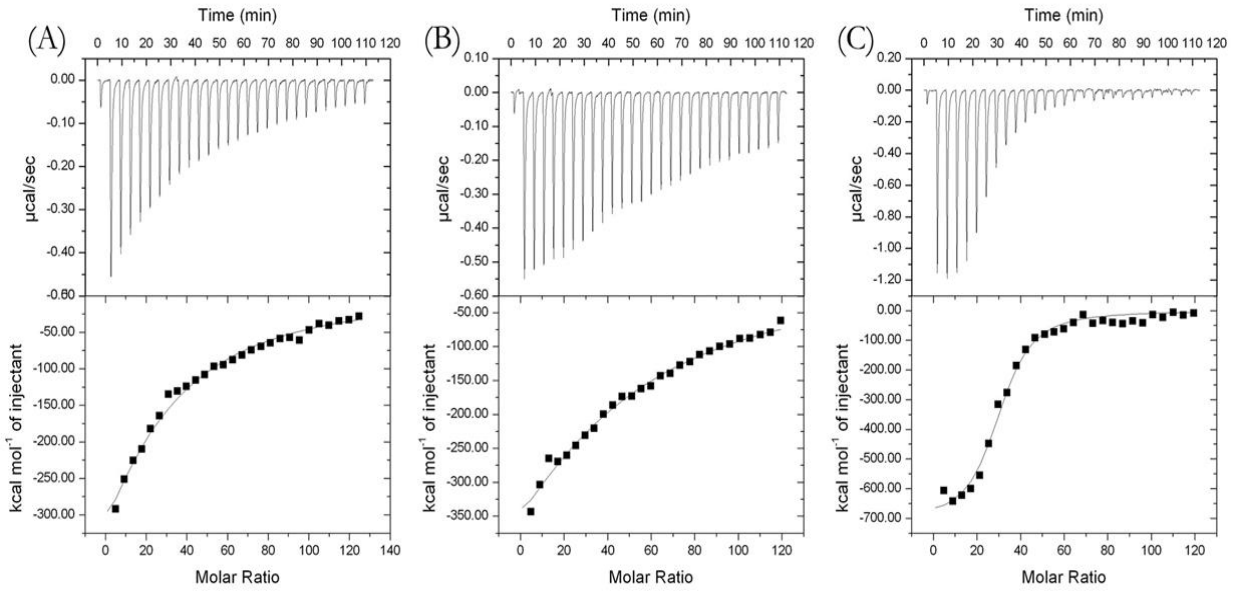


Figure 2.10 ITC Data from Titrating mHDL into Polystyrene Nanoparticles. (A) mHDL + PS. (B) mHDL + PS-COOH. (C) mHDL + PS-NH_2. The top panels represent the raw data from titrations after referenced baseline correction. The bottom panel are the integrated heats from each peak fitted to an independent binding model (solid lines).

Table 2.1 Adsorption Parameters Obtained from ITC and Protein Gel Electrophoresis

Protein	Nanoparticle	n	K_a (μM^{-1})	K_d (μM)	ΔH (kcal/mol)	ΔS (cal/mol K)
mHDL	PS	30 ± 4.99	2.50 ± 0.511	0.4	-596.2 ± 12.51	-1970
	PS-COOH	36.5 ± 8.91	1.11 ± 0.227	0.9	-1036 ± 318.2	-3450
	PS-NH_2	30 ± 0.678	39.5 ± 6.65	0.025	-711.3 ± 21.53	-2350
hHDL	PS	49 ± 1.44	11.1 ± 1.57	0.09	-450.8 ± 17.61	-1480
	PS-COOH	34.2 ± 1.72	5.44 ± 0.596	0.184	-666.1 ± 42.06	-2200
	PS-NH_2	37 ± 15.2	4.60 ± 0.873	0.217	-295.6 ± 13.26	-962
ApoA-I	PS	92	0.32	3.1	-	-
from	PS-COOH	58	0.91	1.1	-	-
mPlsm*	PS-NH_2	100	0.53	1.9	-	-

*ApoA-I from whole mouse plasma. Experiments were carried out at 4 Celsius

and PS-NH_2 nanoparticles respectively. It should be remembered that the experimental conditions for both systems are different, and that could account for the differences observed in the binding of lipoproteins to the nanoparticles.

Stoichiometry values for hHDLs are slightly dissimilar from mHDLs and this is expected since the molar mass and HDL species are different. The molar mass as estimated by gel filtration chromatography was 140.8 kDa and 276.5 kDa for hHDLs and mHDLs respectively (Appendix A.8). It is expected that a higher molecular weight (MW) protein occupy less area on a nanoparticle surface given its size and the available area for binding. Binding affinities for the hHDL group revealed that the K_d values for PS-COOH and PS-NH_2 were comparable and that the highest affinity was for PS. However, mHDLs displayed a different trend with mHDLs binding to PS-NH_2 possessing the highest affinity (PS-COOH < PS < PS-NH_2).

Conformational changes of the mHDLs may have played a role in the high values observed for binding to PS-NH_2. Recently, Müller and coworkers employed ITC to study the binding of lipoproteins to PS nanoparticles and from results of their investigations they indicated that lipoproteins that first come into contact with PS

nanoparticles disintegrate and promote the complete saturation of the nanoparticle surface by lipids before additional lipoproteins bind to form the biomolecular corona.[26] Therefore, it is seems probable that conformational changes in the mHDLs could have fostered the increased binding affinity for PS-NH_2. Our CD data (Appendix A.5) and those of other researchers[14] showing the loss in secondary structure of lipoproteins upon interaction with $PSNH_2$ nanoparticles lend credence to this point, suggesting that this could be the case. It is possible that specific conformational states allow for the undocking of the lipid component of HDLs which facilitates disintegration, lipid binding to the nanoparticles and ultimately the binding of lipoprotein complexes.

It should be noted, however, that a higher conformational change does not necessitate tighter binding, as has been recognized in other studies.[27-28] In our study, hHDLs binding to PS-NH_2 had the lowest binding affinity but its entropy was highest for all three nanoparticle types while hHDLs binding to PS had the highest binding affinity, but its entropy was lower. Research by Kono and coworkers suggest that ApoA-I could have different conformations (open or closed conformation anchored by the C-terminal domain) at the surface of a lipid particle depending on the ApoA-I concentration and cholesterol content on the particle.[29] From their investigations, they proposed a mechanism whereby high cholesterol content (and low ApoA-I surface concentration) on the lipid particle promotes an open conformation while low cholesterol content (and high ApoA-I surface concentration) promotes the closed conformational state. Consequently, it appears plausible that there is an interplay between specific conformational states on lipoprotein molecules that enhances lipid release and binding to nanoparticles.

2.4.4 Effect of Lipoprotein Binding and SCARBI Receptors on Nanoparticle Biodistribution

With Sarah Kauffman, we bred mice homozygous null for SCARBI. Mice were genotyped using PCR (Appendix A.9). Following intravenous injections with clodronate liposomes, it is expected that hepatic and splenic

macrophages be eliminated within 24 hours after administration of the recommended 0.01ml/g dose.[30-31] Macrophage depletion in the liver and spleen helped to decouple the effects of macrophage activity in these organs on nanoparticle uptake. We see from Figure 2.11 – 2.12 that after macrophage depletion, the uptake of PS-COOH nanoparticles in the livers of male SCARBI-/- mice was significantly reduced. Interestingly, there was no significant change in the spleen. The lungs were considerably affected by the injection of clodronate liposomes as is evident in the significantly reduced uptake in male SCARBI-/- mice. In the rest of the investigated organs, we do not see any significant changes in nanoparticle uptake after macrophage depletion. Male mice that were injected with control liposomes saw only a significantly reduced uptake in the spleen of SCARBI-/-. Injected dye seemed to follow similar trends in uptake for males injected with clodronate and control liposomes, with exceptions in the lungs and kidneys in the clodronate liposome group and white adipose tissue (WAT) in the control group.

In female mice, there appeared to be a reversal in the uptake of nanoparticles in the clodronate liposome-treated group. The liver, spleen, heart and kidneys all showed a significantly *increased* uptake of nanoparticles in SCARBI-/- mice (Figure 2.13 – 2.14). This is intriguing because it was initially assumed that lipoproteins would bind nanoparticles and deliver them to SCARBI receptors in various organs. One possible reason for this difference could be size of the organs. SCARBI-/- mice of both male and female genders have been shown to have a tendency of exhibiting splenomegaly;[32-33] therefore, the overall uptake per organ should be diminished and thus does not explain the significant differences observed in the spleen of female mice that were injected with clodronate liposomes. The splenomegaly effect in SCARBI-/- mice however brings up the question of organ size dissimilarities between SCARBI-/- and SCARB+/+ mice.

An inspection of the weights of the different organs (Figure 2.15 – 2.16) revealed that there were some significant differences in the spleen and WAT of the SCARBI-/- and SCARBI+/+ female pair for the control

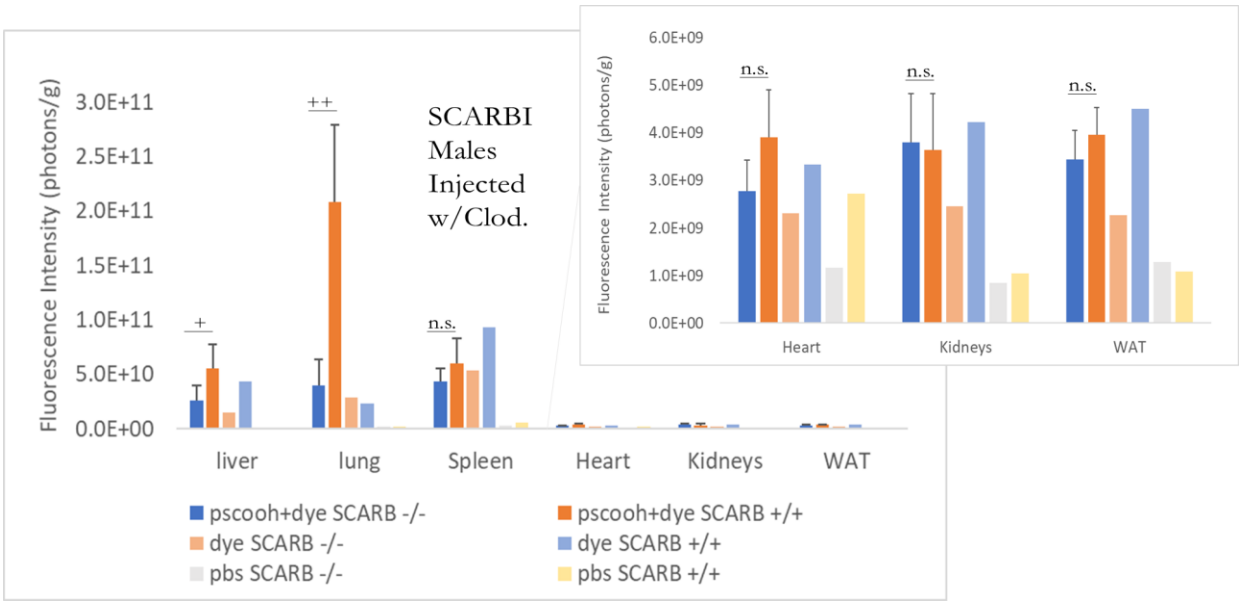


Figure 2.11 Fluorescence Intensity of Organs of Male SCARBI Ex Vivo After Macrophage Depletion with Clodronate Liposomes. PSCOOH+dye values are means ± SD (n = 5) except SCARB -/- (n = 3), dye (n = 1), pbs (n = 1). + $p < 0.05$, ++ $p < 0.01$ as determined by t-test (an F-test for equal and unequal variances was done and the corresponding t-test was applied).

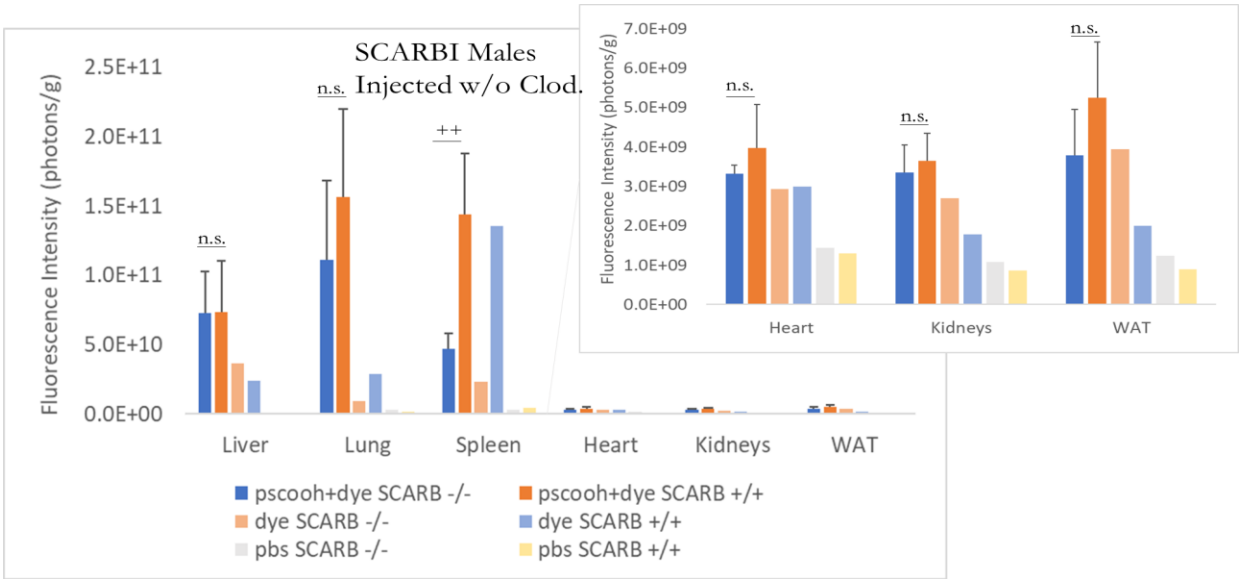


Figure 2.12 Fluorescence Intensity of Organs of Male SCARBI Ex Vivo After Injections with Control Liposomes. PSCOOH+dye values are means ± SD (n = 5), dye (n = 1), pbs (n = 1) except SCARB -/- (n =2). ++ $p < 0.01$ as determined by t-test (an F-test for equal and unequal variances was done and the corresponding t-test was applied).

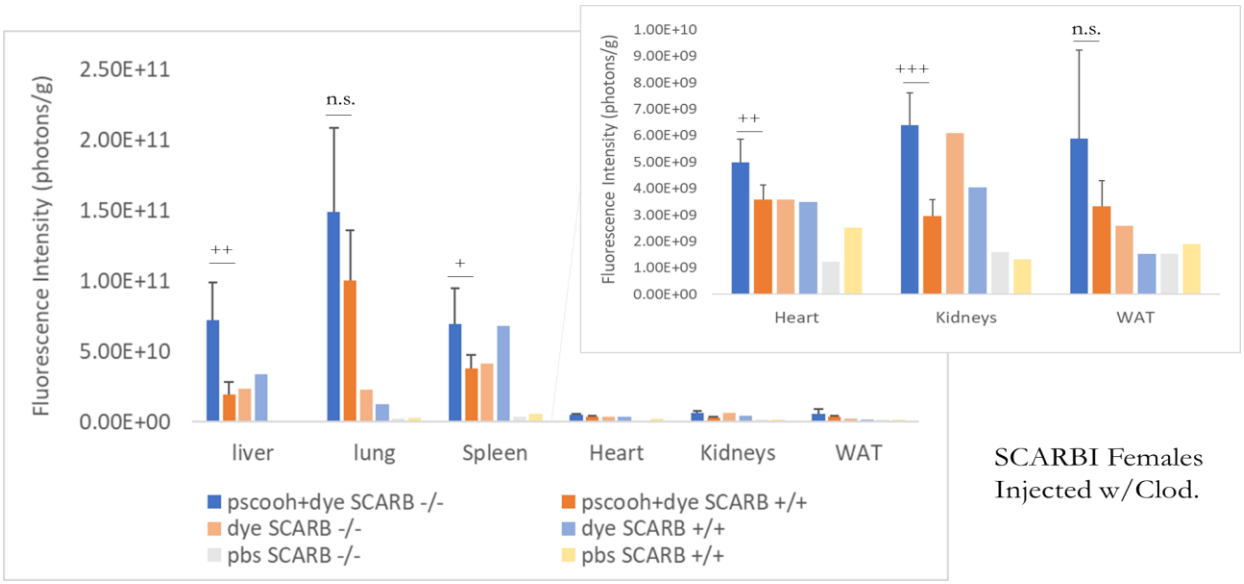


Figure 2.13 Fluorescence Intensity of Organs of Female SCARBI Ex Vivo After Macrophage Depletion with Clodronate Liposomes. PSCOOH+dye values are means ± SD (n = 5), dye (n = 1), pbs (n = 1). ++ $p < 0.01$, +++ $p < 0.001$ as determined by t-test (an F-test for equal and unequal variances was done and the corresponding t-test was applied)

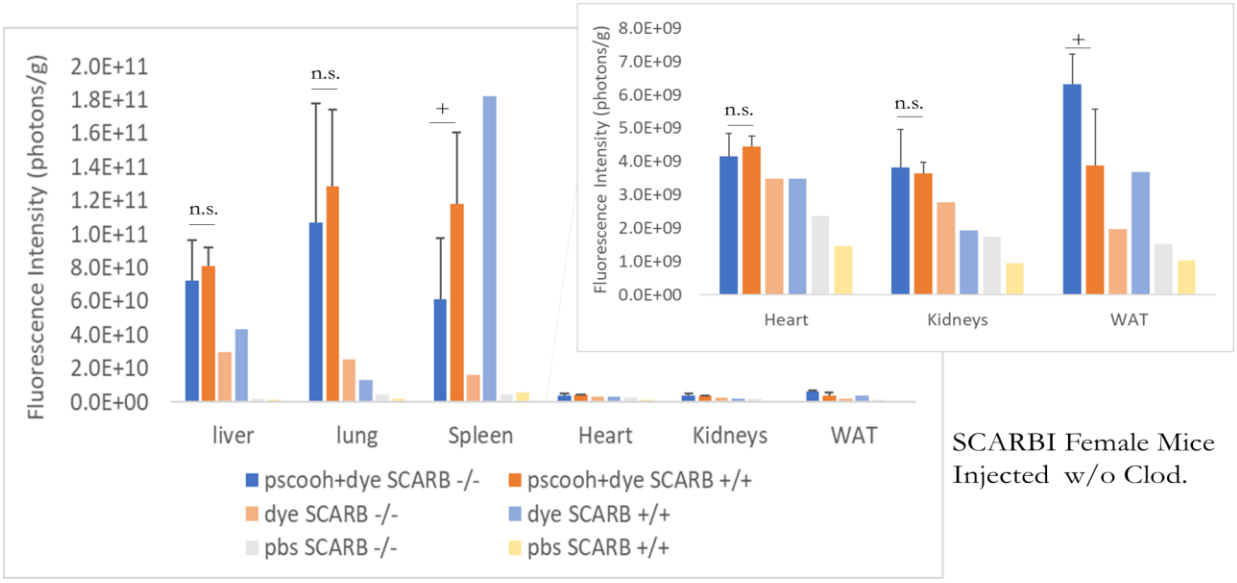


Figure 2.14 Fluorescence Intensity of Organs of Female SCARBI Ex Vivo After Injections with Control Liposomes. PSCOOH+dye values are means ± SD (n = 5), dye (n = 1), pbs (n = 1). + $p < 0.05$ as determined by t-test (an F-test for equal and unequal variances was done and the corresponding t-test was applied).

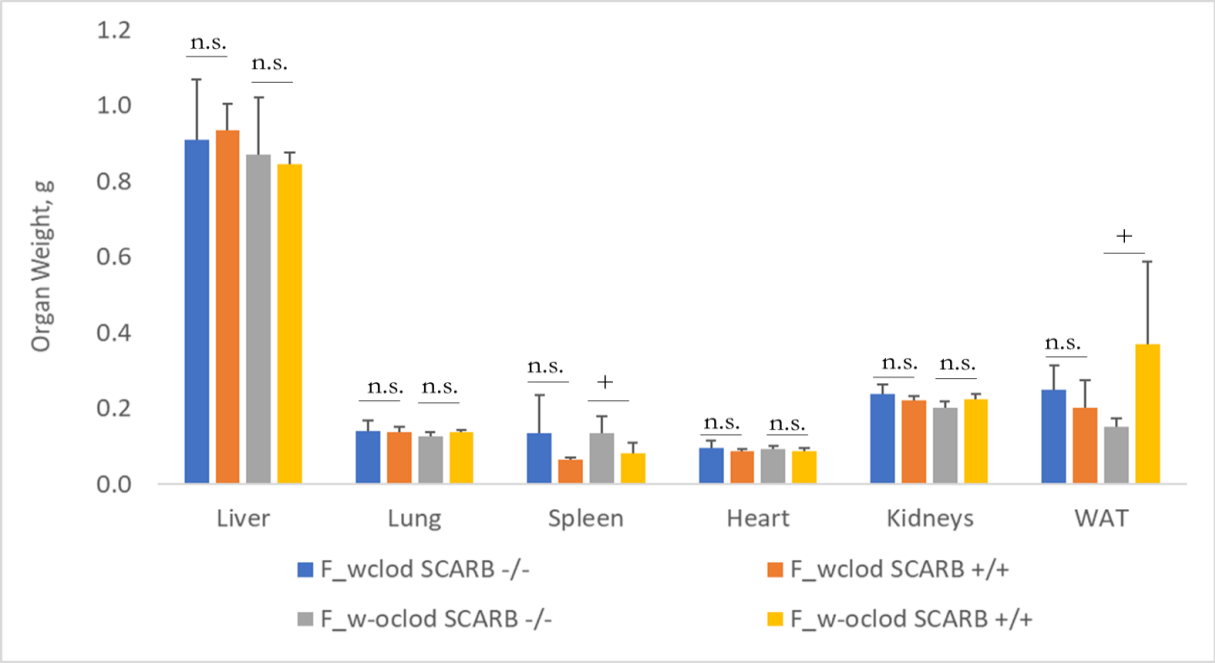


Figure 2.15 SCARBI Female Organ Weights. n = 5. + $p < 0.05$ as determined by t-test (an F-test for equal and unequal variances was done and the corresponding t-test was applied)

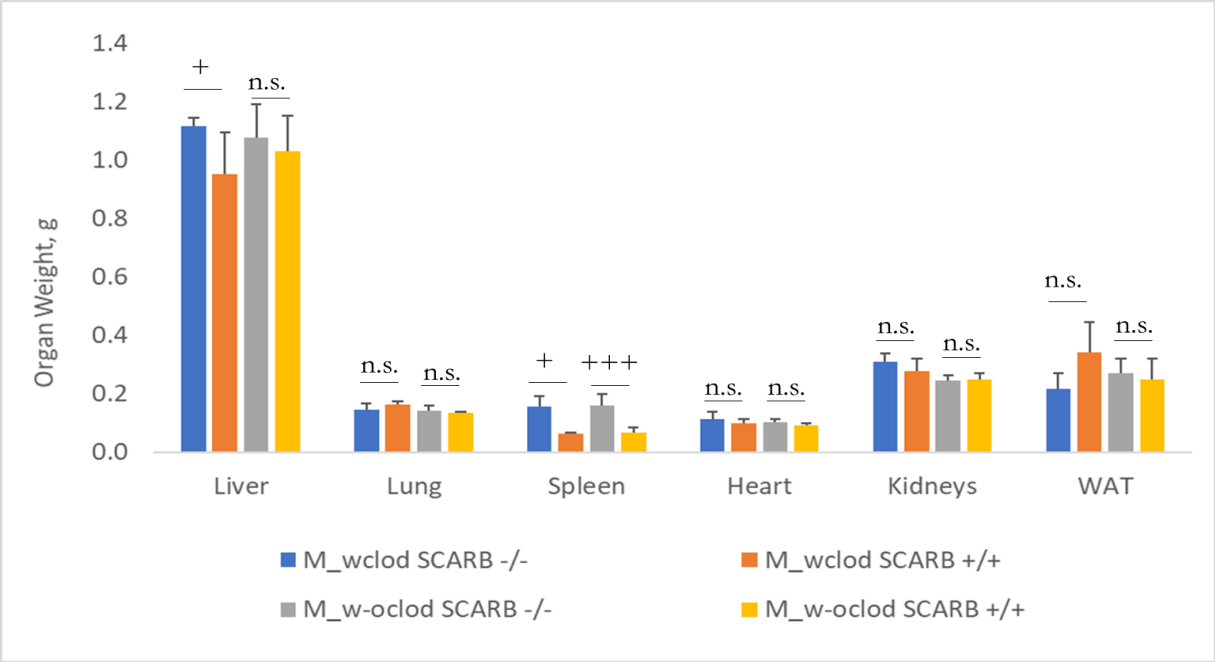


Figure 2.16 SCARBI Male Organ Weights. n = 5, but wclod SCARBI-/- n = 3. + $p < 0.05$, +++ $p < 0.001$ as determined by t-test (F-test for equal and unequal variances was done and the corresponding t-test was applied).

liposome group. Hence, the size of the spleen and WAT could possibly explain the decreased and increased uptake of nanoparticles respectively by female SCARBI-/- mice for the control liposome group. There were not any significant differences in all the other pairs for both the clodronate and control liposome group. Consequently, the increased nanoparticle uptake in the liver, spleen, heart and kidneys of the clodronate liposome-treated group of female mice was not influenced by organ size. No particular trends were observed within either the clodronate liposome-treated or control liposome group after the injection of dye. Nonetheless, we do see some trends in the biodistribution of the dye across the two groups with the exception of WAT; also pointing to the importance of SCARBI receptors in nanoparticle biodistribution.

For male mice, the differences in liver weights may potentially explain the decreased uptake; but it does not explain the drastically increased uptake by the lungs since there were no organ size differences. The SCARBI receptors were the likely cause for the increased uptake, and our results also suggests a different mode of macrophage depletion in the lungs by intravenously injected clodronate liposomes. Clodronate liposome mechanism of action is such that after macrophage engulfment and fusion with lysosome, the phospholipid bilayers of clodronate liposomes are broken down by lysosomal enzymes (phospholipases) which then releases the clodronate drug.[34] The clodronate drug by itself cannot cross the phospholipid bilayers of the liposomes so that more drug is released with an increase in the disruption of concentric phospholipid bilayers.[35] Since free clodronate cannot cross the phospholipid bilayer, it will not easily pass the phospholipid bilayers of cell membranes. Moreover, the half-life of free clodronate is extremely short (order of minutes) and will only spend a short time in circulation if released from dead macrophages.[36] Therefore, there has to be another mechanism by which clodronate liposomes deplete macrophages in the lungs since free clodronate are removed from circulation rapidly and it would not readily pass through the interstitial blood-gas barrier.

Koay and coworkers demonstrated that intravenous injection of 200 µl (5 mg/ml) clodronate liposomes in C57BL/6 mice depleted 66% of alveolar macrophages in the bronchial alveolar lavage fluid after 48 hours.[37] The exact mechanism for this depletion is unclear. Considering the depletion of bone marrow macrophages by clodronate liposomes,[38] perhaps, the recruitment of bone marrow macrophages enriches alveolar macrophages in lungs since macrophage populations in the lungs can arise from bone marrow-derived blood monocytes.[39-40] It may then be possible that a recruitment of pulmonary intravascular monocytes/macrophages (e.g. due to nanoparticle burden) are either indirectly or directly affected by bone marrow macrophage depletion in the SCARBI mice.[41]

Disparities in the mode of nanoparticle uptake between male and female mice may be a consequence of distinct lipid and lipoprotein metabolism in the two genders. Our findings from measurements of plasma HDL and LDL/VLDL cholesterol content in mice treated with clodronate liposomes and control liposomes suggests this phenomenon. Plasma HDL cholesterol content was lower in female SCARBI+/+ mice in the clodronate liposome-treated group while the opposite was observed for male SCARBI+/+ mice (Figure 2.17). This shows the potential for macrophage cholesterol homeostasis to be differentially affected in the different genders. The decrease in plasma HDL cholesterol displayed by female SCARBI+/+ mice could signify a more selective and involved SCARBI receptor-mediated control of cholesterol metabolism, while the increase in plasma HDL cholesterol seen in male SCARBI+/+ is not surprising since macrophages as a whole play a role in the regulation of cholesterol uptake. It is worth noting that the absence of the SCARBI receptor increased plasma LDL/VLDL cholesterol concentrations. This is predictable because SCARBI can function as a multiligand receptor for HDLs, LDLs and VLDLs.[42] Research by Huby and coworkers also found increased plasma cholesterol levels of VLDLs in SCARBI-/- mice that were fed

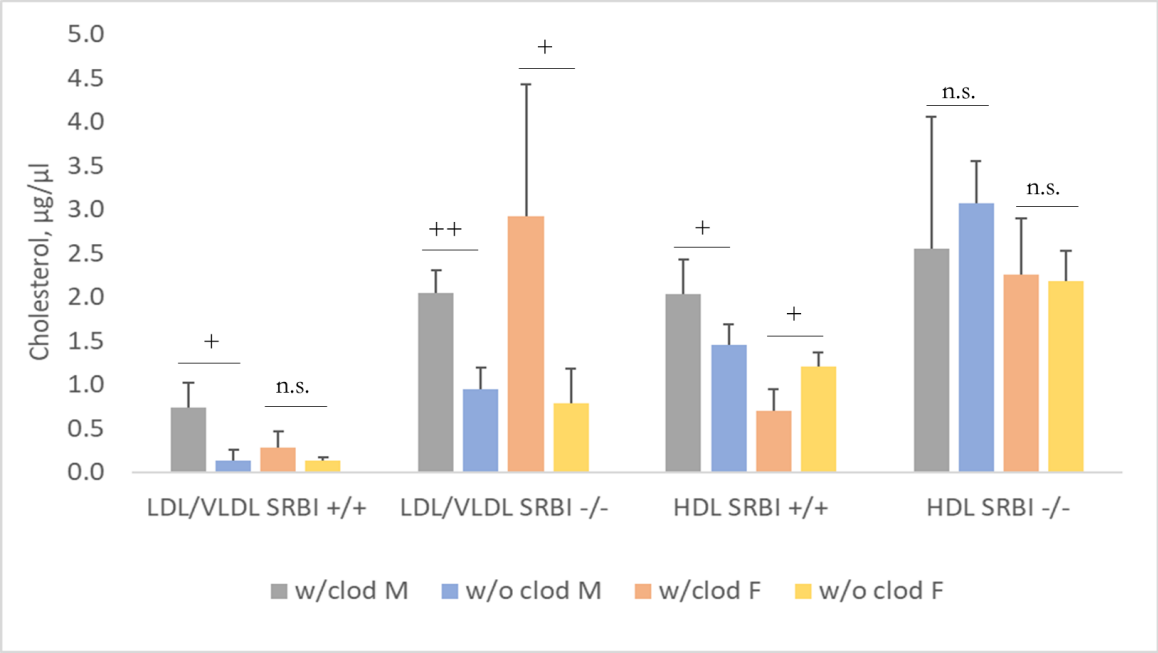


Figure 2.17 Plasma HDL and LDL/VLDL Concentration in Male and Female Mice Treated With Clodronate and Control Liposomes. For SCARBI+/+, n = 3 for all except females treated with clodronate liposomes n = 4. For SCARBI-/-, n = 3, 4, 4 and 5 for males treated with clodronate liposomes, control liposomes; and females with clodronate liposomes, control liposomes respectively. + $p < 0.05$ and ++ $p < 0.01$ as determined by t-test (an F-test for equal and unequal variances was done and the corresponding t-test was applied).

a high fat diet, and these VLDL particles were rich in apoE.[43] Rigotti and coworkers also found similar apoE-rich VLDLs in the plasma cholesterol of SCARBI-/- mice that were fed a regular diet.[44]

In the HDL SCARBI-/- group, it is unclear why no significant changes in plasma HDL cholesterol were detected in both female and male mice; it may be possible that the absence of macrophages and SCARBI receptors is compensated for by other SCARBI-independent pathways or the net flux of plasma HDL cholesterol from macrophage uptake and SCARBI-independent pathways. However, differences in plasma HDL cholesterol levels in SCARBI+/+ mice treated with clodronate liposomes does suggest different mechanisms for lipid and lipoprotein metabolism between male and female mice. A study by Brodeur and coworkers provide more validation for genetic differences in lipid and lipoprotein metabolism.[45] Their core findings showed that the selective uptake of LDL cholesteryl esters in the livers of male and female mice is carried out by both an SCARBI-dependent and independent pathway, with females displaying much higher SCARBI-independent activity. Others have also noted gender-related differences in cholesterol uptake[46-48] and drug metabolism,[49-50] and these would have significant implications in nanoparticle drug delivery.

2.5 Conclusion

Lipoproteins bind nanoparticles, but their affinity depends on the composition of the nanomaterial and the conformational state of lipoproteins during binding. The release of lipids from lipoproteins could also direct binding kinetics and the flux of lipoprotein complexes after lipoprotein fragmentation from contact with the nanoparticle surface. Due to the functions of lipoproteins in cholesterol metabolism, intravenously injected nanoparticles could bind lipoproteins and be diverted away from intended targets to lipoprotein receptors in the body. Gender differences could also affect nanoparticle drug delivery because of the selective uptake of cholesteryl

esters by scavenger receptors. Overall, lipoproteins and lipid metabolism have been shown to be important contributors to the biodistribution of nanoparticles. These findings should make us become more aware of the influence of metabolic status on nanomedicine.

References

1. Hare, J. I.; Lammers, T.; Ashford, M. B.; Puri, S.; Storm, G.; Barry, S. T., Challenges and strategies in anti-cancer nanomedicine development: An industry perspective. *Advanced Drug Delivery Reviews* **2017,** *108*, 25-38.
2. Etheridge, M. L.; Campbell, S. A.; Erdman, A. G.; Haynes, C. L.; Wolf, S. M.; McCullough, J., The big picture on nanomedicine: the state of investigational and approved nanomedicine products. *Nanomedicine: Nanotechnology, Biology and Medicine* **2013,** *9* (1), 1-14.
3. Duncan, R., Polymer conjugates as anticancer nanomedicines. *Nature Reviews Cancer* **2006,** *6* (9), 668-701.
4. Dawidczyk, C. M.; Kim, C.; Park, J. H.; Russell, L. M.; Lee, K. H.; Pomper, M. G.; Searson, P. C., State-of-the-art in design rules for drug delivery platforms: Lessons learned from FDA-approved nanomedicines. *Journal of Controlled Release* **2014,** *187*, 133-144.
5. Cedervall, T.; Lynch, I.; Lindman, S.; Berggård, T.; Thulin, E.; Nilsson, H.; Dawson, K. A.; Linse, S., Understanding the nanoparticle–protein corona using methods to quantify exchange rates and affinities of proteins for nanoparticles. *Proceedings of the National Academy of Sciences* **2007,** *104* (7), 2050-2055.
6. Lundqvist, M.; Stigler, J.; Elia, G.; Lynch, I.; Cedervall, T.; Dawson, K. A., Nanoparticle size and surface properties determine the protein corona with possible implications for biological impacts. *Proceedings of the National Academy of Sciences* **2008,** *105* (38), 14265-14270.
7. Olbrich, C.; Gessner, A.; Schröder, W.; Kayser, O.; Müller, R. H., Lipid–drug conjugate nanoparticles of the hydrophilic drug diminazene—cytotoxicity testing and mouse serum adsorption. *Journal of Controlled Release* **2004,** *96* (3), 425-435.
8. Göppert, T. M.; Müller, R. H., Protein adsorption patterns on poloxamer- and poloxamine-stabilized solid lipid nanoparticles (SLN). *European Journal of Pharmaceutics and Biopharmaceutics* **2005,** *60* (3), 361-372.
9. Gossmann, R.; Fahrländer, E.; Hummel, M.; Mulac, D.; Brockmeyer, J.; Langer, K., Comparative examination of adsorption of serum proteins on HSA- and PLGA-based nanoparticles using SDS–PAGE and LC–MS. *European Journal of Pharmaceutics and Biopharmaceutics* **2015,** *93*, 80-87.
10. Cedervall, T.; Lynch, I.; Foy, M.; Berggård, T.; Donnelly, S. C.; Cagney, G.; Linse, S.; Dawson, K. A., Detailed Identification of Plasma Proteins Adsorbed on Copolymer Nanoparticles. *Angew. Chem. Int. Ed.* **2007,** *46* (30), 5754-5756.
11. Tenzer, S.; Docter, D.; Kuharev, J.; Musyanovych, A.; Fetz, V.; Hecht, R.; Schlenk, F.; Fischer, D.; Kiouptsi, K.; Reinhardt, C.; Landfester, K.; Schild, H.; Maskos, M.; Knauer, S. K.; Stauber, R. H., Rapid formation of plasma protein corona critically affects nanoparticle pathophysiology. *Nature Nanotechnology* **2013,** *8*, 772-781.
12. Deng, Z. J.; Mortimer, G.; Schiller, T.; Musumeci, A.; Martin, D.; Minchin, R. F., Differential plasma protein binding to metal oxide nanoparticles. *Nanotechnology* **2009,** *20* (45), 1-9.
13. Dobrovolskaia, M. A.; Patri, A. K.; Zheng, J.; Clogston, J. D.; Ayub, N.; Aggarwal, P.; Neun, B. W.; Hall, J. B.; McNeil, S. E., Interaction of colloidal gold nanoparticles with human blood: effects on particle size and analysis of plasma protein binding profiles. *Nanomedicine: Nanotechnology, Biology and Medicine* **2009,** *5* (2), 106-117.
14. Cukalevski, R.; Lundqvist, M.; Oslakovic, C.; Dahlbäck, B.; Linse, S.; Cedervall, T., Structural Changes in Apolipoproteins Bound to Nanoparticles. *Langmuir* **2011,** *27* (23), 14360-14369.

15. Winzen, S.; Schoettler, S.; Baier, G.; Rosenauer, C.; Mailaender, V.; Landfester, K.; Mohr, K., Complementary analysis of the hard and soft protein corona: sample preparation critically effects corona composition. *Nanoscale* **2015,** *7* (7), 2992-3001.
16. Dell'Orco, D.; Lundqvist, M.; Oslakovic, C.; Cedervall, T.; Linse, S., Modeling the Time Evolution of the Nanoparticle-Protein Corona in a Body Fluid. *PLoS One* **2010,** *5* (6), e10949.
17. Fagerberg, L.; Hallstrom, B. M.; Oksvold, P.; Kampf, C.; Djureinovic, D.; Odeberg, J.; Habuka, M.; Tahmasebpoor, S.; Danielsson, A.; Edlund, K.; Asplund, A.; Sjostedt, E.; Lundberg, E.; Szigyarto, C. A.-K.; Skogs, M.; Takanen, J. O.; Berling, H.; Tegel, H.; Mulder, J.; Nilsson, P.; Schwenk, J. M.; Lindskog, C.; Danielsson, F.; Mardinoglu, A.; Sivertsson, A.; Felitzen, K. v.; Forsberg, M.; Zwahlen, M.; Olsson, I.; Navani, S.; Huss, M.; Nielsen, J.; Ponten, F.; Uhlen, M., Analysis of the human tissue-specific expression by genome-wide integration of transcriptomics and antibody-based proteomics. *Molecular & Cellular Proteomics* **2014,** *13* (2), 397-406.
18. Shevchenko, A.; Tomas, H.; Havli, J.; Olsen, J. V.; Mann, M., In-gel digestion for mass spectrometric characterization of proteins and proteomes. *Nature Protocols* **2006,** *1* (6), 2856-2860.
19. Freire, E.; Mayorga, O. L.; Straume, M., Isothermal titration calorimetry. *Analytical Chemistry* **1990,** *62* (18), 950A-959A.
20. McCarthy, J. R.; Perez, J. M.; Brückner, C.; Weissleder, R., Polymeric Nanoparticle Preparation that Eradicates Tumors. *Nano Letters* **2005,** *5* (12), 2552-2556.
21. Bisswanger, H., Multiple Equilibria. In *Enzyme Kinetics: Principles and Methods*, Wiley-VCH Verlag GmbH & Co. KGaA: 2008.
22. Lauffenburger, D. A.; Linderman, J. J., Cell Surface Receptor Binding Models. In *Receptors: Models for Binding, Trafficking, and Signaling*, Oxford University Press: 1996.
23. Camus, M.-C.; Chapman, M. J.; Forgez, P.; Laplaud, P. M., Distribution and characterization of the serum lipoproteins and apoproteins in the mouse, Mus musculus. *Journal of Lipid Research* **1983,** *24* (9), 1210-1218.
24. Parolini, C.; Chiesa, G.; Zhu, Y.; Forte, T.; Caligari, S.; Gianazza, E.; Sacco, M. G.; Sirtori, C. R.; Rubin, E. M., Targeted Replacement of Mouse Apolipoprotein A-I with Human ApoA-I or the Mutant ApoA-I_{Milano}: Evidence of ApoA-I_M Impaired Hepatic Secretion *Journal of Biological Chemistry* **2003,** *278* (7), 4740-4746.
25. Hutchins, P. M.; Ronsein, G. E.; Monette, J. S.; Pamir, N.; Wimberger, J.; He, Y.; Anantharamaiah, G. M.; Kim, D. S.; Ranchalis, J. E.; Jarvik, G. P.; Vaisar, T.; Heinecke, J. W., Quantification of HDL Particle Concentration by Calibrated Ion Mobility Analysis. *Clinical Chemistry* **2014,** *60* (11), 1393-1401.
26. Müller, J.; Prozeller, D.; Ghazaryan, A.; Kokkinopoulou, M.; Mailänder, V.; Morsbach, S.; Landfester, K., Beyond the protein corona - lipids matter for biological response of nanocarriers. *Acta Biomaterialia* **2018,** *71*, 420-431.
27. Duan, Y.; Liu, Y.; Shen, W.; Zhong, W., Fluorescamine Labeling for Assessment of Protein Conformational Change and Binding Affinity in Protein–Nanoparticle Interaction. *Analytical Chemistry* **2017,** *89*, 12160-12167.
28. Daniels, K. G.; Suo, Y.; Oas, T. G., Conformational kinetics reveals affinities of protein conformational states. *Proceedings of the National Academy of Sciences* **2015,** *112* (30), 9352-9357.
29. Kono, M.; Okumura, Y.; Tanaka, M.; Nguyen, D.; Dhanasekaran, P.; Lund-Katz, S.; Phillips, M. C.; Saito, H., Conformational Flexibility of the N-terminal Domain of Apolipoprotein A-I Bound to Spherical Lipid Particles. *Biochemistry* **2008,** *47* (43), 11340-11347.

30. Jordan, M. B.; Rooijen, N. v.; Izui, S.; Kappler, J.; Marrack, P., Liposomal clodronate as a novel agent for treating autoimmune hemolytic anemia in a mouse model. *Blood* **2003,** *101* (2), 594-601.
31. Rooijen, N. v.; Nieuwmegen, R. v., Elimination of phagocytic cells in the spleen after intravenous injection of liposome-encapsulated dichloromethylene diphosphonate: an enzyme-histochemical study. *Cell and Tissue Research* **1984,** *238*, 355-358.
32. Feng, H.; Guo, L.; Wang, D.; Gao, H.; Hou, G.; Zheng, Z.; Ai, J.; Foreman, O.; Daugherty, A.; Li, X.-A., Deficiency of SR-BI Leads to Impaired Lymphocyte Homeostasis and Autoimmune Disorders in Mice. *Arteriosclerosis, Thrombosis, and Vascular Biology* **2011,** *31* (11), 2543-2551.
33. Pal, R.; Ke, Q.; Pihan, G. A.; Yesilaltay, A.; Penman, M. L.; Wang, L.; Chitraju, C.; Kang, P. M.; Krieger, M.; Kocher, O., Carboxy-terminal deletion of the HDL receptor reduces receptor levels in liver and steroidogenic tissues, induces hypercholesterolemia, and causes fatal heart disease. *American Journal of Physiology-Heart and Circulatory Physiology* **2016,** *311* (6), H1392-H1408.
34. van-Rooijen, N.; Sanders, A.; van-den-Berg, T. K., Apoptosis of macrophages induced by liposome-mediated intracellular delivery of clodronate and propamidine. *Journal of Immunological Methods* **1996,** *193* (1), 93-99.
35. Van-Rooijen, N.; Sanders, A., Liposome mediated depletion of macrophages: mechanism of action, preparation of liposomes and applications. *Journal of Immunological Methods* **1994,** *174* (1-2), 83-93.
36. Fleisch, H., Bisphosphonates: A New Class of Drugs in Diseases of Bone and Calcium Metabolism In *Bisphosphonates and Tumor Osteolysis. Recent Results in Cancer Research*, Brunner, K. W.; Fleisch, H.; Senn, H. J., Eds. Springer: Berlin, Heidelberg, 1989; Vol. 116, pp 1-28.
37. Koay, M. A.; Gao, X.; Washington, M. K.; Parman, K. S.; Sadikot, R. T.; Blackwell, T. S.; Christman, J. W., Macrophages Are Necessary for Maximal Nuclear Factor- κ B Activation in Response to Endotoxin. *American Journal of Respiratory Cell and Molecular Biology* **2002,** *26* (5), 572-578.
38. Chow, A.; Lucas, D.; Hidalgo, A.; Méndez-Ferrer, S.; Hashimoto, D.; Scheiermann, C.; Battista, M.; Leboeuf, M.; Prophete, C.; van-Rooijen, N.; Tanaka, M.; Merad, M.; Frenette, P. S., Bone marrow CD169+ macrophages promote the retention of hematopoietic stem and progenitor cells in the mesenchymal stem cell niche. *Journal of Experimental Medicine* **2011,** *208* (2), 261-271.
39. Landsman, L.; Jung, S., Lung Macrophages Serve as Obligatory Intermediate between Blood Monocytes and Alveolar Macrophages. *Journal of Immunology* **2007,** *179* (6), 3488-3494.
40. Gordon, S.; Taylor, P. R., Monocyte and macrophage heterogeneity. *Nature Reviews Immunology* **2005,** *5*, 953-964.
41. Tatham, K. C.; O'Dea, K. P.; Romano, R.; Donaldson, H. E.; Wakabayashi, K.; Patel, B. V.; Thakuria, L.; Simon, A. R.; Sarathchandra, P.; Marczin, N.; Takata, M., Intravascular donor monocytes play a central role in lung transplant ischaemia-reperfusion injury. *Thorax* **2018,** *73* (4), 350-360.
42. Krieger, M., Scavenger receptor class B type I is a multiligand HDL receptor that influences diverse physiologic systems. *Journal of Clinical Investigation* **2001,** *108* (6), 793-797.
43. Huby, T.; Doucet, C.; Dachet, C.; Ouzilleau, B.; Ueda, Y.; Afzal, V.; Rubin, E.; Chapman, M. J.; Lesnik, P., Knockdown expression and hepatic deficiency reveal an atheroprotective role for SR-BI in liver and peripheral tissues. *Journal of Clinical Investigation* **2006,** *116* (10), 2767-2776.

44. Rigotti, A.; Trigatti, B. L.; Penman, M.; Rayburn, H.; Herz, J.; Krieger, M., A targeted mutation in the murine gene encoding the high density lipoprotein (HDL) receptor scavenger receptor class B type I reveals its key role in HDL metabolism. *Proceedings of the National Academy of Sciences* **1997,** *94* (23), 12610-12615.
45. Brodeur, M. R.; Luangrath, V.; Bourret, G.; Falstrault, L.; Brissette, L., Physiological importance of SR-BI in the in vivo metabolism of human HDL and LDL in male and female mice. *Journal of Lipid Research* **2005,** *46*, 687-696.
46. Badeau, R. M.; Metso, J.; Wähälä, K.; Tikkanen, M. J.; Jauhiainen, M., Human macrophage cholesterol efflux potential is enhanced by HDL-associated 17β-estradiol fatty acyl esters. *The Journal of Steroid Biochemistry and Molecular Biology* **2009,** *116* (1-2), 44-49.
47. Khoudary, S. R. E.; Hutchins, P. M.; Matthews, K. A.; Brooks, M. M.; Orchard, T. J.; Ronsein, G. E.; Heinecke, J. W., Cholesterol Efflux Capacity and Subclasses of HDL Particles in Healthy Women Transitioning Through Menopause. *Journal of Endocrinology and Metabolism* **2016,** *101* (9), 3419–3428.
48. Ulloa, N.; Arteaga, E.; Bustos, P.; Duran-Sandoval, D.; Schulze, K.; Castro, G.; Jauhiainen, M.; Fruchart, J. C.; Calvo, C., Sequential estrogen-progestin replacement therapy in healthy postmenopausal women: effects on cholesterol efflux capacity and key proteins regulating high-density lipoprotein levels. *Metabolism* **2002,** *51* (11), 1410-1417.
49. Rinn, J. L.; Rozowsky, J. S.; Laurenzi, I. J.; Petersen, P. H.; Zou, K.; Zhong, W.; Gerstein, M.; Snyder, M., Major Molecular Differences between Mammalian Sexes Are Involved in Drug Metabolism and Renal Function. *Developmental Cell* **2004,** *6* (6), 791-800.
50. O'Malley, K.; Crooks, J.; Duke, E.; Stevenson, I. H., Effect of Age and Sex on Human Drug Metabolism. *British Medical Journal* **1971,** *3* (5775), 607-609.

Appendix A

A.1 Isothermal Titration Calorimetry: Single Set of Independent Sites Binding Model

In this model, we assume that the nanoparticle (N) contains identical and independent binding sites for the ligand (L), and that the ligand binds without any cooperative effects. The reaction under consideration can then be written as,

$$[N] + [L] \rightleftharpoons [NL] \tag{A1}$$

$$[N_T] = [NL] + [N] \tag{A2}$$

$$[L_T] = [NL] + [L] \tag{A3}$$

where [N] and [L] are the concentrations of free nanoparticle and ligand respectively. $[N_T]$ and $[L_T]$ are the total concentrations of nanoparticle and ligand respectively while [NL] is the nanoparticle-ligand complex concentration.

The equilibrium association constant of the interaction of nanoparticle with ligand can be expressed as,

$$K_a = \frac{[NL]}{[N][L]} = \frac{\Theta}{(1 - \Theta)[L]} \tag{A4}$$

where Θ is the fractional saturation, that is, the fraction occupancy of ligand binding sites on a nanoparticle saturated, and by conservation of mass,

$$[L_T] = [L] + n\Theta[N_T] \tag{A5}$$

where n is the number of binding sites and combining equations (4) and (5) gives a quadratic equation,

$$\Theta^2 - \Theta\left(1 + \frac{1}{nK_a[N_T]} + \frac{[L_T]}{n[N_T]}\right) + \frac{[L_T]}{n[N_T]} = 0 \tag{A6}$$

Solving the quadratic equation gives the root of Θ,

$$\Theta = \frac{1}{2}\left(1 + \frac{1}{nK_a[N_T]} + \frac{[L_T]}{n[N_T]} - \sqrt{\left(1 + \frac{1}{nK_a[N_T]} + \frac{[L_T]}{n[N_T]}\right)^2 - \frac{4[L_T]}{n[N_T]}}\right) \quad (A7)$$

The total heat of reaction Q in the cell is then given by,

$$Q = n\Theta[N_T]V_0\Delta H \quad (A8)$$

where V_0 is the cell volume and ΔH is the molar heat of ligand binding

Taking into consideration the injection volume ΔV_i for injection i, a correction is needed to account for this displaced volume. The displaced volume contributes about 50% as much heat as an equivalent material in the working volume V_0, such that the heat released from the i^{th} injection is,

$$\Delta Q_i = Q_i + \frac{\Delta V_i}{V_0}\left(\frac{Q_i + Q_{i-1}}{2}\right) - Q_{i-1} = Q_i\left(1 + \frac{\Delta V_i}{V_0}\right) - Q_{i-1}\left(1 - \frac{\Delta V_i}{V_0}\right) \quad (A9)$$

The procedure of fitting the experimental data involves making initial guesses to n, K_a and ΔH. Using these initial guesses, the heat ΔQ_i for each injection is calculated and compared to the measured heat values for the corresponding experimental injection. Optimizations to the parameters, n, K_a and ΔH, are done with Levenberg-Marquardt methods and further iterations are carried out until no significant improvement is observed and the fit parameters converge.

To calculate change in entropy (ΔS), the reaction isotherm equation (A10) and Gibbs-Helmholtz (A11) are combined to solve for ΔS (A12),

$$\Delta G = -RT \cdot lnK_a \quad (A10)$$

$$\Delta G = \Delta H - T \cdot \Delta S \quad (A11)$$

$$\Delta S = R \cdot lnK_a + \frac{\Delta H}{T} \quad (A12)$$

where ΔG is the Gibbs free energy, T is the temperature and R is the universal gas constant. ΔS can then be calculated for known values of K_a and ΔH

A.2 Protein Gel Calibration

Several known concentrations of BSA were made and used to calibrate the in-gel standard (1/20X mouse plasma). Any protein band on the 1/20X band profile can be used as a relative standard and all major protein bands on the 1/20X profile can be quantified and serve as in-gel standards for the nanoparticle-protein binding experiments.

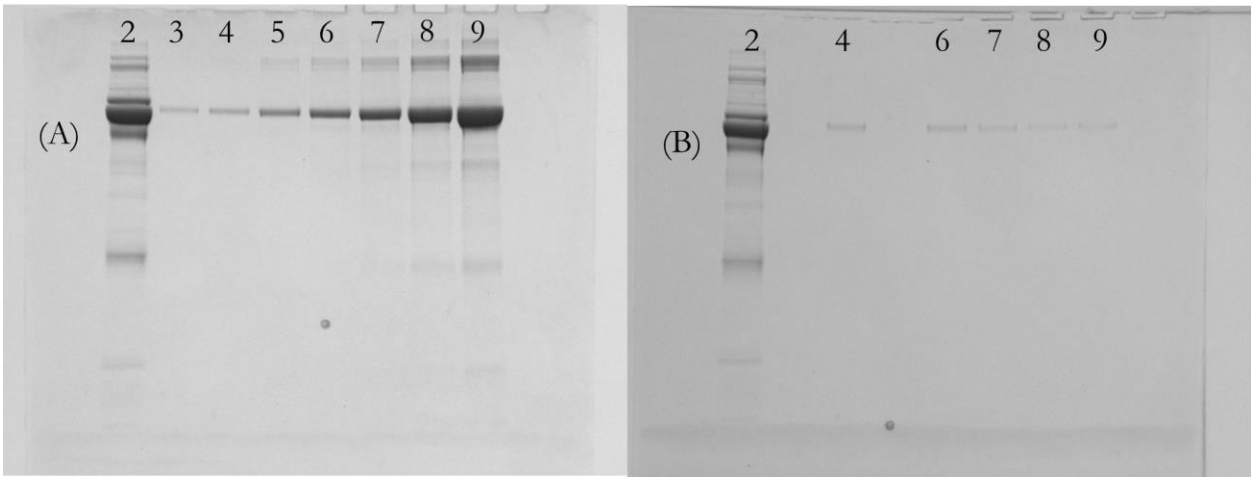


Figure A.2-1 Protein Gel Calibration of 1/20X Plasma with BSA in 10-well Gels. (A) Lane 2- 1/20X plasma, lane 3- 0.175 µg, lane 4- 0.25 µg, lane 5- 0.5 µg, lane 6- 1 µg, lane 7- 2 µg, lane 8- 4 µg, lane 9- 8 µg. (B) Lane 2- 1/20X plasma, lane 4- 0.15 µg, lane 6- 0.125 µg, lane 7- 0.1 µg, lane 8- 0.05 µg, lane 9- 0.075 µg

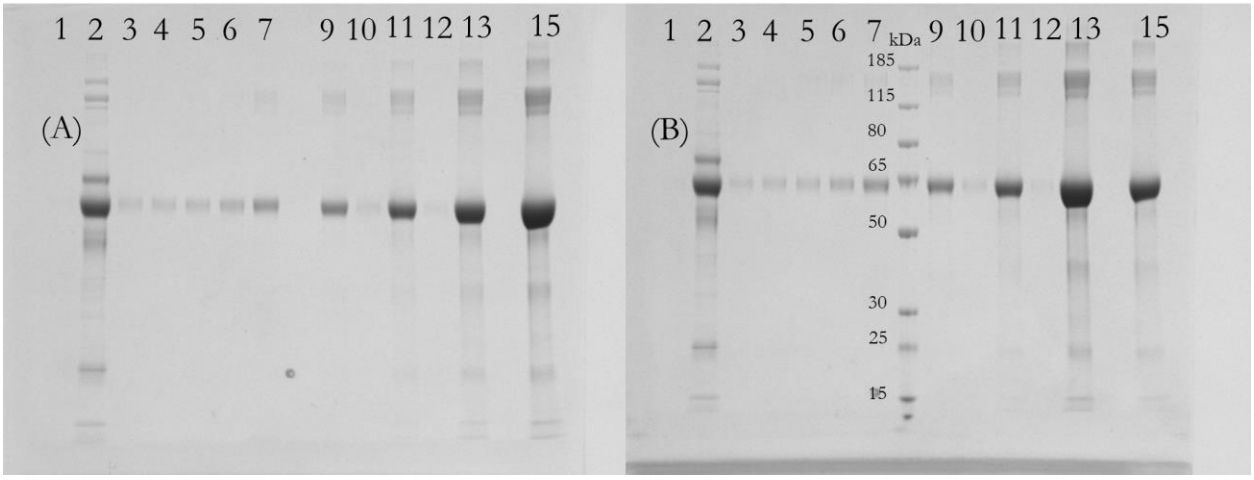


Figure A.2-2 Protein Gel Calibration of 1/20X Plasma with BSA in 15-well Gels. (A) and (B) Lane 1- 0.05 µg, lane 2- 1/20X plasma, lane 3- 0.125 µg, lane 4- 0.15 µg, lane 5- 0.175 µg, lane 6- 0.25 µg, lane 7- 0.5 µg, lane 9- 1 µg, lane 10- 0.1 µg, lane 11- 2 µg, lane 12- 0.075 µg, lane 13- 8 µg, lane 15- 4 µg.

A.3 Representative Protein Gels for the Binding of Nanoparticles to Plasma Proteins

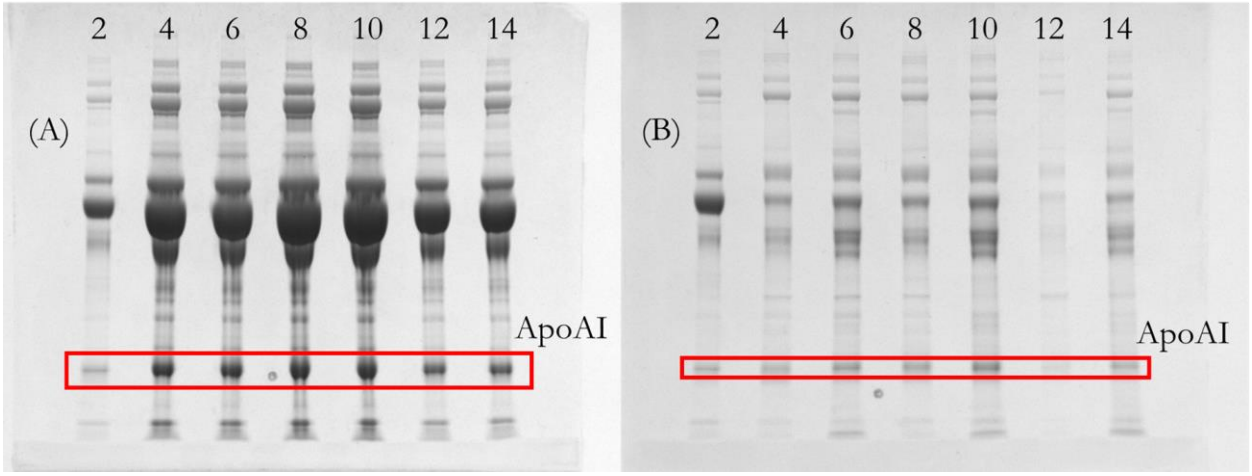


Figure A.3-1 Protein Gels of PSCOOH Binding to 1/5X – 1/2X plasma. (A) 2- 1/20X standard, 4- 1/3X plasma, 6- 1/3X plasma + PSCOOH, 8- 1/2X plasma, 10- 1/2X + PSCOOH, 12- 1/5X plasma, 14- 1/5X plasma + PSCOOH. Lane 4 – 14, supernatant. (B) Same as (A) except lane 4 – 14 is pellet.

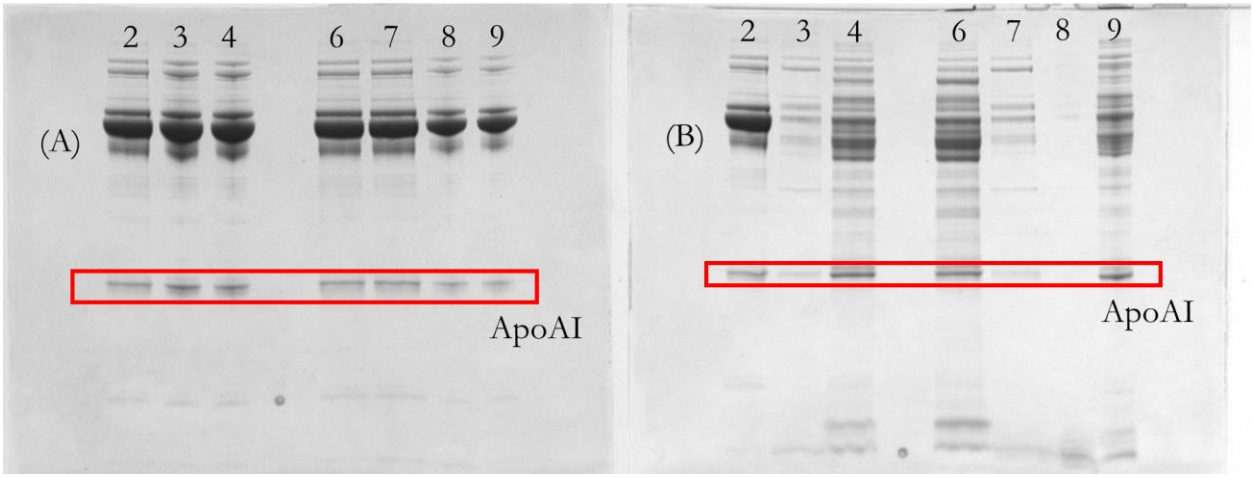


Figure A.3-2 Protein Gels of PSCOOH Binding to 100X – 1/20X plasma. (A) 2- 1/20X standard, 3- 1/50X, 4- 1/50X + PSCOOH, 6- 1/20X + PSCOOH, 7- 1/20X, 8- 1/100X, 9- 1/100X + PSCOOH. Lane 3 – 9, supernatant. (B) Same as (A) except lane 3 – 9 is pellet

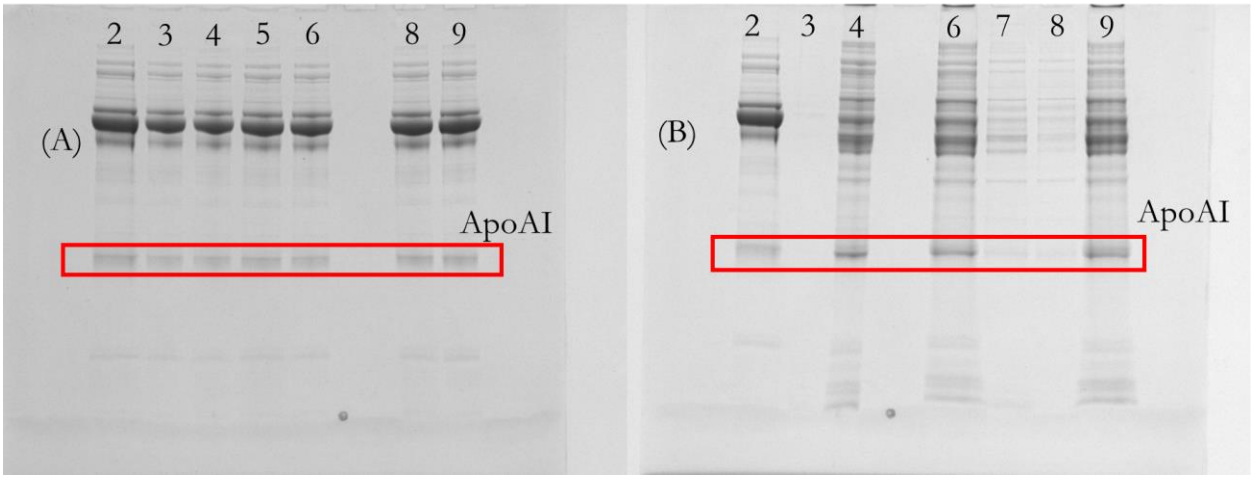


Figure A.3-3 Protein Gels of PSCOOH Binding to 100X – 1/60X plasma. (A) 2- 1/20X standard, 3- 1/100X + PSCOOH, 4- 1/100X, 5- 1/70X, 6- 1/70X + PSCOOH, 8- 1/60X, 9- 1/60X + PSCOOH. Lane 3 – 9, supernatant. (B) 2- 1/20X standard, 3- 1/100X, 4- 1/100X + PSCOOH, 6- 1/70X + PSCOOH, 7- 1/70X, 8- 1/60X, 9- 1/60X + PSCOOH. Lane 3 – 9, pellet.

A.4 Size Distribution of PSCOOH Nanoparticles

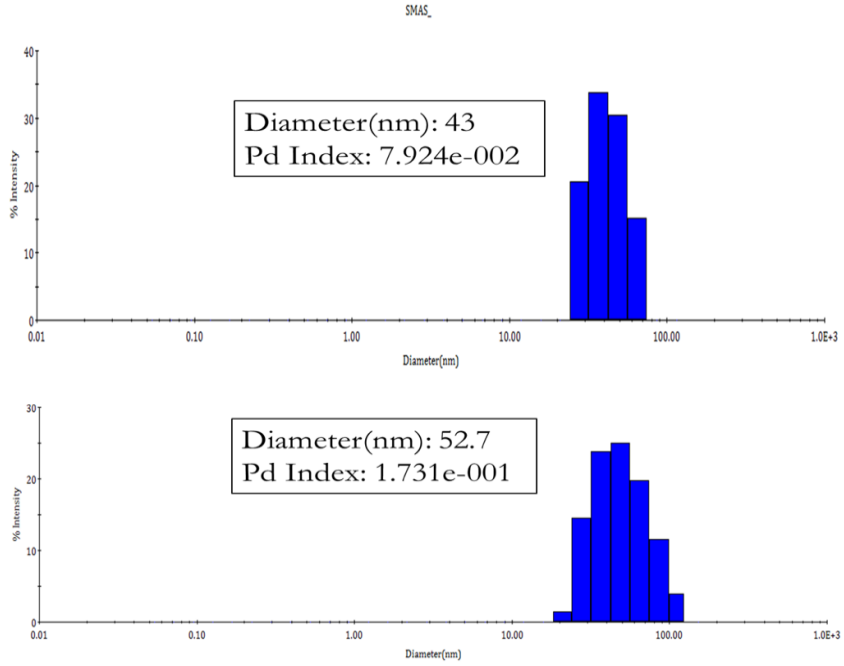


Figure A.4-1 Top Panel: PSCOOH. Bottom Panel: PSCOOH-DiR

A.5 CD Profile of the Structural Changes of mHDL in $PSNH_2$ Nanoparticles

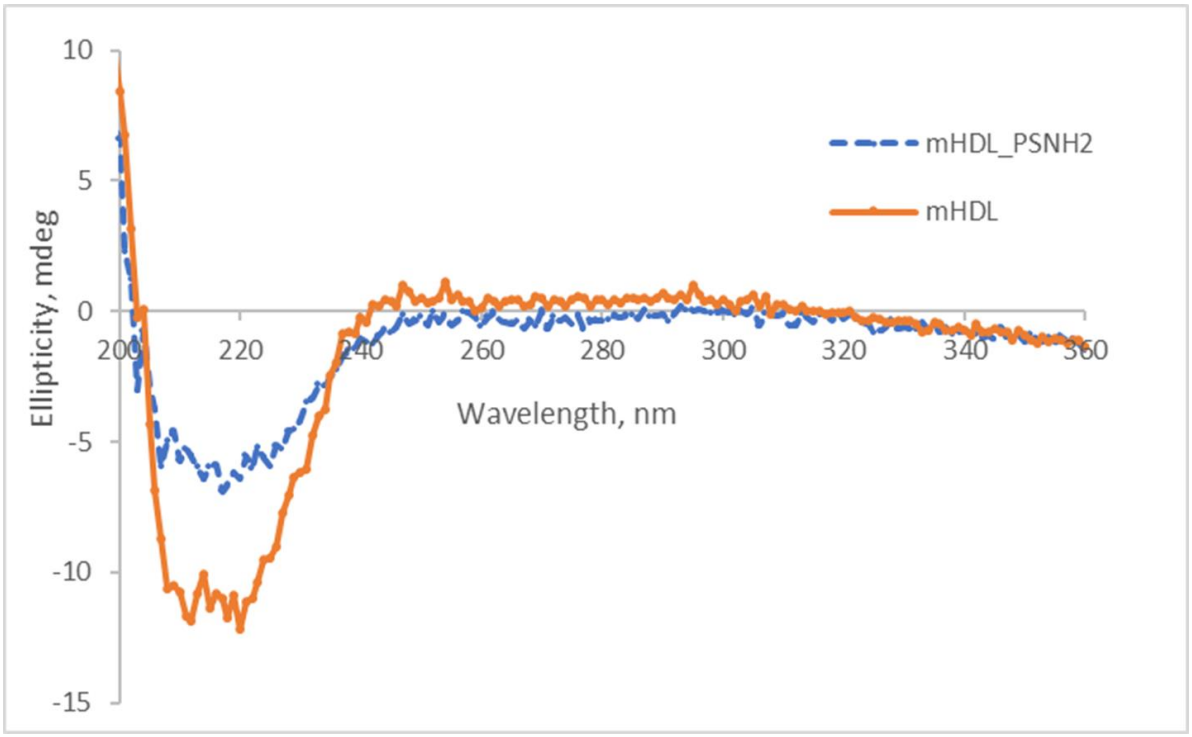


Figure A.5-1 Secondary Structural Changes Of mHDL Incubated With $PSNH_2$ Nanoparticles.

A.6 UV-VIS Absorbance Profile Showing Protein Depletion and Protein Gel Displaying the Plateau of ApoA-I

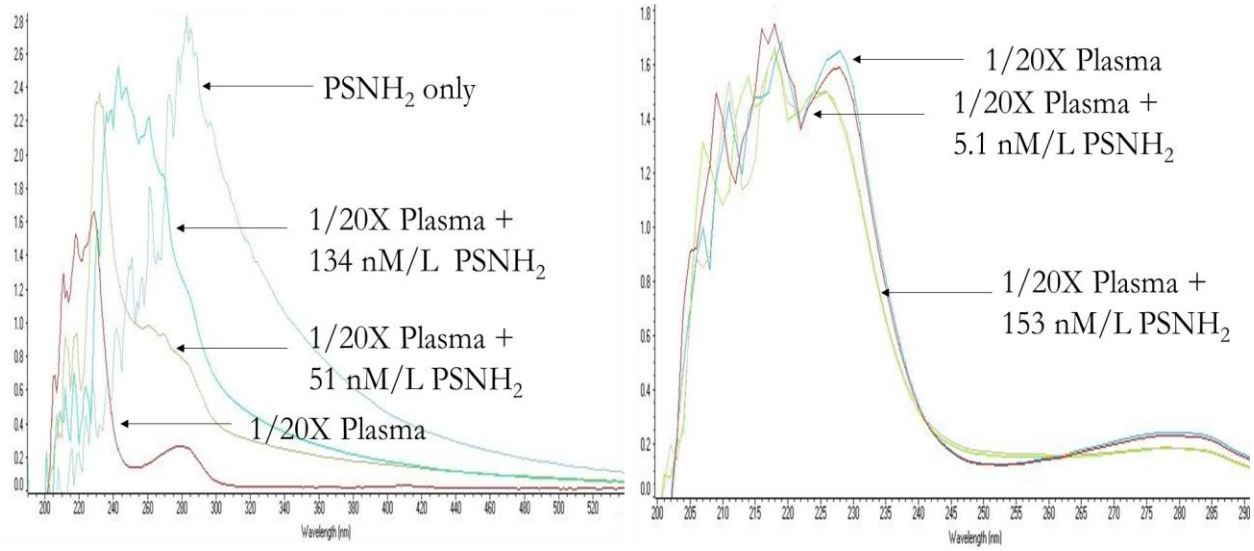


Figure A.6-1 Absorbance Spectra Showing Complete Nanoparticle Pelletization After Ultracentrifugation. Left Panel: Depicting absorbance spectra without ultracentrifugation. Right Panel: Depicting the supernatant absorbance spectra after ultracentrifugation of the $PSNH_2$ and 1/20X plasma suspensions

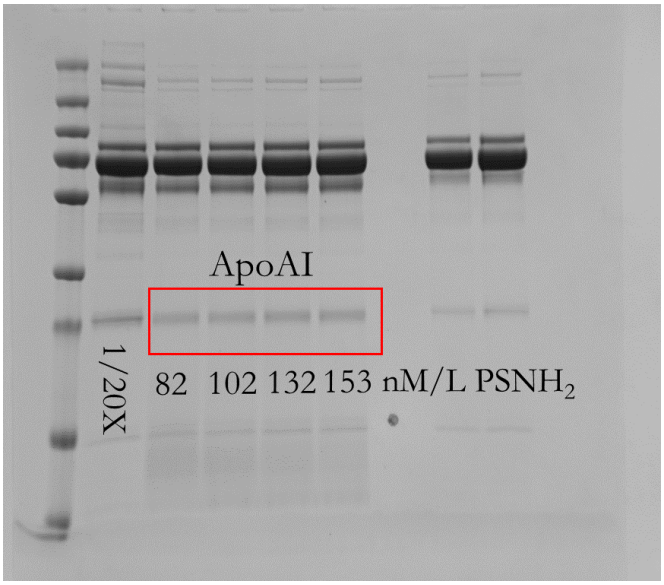


Figure A.6-2 Protein Gel Showing the ApoA-I Bands from the Supernatant After Ultracentrifugation

A.7 Protein Gels from mHDL Isolation by Anion Exchange Chromatography

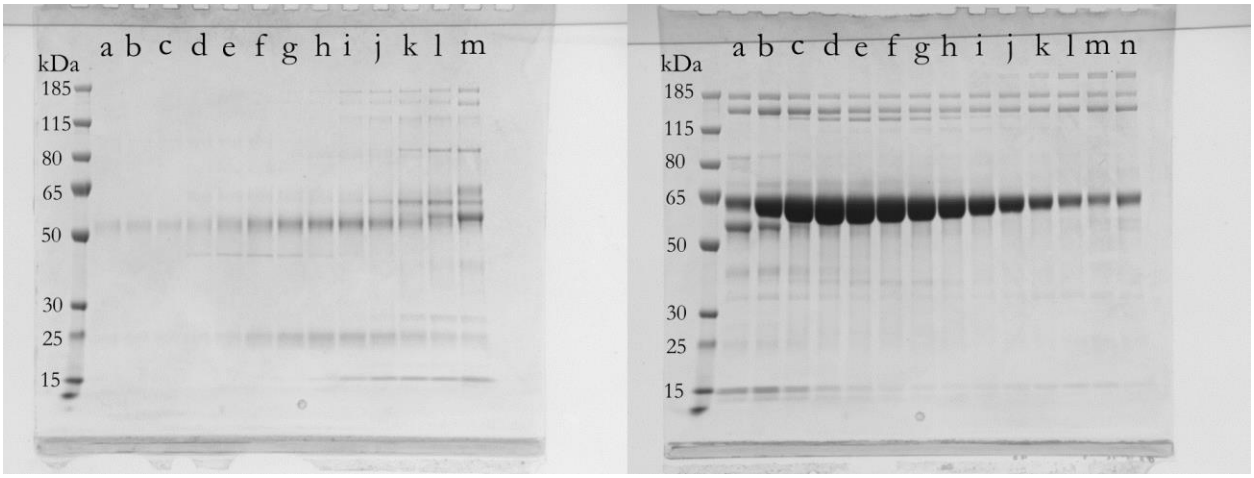


Figure A.7-1 Protein Gels Depicting the Elution of One or More Distinct Plasma Proteins Prior to Changing the Salt Gradient Scheme. Left Panel: a-b, fraction 44 – 46; d – m, fraction 51-60. Right Panel: a-m, fraction 61-74.

A.8 Gel Filtration Chromatography Calibration Curve

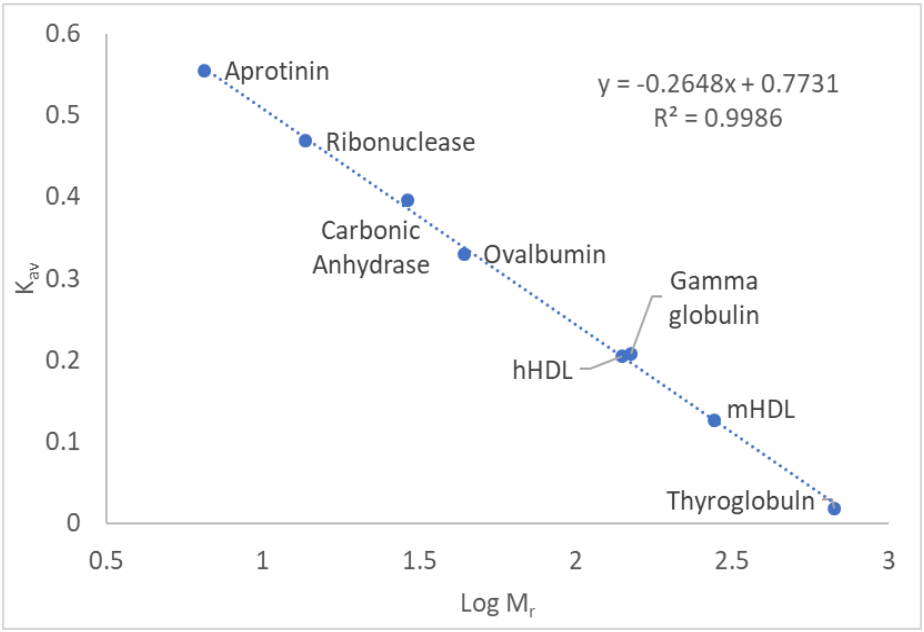


Figure A.8-1 Calibration Curve for Estimating the Molecular Weights of mHDL and hHDL

A.9 PCR Genotyping with Genomic DNA from Mice Tails

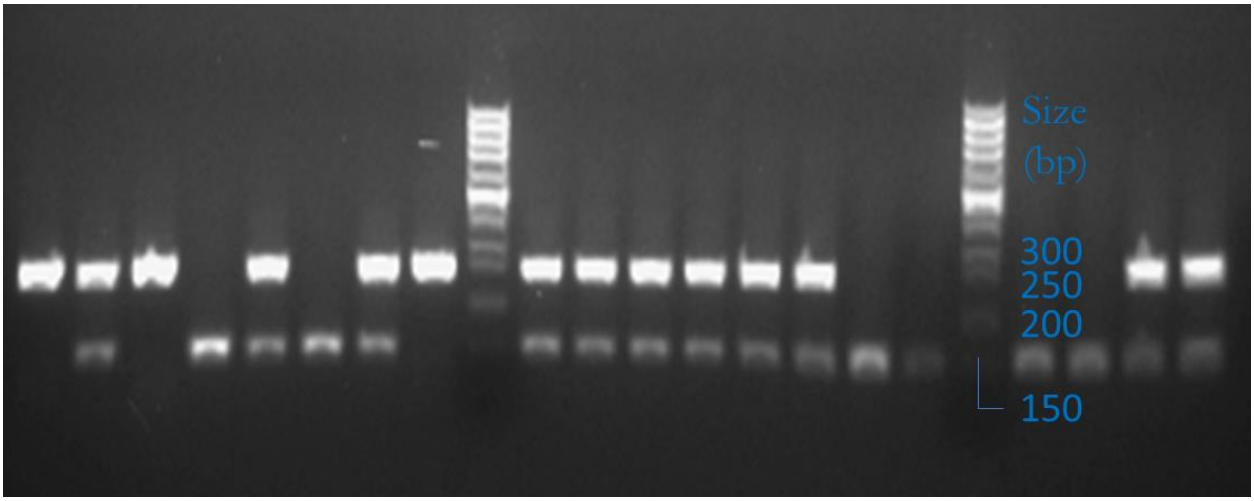


Figure A.9-1 SCARBI^{tm1kri} Genotyping with PCR. Wild-type represent one 262 bp band, mutant represents one 140 bp band, while heterozygous represents both 140 bp and 262 bp bands.

A.10 Body Weight and Organ Weight of Mice

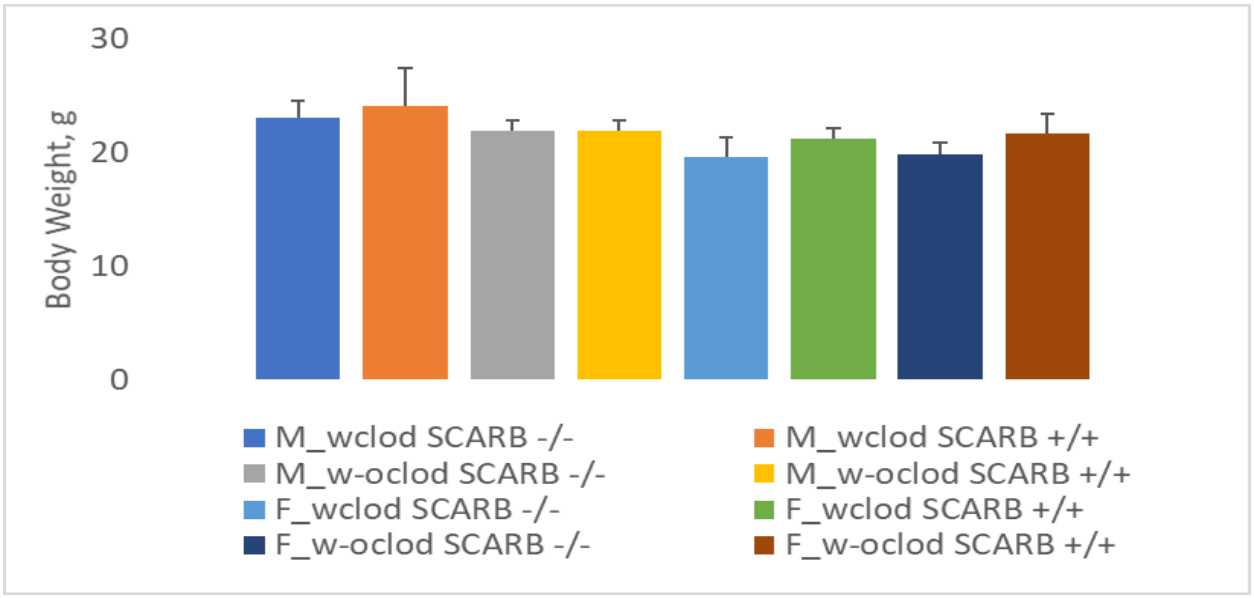


Figure A.10-1 Body weight of male and female SCARBI+/+ and SCARB-/- mice

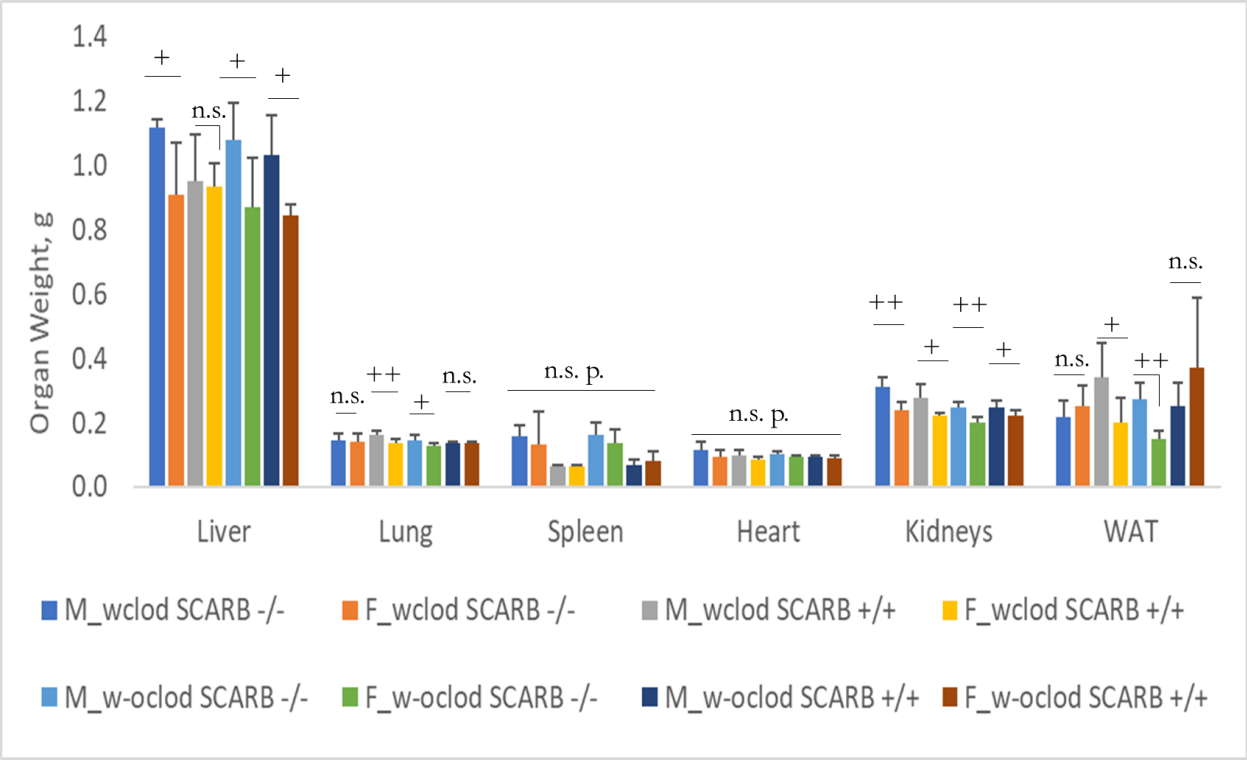


Figure A.10-2 Organ weight differences between male and female mice injected with either clodronate liposomes or control liposomes. + $p < 0.05$, ++ $p < 0.01$ as determined by the t-test (an F-test for equal and unequal variances was done and the corresponding t-test was applied). n.s. p. denotes no significant difference between all the male-female pairs within a clodronate liposome or control liposome group.

CHAPTER III

The Localization of Soft Nanoparticles to the Liver and Spleen is Significantly Reduced in Obese Mice

3.1 Abstract

Due to the prevalence of overweight and obese individuals in the United States being 70% and 30% respectively among adults, it is likely that many prospective patients that will be administered nanotherapies will have additional metabolic complications. Yet, studies on the distribution of nanoparticles and their efficacy occur mostly in lean rodents. Here, we determined the biodistribution of model nanoparticles – filomicelles – as a function of mouse diet and weight utilizing three strains: C57BL/6J, KK-A^y, and ob/ob. C57BL/6J mice are largely resistant to significant weight gain, but KK-A^y and ob/ob mice become obese on a high-fat diet. I found that there was a significant drop in the accumulation of nanoparticles in the livers and spleens of KK-A^y and ob/ob mice as their weights increased. Interestingly, almost no nanoparticles localized to the white adipose tissue (WAT) of any of the mice. These results have significant implications for patients with altered metabolic states.

3.2 Introduction

The biodistribution of a nanoparticle in model mammals such as mice provides clues as to the future promise of nanoparticles in treating human diseases. However, the vast majority of experiments that determine the biodistribution of nanoparticles take place after administration to metabolically healthy rodents.[1] This methodology has provided a wealth of insight into mammalian response to nanoparticles. However, the vast majority of patients that will potentially be administered nanoparticles in the clinic will be overweight to obese and have widely varying metabolic conditions. These imbalances could greatly affect nanoparticle biodistribution and future efficacy.[2-3]

Here, I determined the biodistribution of cylindrical poly-ethylene-oxide–block-poly-butadiene PEO-*b*-PBD filomicelles in three mouse strains: C57BL/6J, KK-A^y, and ob/ob. C57BL/6J (wild-type) mice are not an ideal model for diet-induced obesity, thus the need for the KK-A^y and ob/ob strains. However, I was able to maintain the

weights of the KK-A^y and ob/ob mice at lean C57BL/6J levels (~25-30 g) by limiting their diets to 4 grams of low-fat feed (LFD) per mouse per day. I determined that nanoparticle localization to the liver and the spleen decreased by up to factors of ~4 and ~10, respectively, from the lean (~30 grams) to the heaviest (~55-60 g) KK-A^y and ob/ob mice. Nanoparticle signal in WAT was just above background, indicating that it is not a major sink. This also indicates that any adipose tissue macrophages (ATMs) had a limited role in nanoparticle clearance. My results show that mammalian diet and weight play crucial roles in the biodistribution of model nanoparticles.

3.3 Materials and Methods

3.3.1 Synthesis of Diblock Copolymers for Filomicelles

Poly-ethylene-oxide-*block*-poly-butadiene (PEO-*b*-PBD) copolymers were synthesized following the techniques of Hillmyer and Bates.[4] *s*-BuLi (1.4 M in cyclohexane; Sigma-Aldrich #195596) and *n*-BuLi (2.0 M in cyclohexane; Sigma-Aldrich #302120) were diluted with hexane under vacuum. Potassium naphthalenide (K-Naph) was prepared with naphthalene and potassium in THF. 1,3-butadiene (BD; Sigma-Aldrich #695580) was distilled two times over *n*-BuLi sequentially and diluted with two-fold excess of THF. Ethylene oxide (EO; Sigma-Aldrich #387614) was distilled over *n*-BuLi two times sequentially and distilled again to each ampoule. Tetrahydrofuran (THF; Fisher #T397-1) was distilled under N_2 after refluxing with sodium for 5 h and over K-Naph under vacuum. All initiators and monomers were stored at -30 °C in ampoules equipped with break-seals.

The polymer number-average molecular weight and polydispersity index were determined using size exclusion chromatography (SEC) equipped with a Knauer's K-501 HPLC pump, K-2301 RI detector, K-2501 UV detector, and with a set of two columns; Polymer Standards Services, SDV-gel, 60 cm length (5 mm) 100 Å and a linear 102–106 Å. THF with toluene as a solvent flow marker, was used as an eluent at a flow rate of 1.0 mL min^{-1}, and

the SEC was calibrated using polystyrene (PS) standards obtained from Pressure Chemicals (Pittsburgh, USA). The ^{1}H-NMR spectra (JEOL JNMLA300WB) were measured using $CDCl_3$ as the solvent.

The anionic polymerization of butadiene (BD) was performed under high-vacuum conditions (10^{-6} Torr) in sealed glass apparatus equipped with break-seals. The polymerization reactors was washed with the initiator solutions of K-Naph in THF after sealed off from the vacuum line. The initiator solution of *s*-BuLi in hexane (1.22 mmol, 0.61M) was transferred into the reactor and stabilized at -60 °C for 5 min. The monomer solution of butadiene in THF (3.2g, 59.2 mmol, 1.2 M) was introduced quickly into the initiator solution at -60 °C. The solution turned deep yellow, which indicated successful initiation. The polymerization was carried out at -60 °C and the color of polymeric solution became light orange. After 6 h, ethylene oxide (1.0 ml, 20 mmol) was added at -60 °C and the reaction became colorless rapidly. The end-capping reaction of living polybutadiene with EO was carried out with stirring at room temperature overnight. The reaction was terminated with acidic methanol. The hydroxyl-end capping polybutadiene (PBD-OH) was precipitated in a large amount of methanol and dried in vacuum oven for 3 days. The polymer (3.23 g) was obtained with 99.5 % of yield and characterized using ^{1}H-NMR and SEC. Molecular weight from SEC is 2,730 g/mol (polydispersity index: 1.06). ^{1}H-NMR spectra ($CDCl_3$, 500 MHz), δ (ppm): 5.6-5.2 (CH_2-C**H**=C**H**-CH_2- and CH_2=C**H**-CH-), 5.0-4.8 (C**H**$_2$=CH-CH-), 3.6 (-C**H**$_2$-OH), 2.3-1.8 (C**H**$_2$-CH=CH-C**H**$_2$-and CH_2=CH-C**H**-), 1.5-1.0 (CH_2=CH-CH-C**H**$_2$-), 0.85(-C**H**$_3$ from initiator).

The viscous polymer of PBD-OH (3.0 g, 55.5 mmol) was dried under reduced pressure for 3 days and the solution of PBD-OH in THF (1.0 M) was prepared by distilling THF over K-Naph under vacuum. The solution of PBD-OH was titrated by adding the deep green solution of potassium naphthalenide in THF drop by drop until a light green solution persisted for 1 h. The monomer of EO (3.4 ml, 68.2 mmol) was introduced to the solution. The polymerization in THF was heated to 60 °C with stirring for 5 days. The acidic methanol was added to the

solution of block copolymer PBD-*b*-PEO. The THF and methanol was evaporated completely. PBD-*b*-PEO was redissolved in chloroform and extracted with deionized water three times. After evaporation of chloroform, the block copolymer of PBD-*b*-PEO was dried by heating to 40 °C for 2 days in vacuum drying oven. The pure block copolymer of PBD-*b*-PEO (5.94 g) was obtained with 99 % of yield and characterized using ^{1}H-NMR and SEC. Molecular weight from SEC is 5,380 g/mol (polydispersity index: 1.09). ^{1}H-NMR spectra ($CDCl_3$, 500 MHz), δ (ppm): 5.6-5.2 (CH_2-C**H**=C**H**-CH_2- and CH_2=C**H**-CH-), 4.9-4.7 (m, C**H**$_2$=CH-CH-), 3.7-3.4(-O-C**H**$_2$-C**H**$_2$-O-), 2.2-1.8 (C**H**$_2$-CH=CH-C**H**$_2$-and CH_2=CH-C**H**-), 1.4-0.9 (CH_2=CH-CH-C**H**$_2$-), 0.6(-C**H**$_3$ from initiator).

3.3.2 Nanoparticle Preparation

Filomicelles were formed from PEO-*b*-PBD copolymers using film rehydration with phosphate buffered saline (PBS) as the aqueous buffer as described previously.[5] Prior to injection, copolymers that did not form filomicelles were pelleted at 25°C for 15 minutes at 15,000 x *g*. The upper phase containing the dispersed filomicelles was reserved for injection, with the amount of copolymer in the pellet being minimal. High-aspect-ratio nanoparticles such as filomicelles should not in general be forced through filters as many of the nanoparticles will be lost.[6] All nanoparticles were loaded with near-infrared (NIR) dye for imaging Life Technologies, #D-12731.[5] The dye partitions into the hydrophobic interiors of the nanoparticles and does not leak *in vivo*.[5]

3.3.3 Mice

All mouse experiments were approved by the University of Tennessee's Institutional Animal Care and Use Committee. I used C57BL/6J (Jackson Laboratories; #000664), KK-A^{y} (Jackson Laboratories; #002468), and ob/ob mice (Jackson Laboratories; #000632). I controlled their weights by the amount and duration that they were

on either low-fat (Research Diets, #D12450B) or high-fat diets (Research Diets, #D12492). All weights were recorded before both injection and 24 hours later before euthanization. No appreciable differences were observed.

3.3.4 Imaging

Mice were euthanized by cervical dislocation under isoflurane anesthesia and the organs and white adipose tissue were immediately harvested and imaged for NIR signal in the IVIS Lumina system

3.4 Results and Discussion

I wished to determine filomicelle biodistributions in mice whose weights were controlled by diet and genetics. I used C57BL/6J mice as a model system for wild-type mice. I used KK-A^y and ob/ob mice as two models of obesity. Heterozygote KK-A^y mice become obese after a few weeks on a high fat diet (HFD).[7] This is due to fat cell hypertrophy potentially caused by a reduction in hypothalamic norepinephrine and dopamine.[7] Homozygous ob/ob mice lack leptin a hormone secreted by adipocytes that acts on hypothalamic neurons to regulate energy and glucose balance.[8] The weights of the three strains of mice were controlled by diet, the duration of time on that diet, and ranged from ~25 to ~60 grams (Figure 3.1A). The leanest mice in each of the three strains had a restricted low-fat diet (LFD) of 4 grams/day per mouse. After each population of mice had reached the desired weight, three mice in each set were tail-vein injected with 100 µl of ~10 mg/ml filomicelles carrying NIR dye (filomicelles-NIR) in PBS.[5] We also injected one additional mouse with the equivalent amount of NIR dye in PBS, and one additional mouse with PBS. 48 hours after injection the mice were humanely euthanized and the liver, spleen, lungs, kidneys, WAT, and heart were immediately harvested along with the blood, which was separated into cells and plasma. I subtracted the intensity of the organs exhumed from the mice that were injected

with PBS from the intensity of the organs exhumed from the mice that were injected with filomicelles-NIR. All organs were washed with cold PBS and were immediately imaged for NIR signal using the IVIS Lumina system.

There was a significant drop in filomicelles-NIR signal across the three strains as a function of liver weight (Figure 3.1B,C). This was especially evident between KK-A^y and ob/ob mice that were on a restricted LFD diet (4 grams/day) versus mice with the same genetic backgrounds that were on an unlimited HFD (Figure 3.1C). There was a similar trend in the filomicelles-NIR signal in the spleens in these same mice (Figure 3.2A,B). There was a striking difference in the localization of filomicelles-NIR to the liver and the spleen versus WAT across all of our mouse models. Although mice on a HFD can have significant amounts of WAT (Figure 3.2C), filomicelles-NIR do not localize there (Figure 3.2D,E). Only mice that are on a LFD have NIR signals in their WAT that are above the background signal (Figure 3.2D,E). There were no major differences in the nanoparticle-NIR signals in the lungs, heart, and kidneys among any of the mice (data not shown).

The accumulation of nanoparticles in the liver and spleen decreased in obese versus lean mice and this may be due to the activity of macrophages. Macrophage populations are heterogeneous;[9] M1 macrophages are classically activated as the result of the overproduction of proinflammatory cytokines whereas M2 macrophages express immunosuppressive factors that promote tissue remodeling and help resolve inflammation.[10] However, recent work has shown that culturing macrophages in an environment of glucose, insulin, and palmitate - which emulates the metabolic condition - result in a unique phenotype called “metabolic activation”.[11] This agrees with recent findings in the literature where it was shown that migrating macrophages buffer the rest of the body from neutral lipids / fatty acids released from WAT.[12-13] It is possible that the exposure of macrophages to high levels of fatty acids inhibits their ability to engulf nanoparticles and foreign objects in general. This could also explain the

modest activity of Kupffer cells in enlarged livers and the reduction in filomicelle-NIR localization in the spleen in ob/ob mice if neutral lipids are also reaching those areas of the body in obese individuals.

Nanoparticles accumulate in WAT as a function of WAT mass, which for obese individuals can account for a large fraction of their total weight: in the ob/ob mice, WAT weight was ~¼ of their total weight. However, based on the NIR intensity of the pixels in the WAT images of obese mice, this appears to be a passive and not an active effect. The targeting of nanoparticles to WAT for obesity treatments has been of recent interest,[14-16] but a thorough study of nanoparticle distribution as a function of patient weight is – to our knowledge – lacking.

3.5 Conclusion

Here, I determined the biodistribution of soft near-infrared (NIR)-carrying filomicelles as a function of patient weight and metabolic state using diet-induced obese mice and mice homozygous null for leptin, an adipokine that regulates appetite.[8] Filomicelles were chosen as model nanoparticles because of their PEG brush, long circulation times, and their effectiveness in targeting and shrinking tumor xenographs in mice.[5, 17] With these properties, I propose that this system be considered as an effective baseline to quantify general nanoparticle biodistribution as a function of patient metabolic state. Chemical and physical modifications that model the properties of specialized nanoparticles of interest can be easily made.[18]

To provide broad insight into the effects of diet and weight on nanoparticle biodistribution, I used four sets of mice ranging from lean (27 ± 1 g) to obese (60 ± 2 g). In lean mice, the liver, spleen, lungs, kidney, and heart showed NIR signals in decreasing order with the liver and spleen dominating as expected.[17] Surprisingly, when the weight of the mice was increased through a HFD leading to significant WAT mass, the NIR signal increased in WAT as a linear function of its mass. Even in mice with moderate weights (20% heavier than lean mice), the signal

of the combined WAT was comparable to that of the spleen. In ob/ob mice, the combined NIR intensity of the WAT was more than twice that of the spleen. These results show that obesity can have a profound influence on the biodistribution of bio-compatible circulating nanoparticles.

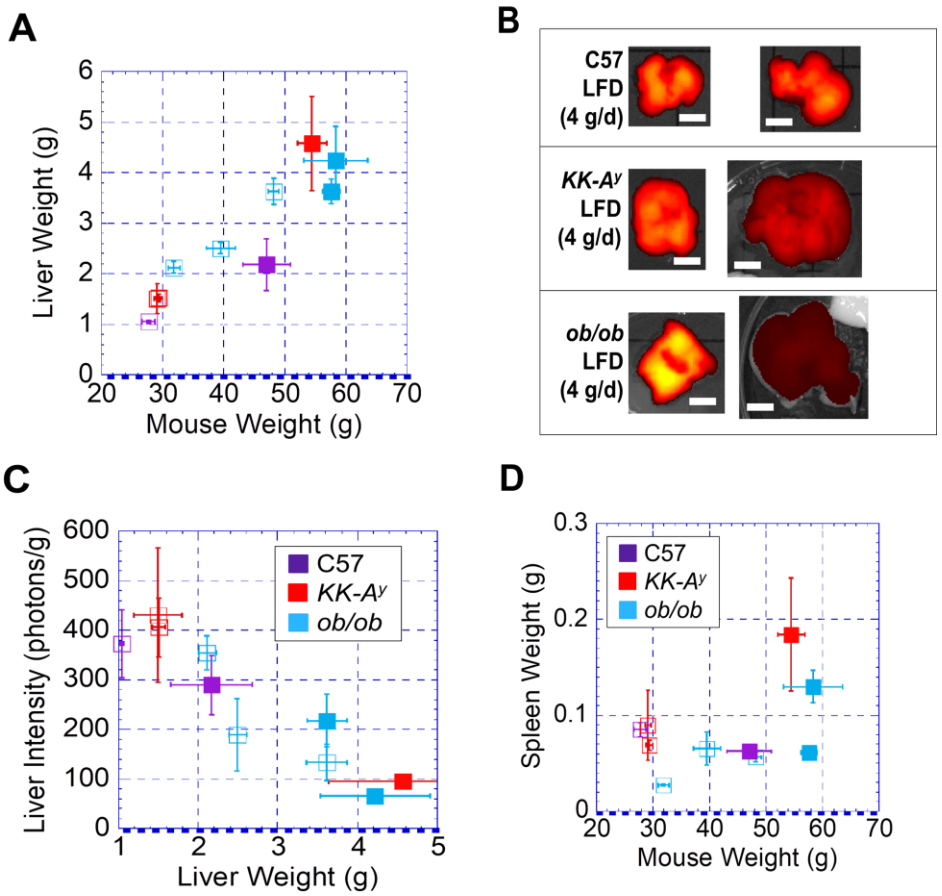


Figure 3.1. Biodistribution of filomicelles in mice as a function of diet, weight, and genetics. (A) Plot of the weights of mouse livers as a function of mouse weight at the time of injection of filomicelles carrying NIR dye (filomicelles-NIR). Open symbols represent mice that were fed a low fat diet (LFD). Closed symbols represent mice that were fed a high fat diet (HFD). Mice that are represented by the open symbols in the box were restricted to 4 g/d of LFD. (B) Fluorescent images of livers from the mice that were injected with filomicelles-NIR. (C) Fluorescent intensity of the livers shown in (B). Each data point represents three livers. (D) Plot of the weights of mouse spleens as a function of mouse weight at the time of injection of filomicelles-NIR. Scale bars are 10 mm.

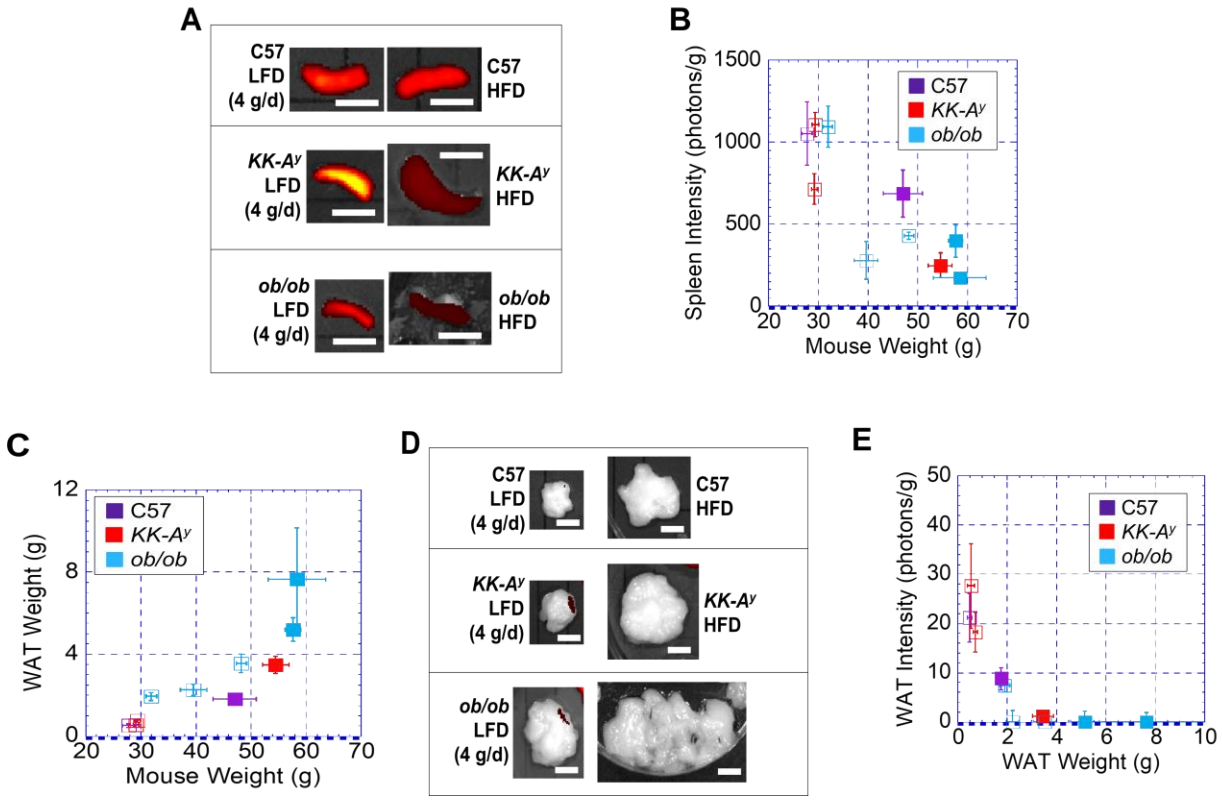


Figure 3.2 (A) Fluorescent images of spleens from the mice that were injected with filomicelles-NIR. (B) Fluorescent intensity of the spleens shown in (A). Each data point represents three spleens. (C) Plot of the weights of mouse WAT as a function of mouse weight at the time of injection of filomicelles-NIR. (D) Fluorescent images of the WAT from the mice that were injected with filomicelles-NIR. (E) Fluorescent intensity of the WAT shown in (D). Each data point represents the WAT from three separate mice. Scale bars are 10 mm.

References

1. Simon, L. C.; Sabliov, C. M., The effect of nanoparticle properties, detection method, delivery route and animal model on poly(lactic-co-glycolic) acid nanoparticles biodistribution in mice and rats. *Drug Metabolism Reviews* **2013,** *46* (2), 128-141.
2. Dawidczyk, C. M.; Kim, C.; Park, J. H.; Russell, L. M.; Lee, K. H.; Pomper, M. G.; Searson, P. C., State-of-the-art in design rules for drug delivery platforms: Lessons learned from FDA-approved nanomedicines. *Journal of Controlled Release* **2014,** *187*, 133-144.
3. Prado, C. M.; Baracos, V. E.; Xiao, J.; Birdsell, L.; Stuyckens, K.; Park, Y. C.; Parekh, T.; Sawyer, M. B., The association between body composition and toxicities from the combination of Doxil and trabectedin in patients with advanced relapsed ovarian cancer. *Applied Physiology, Nutrition, and Metabolism* **2014,** *39* (6), 693-698.
4. Hillmyer, M. A.; Bates, F. S., Synthesis and characterization of model polyalkane– poly (ethylene oxide) block copolymers. *Macromolecules* **1996,** *29* (22), 6994-7002.
5. Geng, Y.; Dalhaimer, P.; Cai, S.; Tsai, R.; Tewari, M.; Minko, T.; Discher, D. E., Shape effects of filaments versus spherical particles in flow and drug delivery. *Nature Nanotechnology* **2007,** *2*, 249-255.
6. Kersey, F. R.; Merkel, T. J.; Perry, J. L.; Napier, M. E.; DeSimone, J. M., Effect of aspect ratio and deformability on nanoparticle extravasation through nanopores. *Langmuir* **2012,** *28*, 8773-8781.
7. Iwatsuka, H.; Shino, A.; Suzuoki, Z., General survey of diabetic features of yellow KK mice. *Endocrinol Jpn* **1970,** *17*, 23-25.
8. Coll, A. P.; Farooqi, I. S.; O'Rahilly, S., The hormonal control of food intake. *Cell* **2007,** *129*, 251-252.
9. Gordon, S.; Taylor, P. R., Monocyte and macrophage heterogeneity. *Nature Reviews Immunology* **2005,** *5*, 953-964.
10. Odegaard, J. I.; Ricardo-Gonzalez, R. R.; Goforth, M. H.; Morel, C. R.; Subramanian, V.; Mukundan, L.; Red Eagle, A.; Vats, D.; Brombacher, F.; Ferrante, A. W.; Chawla, A., Macrophage-specific PPARgamma controls alternative activation and improves insulin signaling in adipose tissue. *Nature* **2007,** *448*, 1116-1120.
11. Kratz, M.; Coats, B. R.; Hisert, K. B.; Hagman, D.; Mutskov, V.; Peris, E.; Schoenfelt, K.; Kuzma, J. N.; Larson, I.; Billing, P. S.; Landerholm, R. W.; Crouthamel, M.; Gozal, D.; Hwang, S.; Singh, P. K.; Becker, L., Metabolic dysfunction drives a mechanistically distinct proinflammatory phenotype in adipose tissue macrophages. *Cell Metabolism* **2014,** *20*, 614-625.
12. Xu, X.; Grijalva, A.; Skowronski, A.; van Eijk, M.; Serlie, M. J.; Farrante, A. W., Obesity activates a program of lysosomal-dependent lipid metabolism in adipose tissue macrophages independently of classic activation. *Cell Metabolism* **2013,** *18*, 816-830.
13. Morris, D. L.; Cho, K. W.; Delproposto, J. L.; Oatmen, K. E.; Geletka, L. M.; Martinez-Santibanez, G.; Singer, K.; Lumeng, C. N., Adipose tissue macrophages function as antigen-presenting cells and regulate adipose tissue CD4(+) T cells in mice. *Diabetes* **2013,** *62*, 2762-2772.
14. Hossen, M. N.; Kajimoto, K.; Akita, H.; Hyodo, M.; Harashima, H., Vascular-targeted nanotherapy for obesity: unexpected passive targeting mechanism to obese fat for the enhancement of active drug delivery. *Journal of Controlled Release* **2013,** *163*, 101-110.

15. Hossen, M. N.; Kajimoto, K.; Akita, H.; Hyodo, M.; Harashima, H., A comparative study between nanoparticle-targeted therapeutics and bioconjugates as obesity medication. *Journal of Controlled Release* **2012,** *171*, 104-112.
16. Hossen, M. N.; Kajimoto, K.; Akita, H.; Hyodo, M.; Ishitsuka, T.; Harashima, H., Ligand-based targeted delivery of a peptide modified nanocarrier to endothelial cells in adipose tissue. *Journal of Controlled Release* **2010,** *147*, 261-268.
17. Christian, D. A.; Cai, S.; Garbuzenko, O. B.; Harada, T.; Zajac, A. L.; Minko, T.; Discher, D. E., Flexible Filaments for in vivo Imaging and Delivery: Persistent Circulation of Filomicelles Opens the Dosage Window for Sustained Tumor Shrinkage. *Molecular Pharmaceutics* **2009,** *6* (5), 1343-1352.
18. Dalhaimer, P., Engler, A. J., Parthasarathy, R., Bates, F. S., Discher, D. E, Targeted worm micelles. *Biomacromolecules* **2004,** *5*, 1714-1719.

CHAPTER IV

Incorporation of Obesity and B-cell Lymphoma in a Mouse Model

4.1 Abstract

Our novel crossing of Eμ-*myc* and ob/ob, done with the help of Sarah Kauffman, provided useful for understanding some of the effects of diet-induced obesity on the proliferative nature of B-cell malignancies. We show here that diet has the capability of causing significant changes to lymph node and splenic architecture. High fat-diet consumption for prolonged periods was shown to cause lymphoid hyperplasia cholesterol granuloma and foamy macrophages in lymph nodes of ob/ob mice. When ob/ob mice were placed on a high-fat diet and administered paclitaxel, there was still an identification of marked follicular lymphoid hyperplasia in their spleens. This is particularly interesting since paclitaxel is generally known to reduce lymphocyte numbers. Male ob/OB x Eμ-*myc* that were fed a high-fat diet also had a worse diagnosis than their female counterparts that were fed a low-fat diet. Altogether, our studies point to the potential of obesity status to influence B-cell lymphoma.

4.2 Introduction

Non-Hodgkin's lymphoma (NHL) constitutes a heterogenous group of lymphoproliferative malignancies with approximately 85% arising from B-cell lymphocytes while the remainder are derived from T-cells and natural killer cells.[1] These malignant lymphomas generally emerge from cancerous lymphocytes in the lymph nodes but can develop anywhere lymph tissues are found in the body.[1] Based on histopathological features, the lymphomas can be broadly categorized as indolent or aggressive. Indolent lymphomas are usually incurable and tend to less responsive to each successive treatment of chemotherapy over the history of the disease.[2] On the other hand, aggressive lymphomas are typically characterized by a rapid symptom onset and if the disease is left untreated, death could occur fairly quickly although most cases of aggressive lymphoma can be cured if chemotherapy is initiated in a timely manner.[2]

Treatment of NHL can often be complicated by the presence of underlying conditions[3-5] and understanding the impact of such comorbidities on lymphoma therapy is important in determining potential preventive regimens and therapeutic strategies. Obesity, in particular, is one of such conditions that is highly prevalent in the United States and most of the Western world;[6] therefore, it is possible that overweight and obese patients would often be encountered for lymphoma treatment. Although obesity is a well-known risk factor for developing NHL,[7-8] there is scant knowledge about the impact of obesity on the aggressiveness or overall survival in lymphoma cases. Most studies in literature are non-experimental epidemiological studies and their results are conflicting.[9-16] Some researchers found a positive association between overweight or obese patients and survival while others found a deleterious association or none at all.

Body mass index (BMI) was used in these epidemiological studies as a measure of body fat and patients were stratified into various groups depending on their BMI. Since there were no quantifiable indicators for obesity-related disease aggressiveness, overall survival was considered as an alternate measure for the impact of obesity in the NHL cases. In summary, diffuse large B-cell lymphoma (DLBCL) was the predominant aggressive NHL subtype examined and obesity-related impact on overall survival was inconclusive since these studies lacked a consistent objective grouping measure for body fat, and other influential factors such as established NHL treatment regimens or age, gender and people groups were not comparable across all studies. Although the non-experimental epidemiological studies were inconclusive, the results do show that obesity is an important factor that needs to be considered in the treatment and survival of lymphoma patients. To this end, experimental studies (e.g. animal models of B-cell lymphoma and obesity) that demonstrate how obesity affects NHL prognosis will be essential.

While there is limited experimental information on how obesity impacts NHL, a couple studies provide some insight as to the relevance of body fat in NHL cases. Huang and coworkers utilized C57BL6/J and peroxisome proliferator-activated receptor-α deficient (PPAR-α -/-) mice bearing B-cell tumors induced by Bcr/Abl-transformed B-cells to study the effect of tumor development on lipid mobilization and distribution.[17] They found that it could be possible for the B-cell tumors to elicit lipid mobilization from white adipose tissue to the liver, with subsequent increased export of serum lipids in the form of very low density lipoprotein (VLDL)/low density lipoprotein (LDL) to further promote tumor growth. Results of their investigations also showed that fenofibrate, a lipid-lowering drug and PPAR-α agonist, altered hepatic lipid metabolism and suppressed tumor growth. In a different study by the same group, they used VLDL production-deficient mice, carboxylesterase 3/triacylglycerol hydrolase -/- (Ces3/Tgh -/-), to further elucidate the mechanism by which tumor progression was dependent on tumor-induced hyperlipidemia.[18] They discovered that Ces3/Tgh -/- mice were resistant to tumor-induced hepatic LDL receptor (LDLR) downregulation and hyperlipidemia which resulted in significantly diminished growth of Bcr/Abl-transformed B-cell tumors.

Other researchers' works have also pointed to the potential for altered lipid metabolism to impact B-cell lymphoma growth,[19-21] however, more studies need to be done to further assess the impact of body fat or obesity on B-cell lymphoma cases. In light of our current limited knowledge of B-cell lymphoma metabolism, we proposed to incorporate obesity and B-cell lymphoma in a single mouse model to better understand the effects of obesity on the growth of B-cell tumors and ultimately overall survival.

4.3 Materials and Methods

All animal experiments were conducted using institutionally approved protocols by the Institutional Animal Care and Use Committee (IACUC) at the University of Tennessee, Knoxville. Veterinarians (MMF & KN) at the University of Tennessee, Knoxville were blinded for all submitted samples.

4.3.1 Breeding and Injections

Heterozygous obese (ob/OB; stock# 000632, JAX Laboratory, United States) female mice were bred with male mice that develop B-cell lymphomas (OB/OB B6.Cg-Tg(IghMyc)22Bri/J; stock# 00278, JAX Laboratory, United States). Mice with the desired genotypes were separated into two groups; one given a high-fat diet (D12492, Research Diets, Inc., United States) to induce obesity and another on a low-fat diet (D12450B, Research Diets, Inc., United States) to serve as a control. After confirmation of obese or B-cell lymphoma status, mice were intravenously administered either 100 µl 1X PBS or 5 mg/kg paclitaxel (PTX) drug five to six days before blood collection.

4.3.2 PCR Screening for Mice Genotype – Lep^{Ob}

Mouse tail snips were performed, and genomic DNA extractions were carried out according to manufacturer's protocol using DirectAmp tissue genomic DNA amplification kit (Denville Scientific, United States). The following stock primers were used as recommended by JAX Laboratory for Lep^{ob}: oIMR1151 common,5'-TGT CCA AGA TGG ACC AGA CTC-3'; and oIMR1152 common, 5'-ACT GGT CTG AGG CAG GGA GCA-3'. Stock primers were diluted to 100 pmoles/µl and a fresh primer mix was made by diluting all primers to 10 pmoles/µl. The recipe for PCR amplification consisted of 4 µl of DNA extract, 1 µl of primer mix, 10 µl of Hot-Start Taq mastermix (Denville

Scientific, United States) and 5 µl of water. PCR was carried out with an Eppendorf Mastercycler X50a (Eppendorf, Germany) under the following cycling conditions: 94°C for 3 min, (94°C for 30 s, 62°C for 1 min, 72°C for 45 s) 35 cycles, 72°C for 2 min and hold at 4°C. Following the PCR run, the PCR products were digested with Thermo Scientific FastDigest DdeI (HPyF3I) restriction enzyme kit. Digested products were separated on a 3% agarose gel. Products that were wild-type, heterozygous, and mutant had the following band sizes: 155 bp; 155 bp, 100 bp and 55 bp; and 55 bp respectively.

4.3.3 PCR Screening for Mice Genotype – Eµ-*myc*

Genomic DNA extractions from mouse tails were done with the same kit as above. The same concentrations for stock primers and primer mixes were also used. The following stock primers were utilized as recommended by JAX Laboratory: 14377 transgene forward, 5'-TTA GAC GTC AGG TGG CAC TT-3'; 14378 transgene reverse, 5'-TGA GCA AAA ACA GGA AGG CA-3'; oIMR7338 internal positive control forward, 5'-CTA GGC CAC AGA ATT GAA AGA TCT-3'; and oIMR7339 internal positive control reverse 5'-GTA GGT GGA AAT TCT AGC ATC ATC C-3'. The PCR recipe is as follows: 4 µl of DNA extract, 0.7 µl of primer mix, 10 µl of Hot-Start Taq mastermix and 5.3 µl of water. PCR amplification was carried out with an Eppendorf Mastercycler X50a using the following cycling conditions: 94°C for 4 min, (94°C for 20 s, 65°C for 20 s, 68°C for 25 s) 10 cycles, (94°C for 20 s, 60°C for 20 s, 72°C for 20 s) 28 cycles, 72°C for 2 min and hold at 4°C. PCR Products were separated on a 3% agarose gel with 210 bp and 324 bp corresponding to the transgene and the internal positive control respectively.

4.3.4 Blood Collection

All mice were anaesthetized with isoflurane (Zoetis Inc., Kalamazoo, MI) using the open-drop method prior to blood collection. Whole blood was collected from each mouse via jugular vein puncture with a 20G needle. Blood was collected and placed in a dipotassium ethylenediaminetetraacetic acid (K_2EDTA) tube (BD Microtainer, Becton, Dickinson and Company, Franklin Lakes, NJ), followed by tube inversion several times to mix the blood. All samples were kept at 4°C prior to hematology analysis to be performed within 24 hours.

4.3.5 Hematology

A complete blood count (CBC) was performed using an automated hematology analyzer (Vet abc, Scil Animal Care, Gurnee, IL). Additionally, a blood smear was prepared and stained (Aerospray 7120, Wescor, Logan, UT) using routine clinical laboratory methods, and reviewed by a board-certified veterinary clinical pathologist (MMF).

4.3.6 Tissue Fixation and Evaluation

At necropsy, the tissues were collected, fixed in 10% neutral buffered formalin. After 24 hours of fixation, the tissues underwent routine processing, paraffin-embedding, sectioning, hematoxylin and eosin staining, and microscopic evaluation by a board-certified veterinary pathologist (KN).

4.4 Results and Discussion

Mice were injected according to the schedule in Table 4.1 after confirmation of obesity and/or B-cell lymphoma status (Appendix C.1). Their corresponding weights can also be seen in Table 4.2. Samples for blood collection revealed that mice that were found to have the Eμ-*myc* transgene, as determined by PCR genotyping, also had increased white blood cell count when compared on average to the rest of the non-transgenic mice

(Table 4.3 and Figure 4.1). Cell volume and morphology from healthy and Eμ-*myc* transgenic mice also provided more evidence of hematologic malignancy. Micrographs of blood smear samples from non-transgenic and Eμ-*myc* transgenic mice illustrated that mice with the transgene exhibited larger cells than those from non-transgenic mice, which is consistent with identification of malignant c-*myc* lymphocytes (Figure 4.2).[22] Mice with the Eμ-*myc* transgene (PD5, C35, C6; Table 4.1, Figure 4.2) were categorized as having lymphoid leukemia or stage V lymphoma based on the hematology results.

These findings were also confirmed from a histological examination of spleen and lymph node tissue samples (Table 4.4, Figure 4.3 – 4.5). We can see from Figure 4.5 that the lymph node tumor of the ob/OB x Eμ-*myc* male (C35) mouse did not have any remaining lymph node architecture; furthermore, cells were extending beyond the lymph node capsule. Cells going beyond the lymph node capsule would indicate that the disease could metastasize.[23-24] In Figure 4.5C we also clearly see the presence of monomorphic populations of large lymphocytes and frequent mitosis occurring. Frequent clusters of apoptotic cells were also observed. All of this indicates a rapid proliferation and death of cells which are characteristic of cancerous cell populations.[25-26]

Diagnosis of the spleen (C35) indicated marked follicular lymphoid hyperplasia (MFLH) and extramedullary hematopoiesis (MEMH). Follicular hyperplasia is a typical cause of lymph node enlargement mainly due to an increase in the number of B-cells that become larger and proliferate rapidly.[27] However, follicular hyperplasia diagnosis can be benign as opposed to follicular lymphoma which is a common malignant NHL.[28] MEMH may indicate an infiltration of neoplastic cells,[29] as seen by the large spleen (Table 4.5), and it could also signify a steady supply of monocytes to the tumor site.[30] However, EMH on its own as an assessment of lymphoma pathologies by extramedullary hematopoiesis can be rather obscure and has often been relegated as an epiphenomenon.[31] Therefore, a complete evaluation of other potential factors as we have determined, is necessary

for a clear diagnosis. Altogether, the data and diagnosis are in sync and undoubtedly identify B-cell lymphoma in ob/OB x Eμ-*myc* mice.

Comparing the ob/OB x Eμ-*myc* female (C36) mouse that displayed mild follicular lymphoid hyperplasia (MIFLH) with the male mouse (C35) that was diagnosed with MFLH in the spleen, we see that apart from gender differences, the other main factor that distinguishes the two are their diets. The female was fed a low-fat diet while the male was fed a high-fat diet, which may account for differences in their diagnosis. When the ob/OB x Eμ-*myc* female is compared to her ob/OB (C38) counterpart, their diagnosis for follicular lymphoid hyperplasia is similar but EMH for ob/OB (C38) was considered mild. The identification of MFLH in spleen was also determined for all mice fed a high-fat diet regardless of gender, weight or differences in obesity and Eμ-*myc* status. This agrees with other research studies that have shown an increase in splenic hyperplasia as a result of consuming high-fat diets.[32-35]

Lymphoid cholesterol granuloma in the lymph nodes of female ob/ob (C28 and C29) mice is indicative of their obesity status and intake of high-fat diets. These mice were placed on a high-fat diet for 8 weeks and had an average weight of about 60 g. The presence of foamy macrophages in the lymph node (Figure 4.4) is also a prominent feature of these cells that can result from consuming diets high in fat.[36-37] In the lymph node of this female ob/ob (C28) mouse, even though there was MFLH, the lymph node architecture was retained as opposed to a distortion of lymph node architecture in the male ob/OB x Eμ-*myc* mouse (C35). Germinal centers in the lymph node of the female ob/ob (C28) mouse also displayed larger B-cells with smaller surrounding lymphocytes, but with rare mitotic and apoptotic cell events. The spleen of ob/ob female mouse (Figure 4.3) showed an expansion of periarteriolar lymphoid sheath from lymphocyte hyperplasia and the red pulp displayed EMH. This is interesting since this mouse (C28) was injected with PTX which is well-known to deplete lymphocyte numbers in

tissues and has been found by researchers to cause mouse splenic lymphocytes to be hyporesponsive.[38-40] However, there could be lymphocyte repopulation following paclitaxel therapy (i.e. after gaps in treatment) potentially due to B-cell diversity and/or a recovering immune system.[41-42] Although the exact mechanisms are unclear, the combined treatments of high-fat diet and 5 mg/kg PTX induced lymphoid hyperplasia in ob/ob female mouse. The identification of EMH could also be as a result of PTX and/or a high-fat diet since EMH is a known occurrence following administration paclitaxel and other chemotherapeutic agents.[43-44]

The combined results from our tests should aid in guiding future experiments. One of the major areas to explore would be an introduction of flow cytometry methods that can differentiate between B-cell subpopulations since the automated WBC count makes no distinction between normal and malignant populations. This would also help in resolving subpopulations that are like to be hyporeactive (or hyperactive) after treatment with any chemotherapeutic drugs.

4.5 Conclusion

Overall, our findings demonstrate that there is the potential for obesity status and/or a diet high in fat to influence disease progression in B-cell malignancies. We propose that for a more definitive assessment of B-cell lymphoma pathologies, more tests would need to be incorporated to elucidate the mechanisms surrounding the relationship between obesity status and/or a high-fat diet on B-cell lymphoma.

Table 4.1 Experimental Outline of Injection Schedule, Blood Collection and Diet Placement

Sample ID	Gender	Genotype	**Time of Diet Placement / duration	Injection	Blood collection (BC)
PD1 – PD3	M	ob/ob Tg-	HFD, 15 wks post DOB / 3 wks	--	3 wks post HFD placement
PD4	F	ob/ob Tg-	HFD, 15 wks post DOB / 3 wks	--	3 wks post HFD placement
PD5*	M	ob/ob Tg+	HFD, 16 wks post DOB / 3 wks	--	3 wks post HFD placement
C1, C2	M	OB/OB Tg-	HFD, 12 wks post DOB / 9.5 wks	Pbs/ 5 days pr.BC	9.5 wks post HFD placement
C3, C4*	F	OB/OB Tg-	HFD, 12 wks, 14 wks post DOB / 9.5 wks	Pbs/ 5 days pr.BC	9.5 wks post HFD placement
C5, C6	M	OB/OB Tg-	HFD, 12 wks post DOB / 10.5 wks	Pbs/ 5 days pr.BC	10.5 wks post HFD placement
C7, C8*	F	OB/OB Tg-	HFD, 12 wks, 14 wks post DOB / 10.5 wks	Pbs/ 5 days pr.BC	10.5 wks post HFD placement
C9, C10	M	OB/OB Tg-	HFD, 12 wks post DOB / 11.5 wks	Pbs/ 5 days pr.BC	11.5 wks post HFD placement
C11	F	OB/OB Tg-	HFD, 12 wks post DOB / 11.5 wks	Pbs/ 5 days pr.BC	11.5 wks post HFD placement
C12, C13	M	OB/OB Tg-	HFD, 12 wks post DOB / 12.5 wks	Pbs/ 6 days pr. BC	12.5 wks post HFD placement
C14	F	OB/OB Tg-	HFD, 12 wks post DOB / 12.5 wks	Pbs/ 6 days pr. BC	12.5 wks post HFD placement
C16	F	ob/ob Tg-	HFD, 17 wks post DOB / 5 wks	PTX/ 5 days pr.BC	5 wks post HFD placement
C17, C18	F	ob/ob Tg-	HFD, 16.5 wks post DOB / 5 wks	PTX/ 5 days pr.BC	5 wks post HFD placement
C19*	F	ob/ob Tg-	HFD, 12 wks post DOB / 5 wks	PTX/ 5 days pr.BC	5 wks post HFD placement
C20	F	ob/ob Tg-	HFD, 17 wks post DOB / 5 wks	PTX/ 5 days pr.BC	5 wks post HFD placement
C22	F	ob/ob Tg-	HFD, 17 wks post DOB / 7 wks	PTX/ 5 days pr. BC	7 wks post HFD placement

Table 4.1 (continued)

Sample ID	Gender	Genotype	**Time of Diet Placement / duration	Injection	Blood collection (BC)
C23, C24	F	ob/ob Tg-	HFD, 16.5 wks post DOB / 7 wks	PTX/ 5 days pr.BC	7 wks post HFD placement
C25*	F	ob/ob Tg-	HFD, 12 wks post DOB / 7 wks	PTX/ 5 days pr.BC	7 wks post HFD placement
C27	F	ob/ob Tg-	HFD, 17 wks post DOB / 8 wks	PTX/ 5 days pr.BC	8 wks post HFD placement
C28, C29	F	ob/ob Tg-	HFD, 16.5 wks post DOB / 8 wks	PTX/ 5 days pr.BC	8 wks post HFD placement
C30*	F	ob/ob Tg-	HFD, 12 wks post DOB / 8 wks	PTX/ 5 days pr.BC	8 wks post HFD placement
C35*	M	ob/OB Tg+	HFD, 14 wks post DOB/ 2 wks	--	2 wks post HFD placement
C36*	F	ob/OB Tg+	LFD, throughout lifespan	--	15 wks post DOB
C37*	M	ob/OB Tg-	HFD, 10 wks post DOB/ 2 wks	--	2 wks post HFD placement
C38*	F	ob/OB Tg-	LFD, throughout lifespan	--	15 wks post DOB

ob/ob, homozygous knockout for leptin; OB/OB, wild-type; ob/OB, heterozygous for leptin;
Tg, B6.Cg-Tg(IghMyc)22Bri/J; Tg+, positive for transgene; Tg-, negative for transgene; pr.BC, prior to blood collection;
HFD, high fat diet; LFD, low fat diet; DOB, date of birth
*Differences in timing due to mice DOB
** Mice that were placed on HFD were on LFD prior to diet change
PD1 - PD5 (same BC group); C1 - C14 (same BC group); C16 - C30 (same BC group); C35 - C38 (same BC group). a1: PD1 (1 distinct M), a2: PD2 (1 distinct M), a3: PD3 (1 distinct M), a4: PD4 (1 distinct F), a5: PD5* (1 distinct M) [a1 to a4 born ~5 days after a5]; a6: C1, C5, C9, C12 (1 distinct M for 4 BCs), a7: C2, C6, C10, C13 (1 distinct M for 4 BCs), a8: C3, C7, C11, C14 (1 distinct F for 4 BCs), a9: C4, C8 (1 distinct F for 2 BCs) [a9 born ~3wks before other groups]; a10: C16, C22, C27 (1 distinct F for 3 BCs), a11: C17, C23, C28 (1 distinct F for 3 BCs), a12: C18, C24, C29 (1 distinct F for 3 BC), a13: C19, C25, C30 (1 distinct F for 3 BCs), a14: C20 (1 F for BC) [a10 is the oldest. a11 & a12 are 6 days younger than a10. a14 is 5 wks younger than a10 and ~4.5 wks younger than a11 & a12]; a15: C35 (1 M for 1 BC), a16: C36 (1 F for 1 BC), a17: C37 (1 M for 1 BC), a18: C38 (1 F for 1 BC) [a15 is the oldest. a16 & a18 are 1 wk younger than a15. a17 is 4 wks younger than a15]

Table 4.2 Weight of Mice During Experiments*

Sample ID	Weight (g)	Sample ID	Weight (g)
PD1, M	50.80	C16, F	58.82
PD2, M	56.36	C17, F	54.93
PD3, M	53.62	C18, F	54.60
PD4, F	50.60	C19, F	54.25
PD5, M	44.85	C20, F	60.30
C1, M	38.54	C22, F	62.20
C2, M	41.08	C23, F	59.70
C3, F	24.45	C24, F	58.15
C4, F	34.26	C25, F	58.94
C5, M	37.89	C27, F	63.27
C6, M	40.53	C28, F	61.78
C7, F	24.15	C29, F	58.63
C8, F	33.47	C30, F	60.49
C9, M	37.86	C35, M	21.81
C10, M	41.70	C36, F	18.53
C11, F	24.48	C37, M	28.68
C12, M	38.40	C38, F	20.86
C13, M	41.80	--	--
C14, F	24.50	--	--

*Reference to Table 4.1 for details on injection, blood collection and diet placement. M – male, F- female.

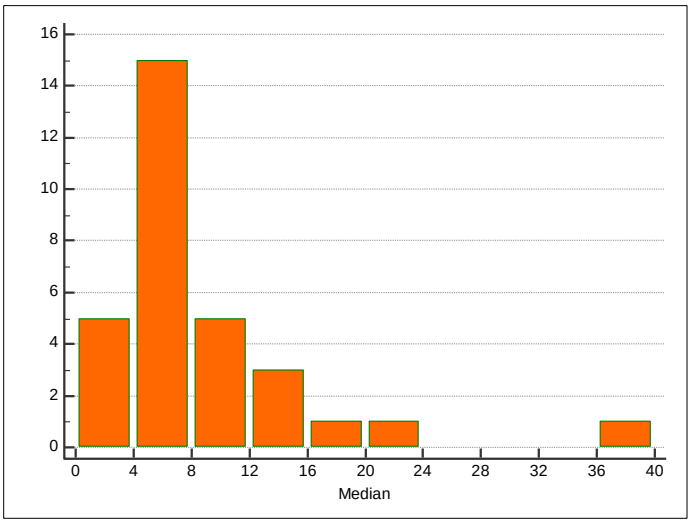


Figure 4.1 White Blood Count Frequency Distribution

Table 4.3 White Blood Cell Count from Blood of Eμ-*myc* Transgenic and Normal Mice

	WBC ($x10^3/\mu L$)				
Sample ID	Run 1	Run 2	Run 3	Mean	Median
PD1, M	8.8	8.7	8.0	8.5	8.7
PD2, M	2.3	5.0	5.0	4.1	5.0
PD3, M	6.2	6.2	6.5	6.3	6.2
PD4, F	5.1	5.2	5.2	5.2	5.2
PD5, M	20.5	20.0	19.7	20.1	20.0
C1, M	3.1	6.1	3.1	4.1	3.1
C2, M	7.1	7.2	7.1	7.1	7.1
C3, F	4.2	4.2	3.8	4.1	4.2
C4, F	4.2	4.2	4.2	4.2	4.2
C5, M	8.3	8.2	7.8	8.1	8.2
C6, M	8.2	9.0	9.2	8.8	9.0
C7, F	5.1	4.7	4.9	4.9	4.9
C8, F	5.6	5.4	5.8	5.6	5.6
C9, M	4.8	4.7	4.7	4.7	4.7
C10, M	4.7	4.4	4.0	4.4	4.4
C11, F	3.2	3.0	3.3	3.2	3.2
C12, M	6.1	5.5	5.6	5.7	5.6
C13, M	6.1	6.2	6.3	6.2	6.2
C14, F	3.9	4.1	3.8	3.9	3.9
C22, F	11.5	11.6	11.8	11.6	11.6
C23, F	6.4	5.5	6.2	6.0	6.2
C24, F	12.8	12.4	12.1	12.4	12.4
C25, F	14.7	13.7	14.7	14.4	14.7
C27, F	7.4	7.2	7.1	7.2	7.2
C28, F	2.1	2.3	2.2	2.2	2.2
C29, F	12.2	11.2	12.0	11.8	12.0
C30, F	10.2	10.2	10.5	10.3	10.2
C35, M	32.6	38.1	37.1	35.9	37.1
C36, F	18.6	18.5	18.1	18.4	18.5
C37, M	3.9	3.7	3.8	3.8	3.8
C38, F	5.4	5.3	5.4	5.4	5.4

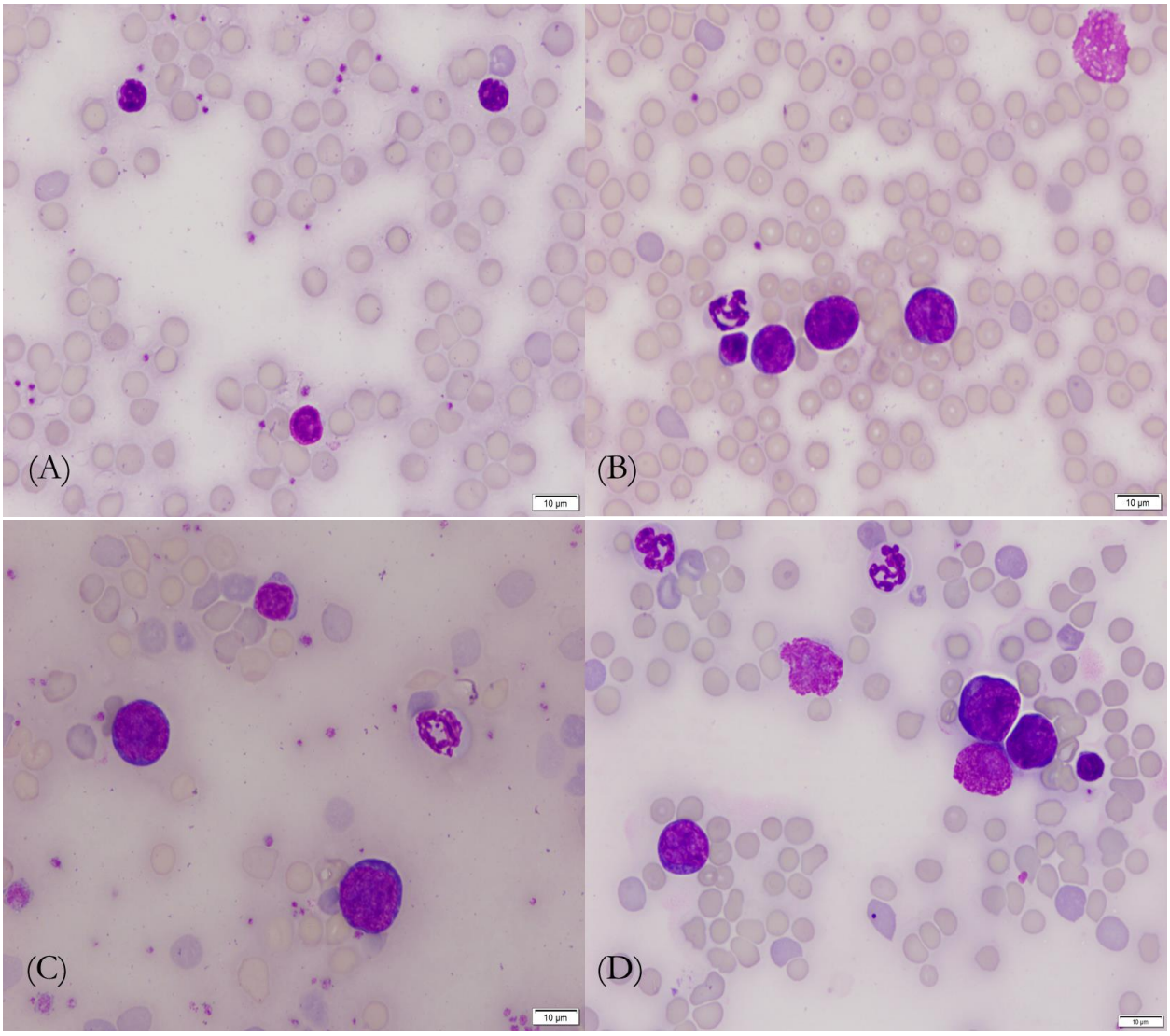


Figure 4.2 Blood smear showing morphology of granulocytes and lymphoblasts (60x). (A) C13 – showing no evidence of malignancy. (B) C35 – showing three large cells consistent with malignant lymphocytes; one small lymphocyte, likely benign; one neutrophil; one lysed cell. (C) C36 – Two large cells consistent with malignant lymphocytes; one small lymphocyte, likely benign; one neutrophil. (D) PD5 – Three large cells consistent with malignant lymphocytes; one small lymphocyte, likely benign; two neutrophils; two lysed cells.

Table 4.4 Histological Classification for Spleen and Lymph Node Tissues of Normal and Eμ-*myc* Mice

Sample ID	Tissue	Diagnosis
C12, M	Spleen	Marked follicular lymphoid hyperplasia
C13, M	Spleen	Marked follicular lymphoid hyperplasia
C14, F	Spleen	Marked follicular lymphoid hyperplasia
C27, F	Spleen	Marked follicular lymphoid hyperplasia & EMH
C28, F	Spleen	Marked follicular lymphoid hyperplasia & EMH
C28, F	Lymph node	Lymphoid hyperplasia cholesterol granuloma
C29, F	Spleen	Marked follicular lymphoid hyperplasia & EMH
C29, F	Lymph node (by pancreas)	Lymphoid hyperplasia cholesterol granuloma
C29, F	Lymph node (by salivary gland)	Lots of mast cells
C30, F	Spleen	Marked follicular lymphoid hyperplasia & EMH
C35, M	Spleen	Marked follicular lymphoid hyperplasia & EMH
C35, M	Lymph node (by pancreas)	Lots of histiocytes in peripancreatic lymph node
C35, M	Lymph node (by salivary gland)	Lymphosarcoma
C36, F	Spleen	Mild lymphoid hyperplasia & moderate EMH
C36, F	Skin with skeletal muscle	Lymphosarcoma
C37, M	Spleen	Marked follicular lymphoid hyperplasia
C38, F	Spleen	Mild lymphoid hyperplasia & EMH

EMH – extramedullary hematopoiesis

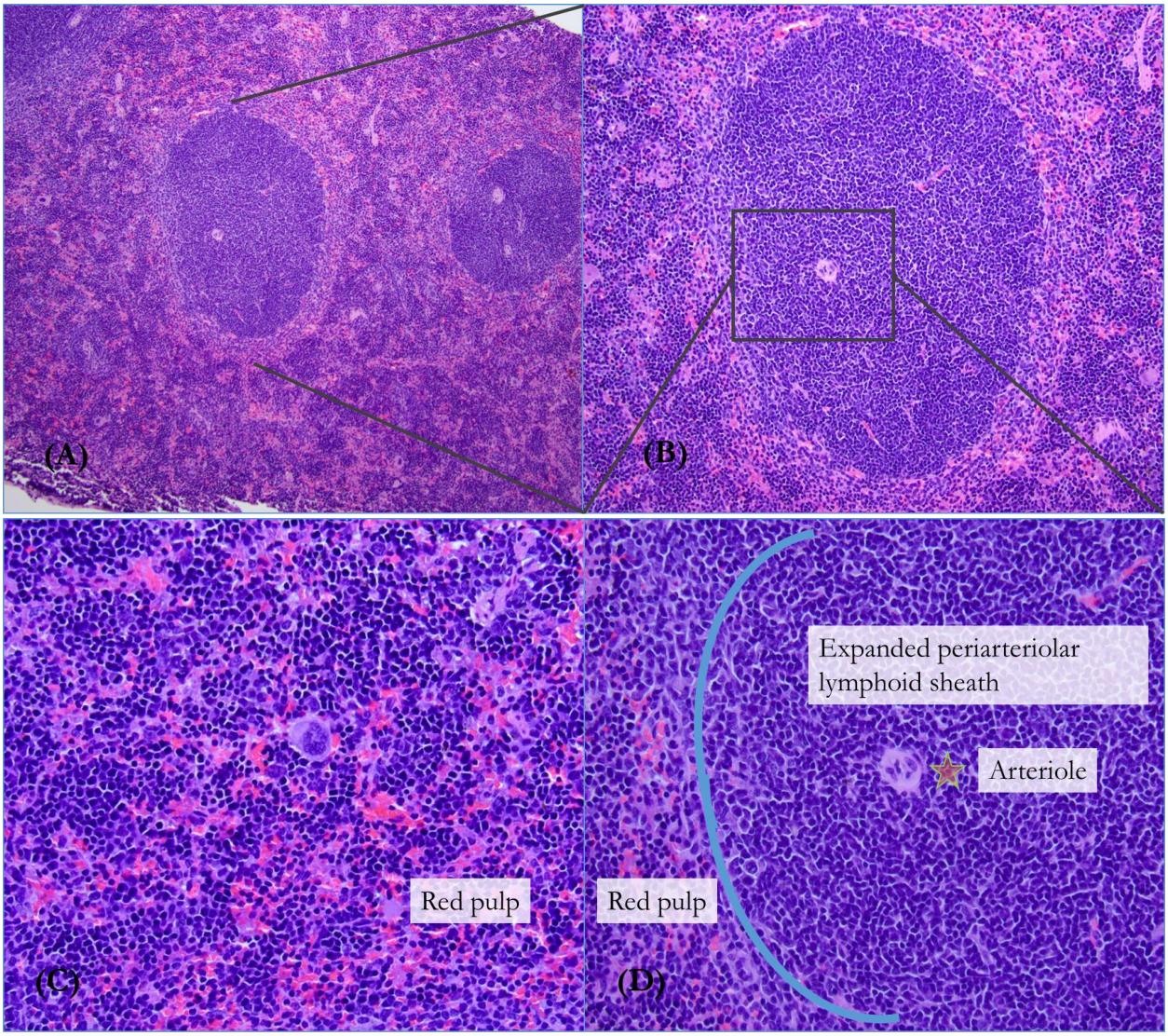


Figure 4.3 Spleen Histology of ob/ob Female (C28) Mice on a High Fat Diet for 8 weeks and following 3 Consecutive Week Injections of 5mg/kg PTX. (A) and (B) show the expansion of periarteriolar lymphoid sheaths, 100x and 200x respectively. (C) Extramedullary hematopoiesis in the red pulp (400x). (D) Enlarged view of the periarteriolar lymphoid sheath (400x). Left of the star in (D) is the arteriole

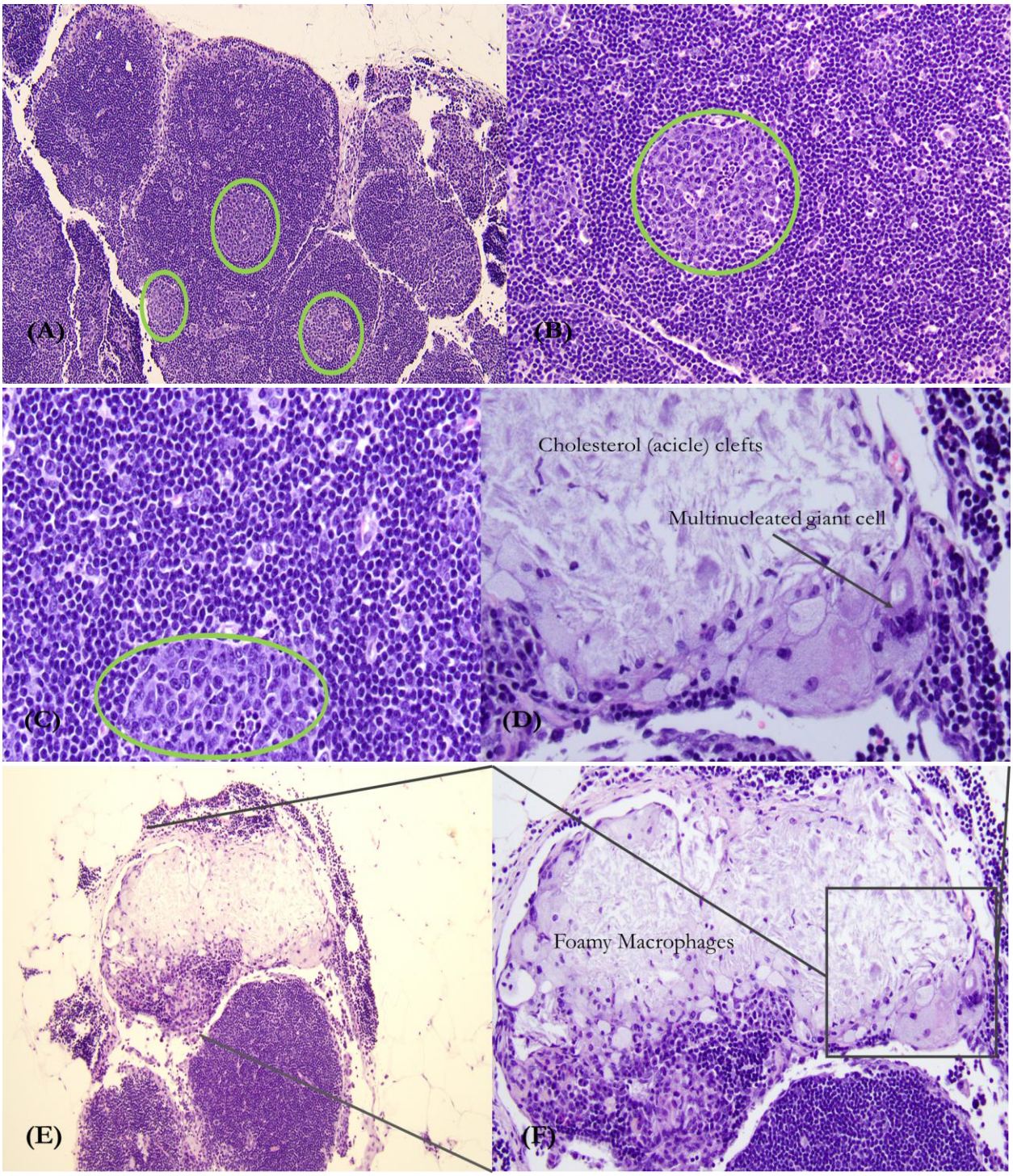


Figure 4.4 Histology of Lymph Node of ob/ob Female Mice (C28) on a High Fat Diet for 8 weeks and following 3 Consecutive Week Injections of 5mg/kg PTX. (A), (B) and (C) show the central germinal centers with larger cells surrounded by small lymphocytes. (D) Enlarged imaged from image [E] showing the cholesterol cleft and the formation of a multinucleated giant cell (400x). (E) Lymph node expanded by cholesterol granuloma (100x). (F) Displaying foamy macrophages (200x). Square box is for the enlarged image in [D].

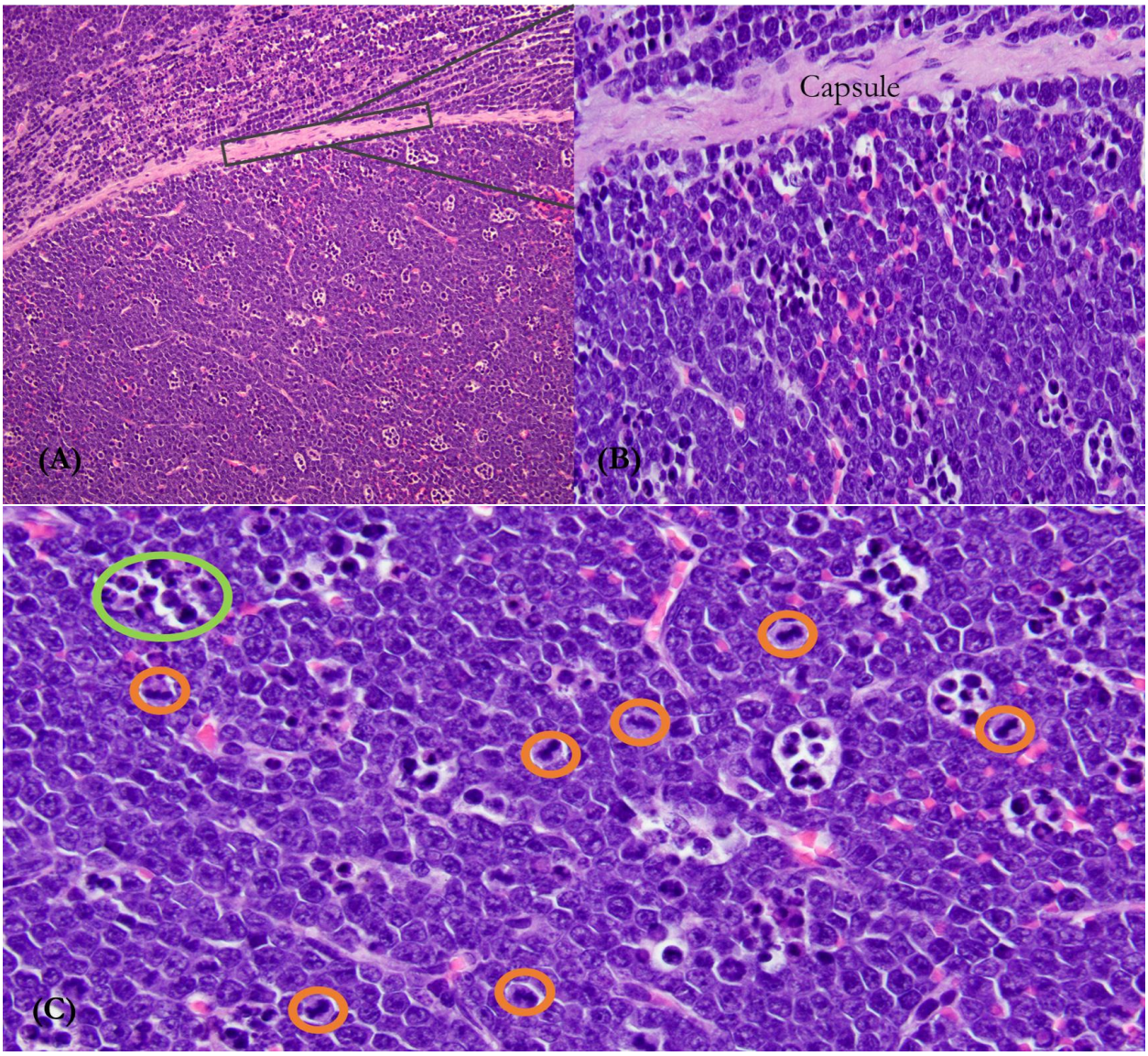


Figure 4.5 Histology of Lymph Nodes of Male (C35) ob/OB x Eμ-*myc* Mouse on a High Fat Diet for 2 weeks. (A) Showing no lymph node architecture and cells extending beyond the capsule (200x). (B) Enlarged image showing lymph node capsule (400x). (C) Monomorphic populations of large round cells with frequent mitoses (orange circle), and apoptotic cells often in clusters (green circle) (400x).

Table 4.5 Weights of Spleen and Lymph Node in C35-C38

Sample ID	Spleen Weight (mg)	Lymph Node (mg)
C35, M	249.7	664.8*, 504.7*,1051.2**
C36, F	322.2	671.0
C37, M	64.5	4.5
C38, F	60.6	5.0

*Lymph nodes by salivary gland, ** Lymph node by pancreas

References

1. Armitage, J. O.; Gascoyne, R. D.; Lunning, M. A.; Cavalli, F., Non-Hodgkin lymphoma. *Lancet* **2017,** *390* (10091), 298-310.
2. Al-Naeeb, A. B.; Ajithkumar, T.; Behan, S.; Hodson, D. J., Non-Hodgkin lymphoma. *BMJ* **2018,** *362*, k2304.
3. Janssen-Heijnen, M. L. G.; vanSpronsen, D. J.; Lemmens, V. E. P. P.; Houterman, S.; Verheij, K. D. G. W.; Coebergh, J. W. W., A population-based study of severity of comorbidity among patients with non-Hodgkin's lymphoma: prognostic impact independent of International Prognostic Index. *British Journal of Haematology* **2005,** *129*, 597-606.
4. Ip, A.; Switchenko, J. M.; Graiser, M.; Koff, J. L.; Gupta, V. A.; Nooka, A. K.; Al-Kadhimi, Z.; Lechowicz, M. J.; Kaufman, J. L.; Lonial, S.; Waller, E. K.; Langston, A.; Flowers, C.; Cohen, J. B., Assessing Individual Comorbidities in Elderly Non-Hodgkin Lymphoma Patients Undergoing Autologous Stem Cell Transplant — Obesity Associated with Inferior Outcomes. *Blood* **2017,** *130*.
5. Leo, Q. J. N.; Ollberding, N. J.; Wilkens, L. R.; Kolonel, L. N.; Henderson, B. E.; LeMarchand, L.; Maskarinec, G., Obesity and Non-Hodgkin Lymphoma Survival in an Ethnically Diverse Population: The Multiethnic Cohort Study. *Cancer Causes & Control* **2014,** *25* (11), 1449-1459.
6. Hruby, A.; Hu, F. B., The Epidemiology of Obesity: A Big Picture. *Pharmacoeconomics* **2015,** *33* (7), 673-689.
7. Renehan, A. G.; Tyson, M.; Egger, M.; Heller, R. F.; Zwahlen, M., Body-mass index and incidence of cancer: a systematic review and meta-analysis of prospective observational studies. *Lancet* **2008,** *371* (9612), 569-578.
8. Larsson, S. C.; Wolk, A., Body mass index and risk of non-Hodgkin's and Hodgkin's lymphoma: A meta-analysis of prospective studies. *European Journal of Cancer* **2011,** *47* (16), 2422-2430.
9. Weiss, L.; Melchardt, T.; Habringer, S.; Boekstegers, A.; Hufnagl, C.; Neureiter, D.; Hopfinger, G.; Greil, R.; Egle, A., Increased body mass index is associated with improved overall survival in diffuse large B-cell lymphoma. *Annals of Oncology* **2014,** *25* (1), 171-176.
10. Carson, K. R.; Bartlett, N. L.; McDonald, J. R.; Luo, S.; Zeringue, A.; Liu, J.; Fu, Q.; Chang, S.-H.; Colditz, G. A., Increased body mass index is associated with improved survival in United States veterans with diffuse large B-cell lymphoma. *Journal of Clinical Oncology* **2012,** *30* (26), 3217-3222.
11. Hwang, H. S.; Yoon, D. H.; Suh, C.; Huh, J., Body mass index as a prognostic factor in Asian patients treated with chemoimmunotherapy for diffuse large B cell lymphoma, not otherwise specified. *Annals of Hematology* **2015,** *94* (10), 1655-1665.
12. Boyle, T.; Connors, J. M.; Gascoyne, R. D.; Berry, B. R.; Sehn, L. H.; Bashash, M.; Spinelli, J. J., Physical activity, obesity and survival in diffuse large B-cell and follicular lymphoma cases. *British Journal of Haematology* **2017,** *178* (3), 442-447.
13. Hohloch, K.; Altmann, B.; Pfreundschuh, M.; Loeffler, M.; Schmitz, N.; Zettl, F.; Ziepert, M.; Trümper, L., Obesity negatively impacts outcome in elderly female patients with aggressive B-cell lymphomas treated with R-CHOP: results from prospective trials of the German high grade non-Hodgkin's lymphoma trial group. *British Journal of Haematology* **2018,** *180* (2), 236-245.

14. Kanemasa, Y.; Shimoyama, T.; Sasaki, Y.; Tamura, M.; Sawada, T.; Omuro, Y.; Hishima, T.; Maeda, Y., Analysis of the prognostic value of BMI and the difference in its impact according to age and sex in DLBCL patients. *Hematology Oncology* **2018,** *36* (1), 76-83.
15. Li, T.; Liu, Z.-G.; Liang, P.-Q.; Wang, H.-T., Can body mass index predict the outcome of diffuse large B-cell lymphoma? A single-center retrospective study in China. *Leukemia & Lymphoma* **2017,** *58* (7), 1624-1629.
16. Jones, J. A.; Fayad, L. E.; Elting, L. S.; Rodriguez, M. A., Body mass index and outcomes in patients receiving chemotherapy for intermediate-grade B-cell non-Hodgkin lymphoma. *Leukemia & Lymphoma* **2010,** *51* (9), 1649-1657.
17. Huang, J.; Das, S. K.; Jha, P.; Zoughbi, W. A.; Schauer, S.; Claudel, T.; Sexl, V.; Vesely, P.; Birner-Gruenberger, R.; Kratky, D.; Trauner, M.; Hoefler, G., The PPARα agonist fenofibrate suppresses B-cell lymphoma in mice by modulating lipid metabolism. *Biochimica et Biophysica Acta* **2013,** *1831* (10), 1555-1565.
18. Huang, J.; Li, L.; Lian, J.; Schauer, S.; Vesely, P. W.; Kratky, D.; Hoefler, G.; Lehner, R., Tumor-Induced Hyperlipidemia Contributes to Tumor Growth. *Cell Reports* **2016,** *15* (2), 336-348.
19. Bhatt, A. P.; Jacobs, S. R.; Freemerman, A. J.; Makowski, L.; Rathmell, J. C.; Dittmer, D. P.; Damania, B., Dysregulation of fatty acid synthesis and glycolysis in non-Hodgkin lymphoma. *Proceedings of the National Academy of Sciences* **2012,** *109* (29), 11818-11823.
20. Ambrosio, M. R.; Piccaluga, P. P.; Ponzoni, M.; Rocca, B. J.; Malagnino, V.; Onorati, M.; Falco, G. D.; Calbi, V.; Ogwang, M.; Naresh, K. N.; Pileri, S. A.; Doglioni, C.; Leoncini, L.; Lazzi, S., The Alteration of Lipid Metabolism in Burkitt Lymphoma Identifies a Novel Marker: Adipophilin. *PLoS One* **2012,** *7* (8), e44315.
21. LaPensee, C. R.; Lin, G.; Dent, A. L.; Schwartz, J., Deficiency of the Transcriptional Repressor B Cell Lymphoma 6 (Bcl6) Is Accompanied by Dysregulated Lipid Metabolism. *PLoS One* **2014,** *9* (6), e97090.
22. Iritani, B. M.; Eisenman, R. N., c-Myc enhances protein synthesis and cell size during B lymphocyte development. *Proceedings of the National Academy of Sciences* **1999,** *96* (23), 13180-13185.
23. Yin, L.; Huang, X.; Liu, X.-L.; Zhang, Y.-C.; Wang, X., Distribution of lymph node metastasis from lymphoepithelial-like carcinoma of the parotid. *Oncotarget* **2017,** *8* (49), 84841–84846.
24. Fleming, F. J.; Kavanagh, D.; Crotty, T. B.; Quinn, C. M.; McDermott, E. W.; O'Higgins, N.; Hill, A. D. K., Factors affecting metastases to non-sentinel lymph nodes in breast cancer. *Journal of Clinical Pathology* **2004,** *57* (1), 73-76.
25. Liu, S.; Edgerton, S. M.; Moore-II, D. H.; Thor, A. D., Measures of Cell Turnover (Proliferation and Apoptosis) and Their Association with Survival in Breast Cancer. *Clinical Cancer Research* **2001,** *7* (6), 1716-1723.
26. McDonnell, T. J., Cell division versus cell death: a functional model of multistep neoplasia. *Molecular Carcinogenesis* **1993,** *8* (4), 209-213.
27. Morice, W. G.; Rodriguez, F. J.; Hoyer, J. D.; Kurtin, P. J., Diffuse large B-cell lymphoma with distinctive patterns of splenic and bone marrow involvement: clinicopathologic features of two cases. *Modern Pathology* **2005,** *18*, 495-502.
28. Brown, J. R.; Skarin, A. T., Clinical Mimics of Lymphoma. *The Oncologist* **2004,** *9* (4), 406-416.
29. Kaza, R. K.; Azar, S.; Al-Hawary, M. M.; Francis, I. R., Primary and secondary neoplasms of the spleen. *Cancer Imaging* **2010,** *10* (1), 173-182.

30. Shand, F. H. W.; Ueha, S.; Otsuji, M.; Koid, S. S.; Shichino, S.; Tsukui, T.; Kosugi-Kanaya, M.; Abe, J.; Tomura, M.; Ziogas, J.; Matsushima, K., Tracking of intertissue migration reveals the origins of tumor-infiltrating monocytes. *Proceedings of the National Academy of Sciences* **2014,** *111* (21), 7771-7776.
31. Johns, J. L.; Christopher, M. M., Extramedullary Hematopoiesis: A New Look at the Underlying Stem Cell Niche, Theories of Development, and Occurrence in Animals. *Veterinary Pathology* **2012,** *49* (3), 508-523.
32. Locniskar, M.; Nauss, K. M.; Newberne, P. M., The Effect of Quality and Quantity of Dietary Fat on the Immune System. *Journal of Nutrition* **1993,** *113* (5), 951-961.
33. Locniskar, M.; Nauss, K. M.; Newberne, P. M., Effect of colon tumor development and dietary fat on the immune system of rats treated with DMH. *Nutrition and Cancer* **1986,** *8* (2), 73-84.
34. Gopal K.; Nagarajan P.; Shankar E. M.; Kamarul T.; Kumar J. M., High-fat diet- and angiotensin II-induced aneurysm concurrently elicits splenic hypertrophy. *European Journal of Clinical Investigation* **2014,** *44* (12), 1169-1176.
35. Matias-da-Silva, A.; Corrêa, C. L.; Nevesa, R. H.; Machado-Silva, J. R., A high-fat diet associated with acute schistosomiasis mansoni causes disorganization in splenic architecture in mice. *Experimental Parasitology* **2012,** *132* (2), 193-199.
36. Shapiro, H.; Pecht, T.; Shaco-Levy, R.; Harman-Boehm, I.; Kirshtein, B.; Kuperman, Y.; Chen, A.; Blüher, M.; Shai, I.; Rudich, A., Adipose Tissue Foam Cells Are Present in Human Obesity. *The Journal of Clinical Endocrinology & Metabolism* **2013,** *98* (3), 1173–1181.
37. Lichtenstein, L.; Mattijssen, F.; de-Wit, N. J.; Georgiadi, A.; Hooiveld, G. J.; van-der-Meer, R.; He, Y.; Qi, L.; Koster, A.; Tamsma, J. T.; Tan, N. S.; Muller, M.; Kersten, S., Angptl4 Protects against Severe Proinflammatory Effects of Saturated Fat by Inhibiting Fatty Acid Uptake into Mesenteric Lymph Node Macrophages. *Cell Metabolism* **2010,** *12*, 580-592.
38. Lee, M.; Yea, S. S.; Jeon, Y. J., Paclitaxel causes mouse splenic lymphocytes to a state hyporesponsive to lipopolysaccharide stimulation. *International Journal of Immunopharmacology* **2000,** *22* (8), 615-621.
39. Moriya, T.; Fukatsu, K.; Noguchi, M.; Okamoto, K.; Murakoshi, S.; Saitoh, D.; Miyazaki, M.; Hase, K.; Yamamoto, J., Intravenous Administration of High-Dose Paclitaxel Reduces Gut-Associated Lymphoid Tissue Cell Number and Respiratory Immunoglobulin A Concentrations in Mice. *Surgical Infections* **2014,** *15* (1), 50-57.
40. Amato, S. F.; Swart, J. M.; Berg, M.; Wanebo, H. J.; Mehta, S. R.; Chiles, T. C., Transient stimulation of the c-Jun-NH2-terminal kinase/activator protein 1 pathway and inhibition of extracellular signal-regulated kinase are early effects in paclitaxel-mediated apoptosis in human B lymphoblasts. *Cancer Research* **1998,** *58*, 241-247.
41. Verma, R.; Foster, R. E.; Horgan, K.; Mounsey, K.; Nixon, H.; Smalle, N.; Hughes, T. A.; Carter, C. R. D., Lymphocyte depletion and repopulation after chemotherapy for primary breast cancer. *Breast Cancer Research* **2016,** *18* (10), 1-12.
42. Mackall, C. L., T-Cell Immunodeficiency Following Cytotoxic Antineoplastic Therapy: A Review. *The Oncologist* **1999,** *4* (5), 370-378.
43. Liu, H. H.; Chen, F. P.; Liu, R. K.; Lin, C. L.; Chang, K. T., Ginsenoside Rg1 improves bone marrow haematopoietic activity via extramedullary haematopoiesis of the spleen. *Journal of Cellular and Molecular Medicine* **2015,** *19* (11), 2575-2586.
44. Wang, J.; Darvishian, F., Extramedullary Hematopoiesis in Breast after Neoadjuvant Chemotherapy for Breast Carcinoma. *Annals of Clinical & Laboratory Science* **2006,** *36* (4), 475-478.

Appendix C

C.1 PCR Genotyping for Lep^{ob} Status and Eμ-*myc*

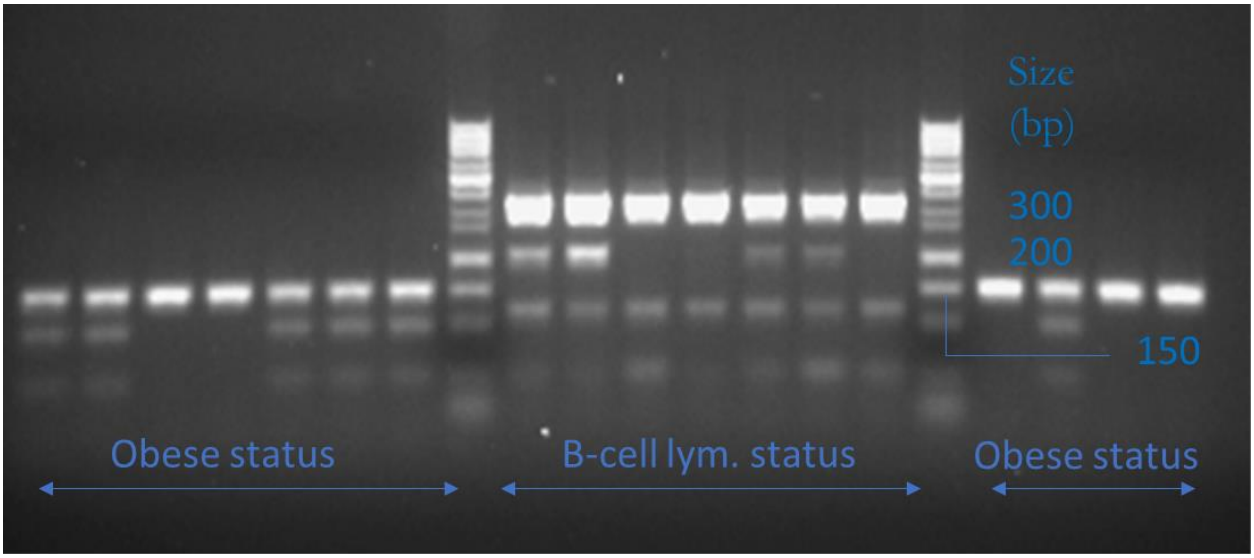


Figure C.1 Representative PCR results from the tail biopsies displaying the Lepob and Eμ-*myc* status of bred mice. 324 bp, internal positive control. 210 bp, B-cell lymphoma status. 155 bp; 155 bp, 100 bp and 55 bp; and 55 bp correspond to wild-type, heterozygous, and mutant for obesity status

CHAPTER V

Conclusion and Recommendations

5.1 Conclusion

Lipoproteins can direct intravenously injected nanoparticles away from their target sites and onto lipoproteins receptors in the body. Lipoproteins engage in lipid metabolism and thus the metabolic state of an individual as we have shown here can affect the biodistribution of injected nanoparticles. There are also gender-related differences in terms of lipid metabolism, and these results as a whole should compel us to redefine our focus and how we conduct research in the field of nanomedicine.

Since the blood profile of each individual is unique and this is also affected by certain diseased states, we ought to narrow our focus of nanotherapy based on disease type, while also conditioning our treatments to the metabolic status of each individual. Obesity for example is one of such conditions where treatment for other diseases such as cancer on the same individual can be problematic since dosages and other underlying factors relating to adequacy of treatment and toxicity becomes an issue. It is therefore imperative that we expand our knowledge in this area since we showed here that the obesity status does affect biodistribution of nanoparticles.

In summary, our investigations communicate the need for taking into consideration the metabolic status of an individual when administering nanotherapeutic drugs since it can influence nanoparticle localization and also potentially worsen diseases such as cancer.

5.2 Recommendations for Future Studies

To further examine the effect of metabolic state in nanoparticle drug delivery, it is recommended that:

(1) Future experiments be conducted that establish the molecular mechanisms behind the reduced localization of filomicelles to the organs of the liver and spleen in obese mice; possibly in relation to macrophage uptake and signaling events.

(2) In terms of lipoprotein and lipid metabolism, mice that have SCARBI-/- and LDLR-/- can potentially be used to identify further differences in plasma cholesterol uptake between the mouse genders. Additional studies using different diets (low-fat and high-fat diets) could possibly be utilized to determine how nanoparticle distribution is affected with mice embodying cholesterol plaques.

(3) For the B-cell lymphoma research, a method (e.g. flow cytometry) of identifying different B-cell subpopulations in the blood and streamlining according to disease progression would be beneficial in comparing mice with different stages of the disease. Immunostaining of spleen and lymph node tissues can also be utilized to determine specific lineages and advancement of B-cell lymphoma.

VITA

Uche Anozie earned his BSc (2010) and MSc (2012) in Chemical Engineering from the University of Akron in Ohio. His master's thesis involved the use of encapsulation technologies with biodegradable polymers to prevent sulfur blooming in rubber materials. Following his master's degree, he worked as a chemical engineer in the pharmaceutical industry before moving to Knoxville to pursue a PhD in Chemical and Biomolecular Engineering at the University of Tennessee. He joined Dr. Paul Dalhaimer's group in July of 2015 where his research was focused on drug delivery systems with implications on metabolic states.